Higher Order Mode Fibers

Israelsen, Stine Møller; Rottwitt, Karsten

Publication date:
2016

Document Version
Publisher's PDF, also known as Version of record

Higher Order Mode Fibers

By

Stine Møller Israelsen

August 2016

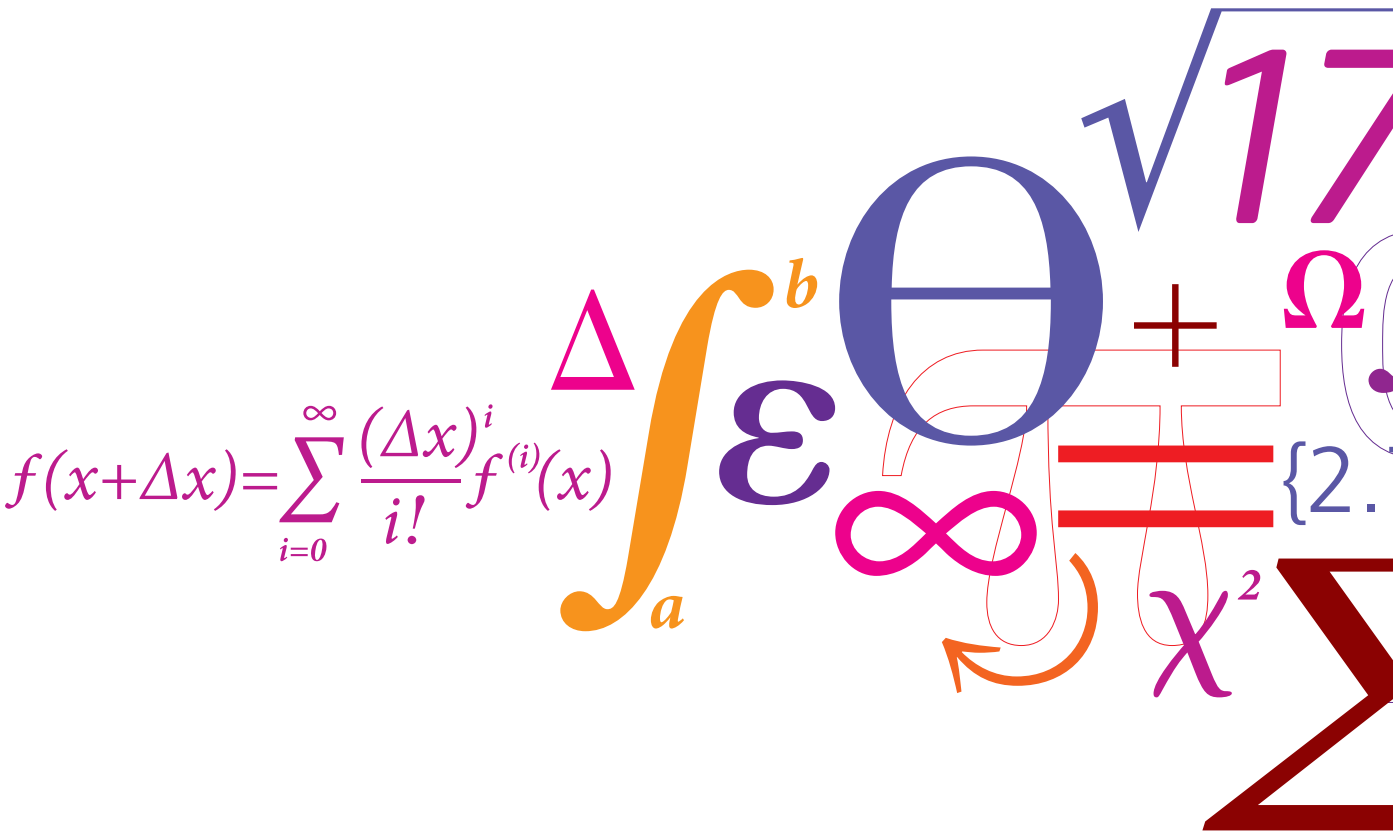

Abstract

This PhD thesis considers higher order modes (HOMs) in optical fibers. That includes their excitation and characteristics. Within the last decades, HOMs have been applied both for space multiplexing in optical communications, group velocity dispersion management and sensing among others.

The research presented in this thesis falls in three parts. In the first part, a first time demonstration of the break of the azimuthal symmetry of the Bessel-like LP_{0X} modes is presented. This effect, known as the bowtie effect, causes the mode to have an azimuthal dependence as well as a quasi-radial polarization as opposed to the linear polarization of the LP_{0X} modes. The effect is investigated numerically in a double cladding fiber with an outer aircladding using a full vectorial modesolver. Experimentally, the bowtie modes are excited using a long period grating and their free space characteristics and polarization state are investigated. For this fiber, the onset of the bowtie effect is shown numerically to be LP_{011}. The characteristics usually associated with Bessel-likes modes such as long diffraction free length and selfhealing are shown to be conserved despite the lack of azimuthal symmetry.

In the second part of the thesis, a new scheme for constructing chirped microbend long period gratings is presented. The method presents a versatile platform for tailoring the chirp to the phase matching profile of the targeted HOM conversion in the fiber under test. The scheme introduces the ability to implement a nonlinear chirp which is a first time demonstration. The results are modelled using coupled mode theory and it is shown that the conversion bandwidth may be increased more than four fold.

In the final part of the thesis, imaging as a characterization tool for HOMs is considered. Three different characterization methods are considered. First, the divergence angle is introduced as a quality parameter to replace the conventional M^2 which compares the diffraction of the investigated fiber mode to that of a Gaussian and suffers from ambiguity when considering mode mixtures. Secondly, the phase retrieval method is used to retrieve the phase profile of a mode mixture in fewmoded fiber based on volume intensity measurement. A mixture of LP_{01} and LP_{11} is considered both using a numerical example to establish the workings of the method and experimental investigations. In the experimental investigation, both a 50/50- and 88/12-mixture is considered, and in both cases the method shows reliable results. Last, a new method for determining the group velocity dispersion of modes in the LP_{0X}, LP_{1X}, and LP_{2X} mode groups based on an analysis of the field profile is presented. The method is independent of the fiber length. The method reproduces the group velocity dispersion spectra obtained analyzing a test fiber with a scalar mode solver.

RESUMÉ

Denne ph.d.-afhandling omhandler højere ordens bølgetyper i optiske fibre. Dette inkluderer deres excitation og karakteristika. Indenfor de sidste 20 år har højere ordens bølgetyper fundet anvendelse indenfor blandt andet rumlig multioverføring i optisk kommunikation, gruppehastighedsdispersion-kompensering samt i sensorer. Denne afhandling falder i tre dele.

I den første del demonstreres for første gang et brud på den azimutale symmetri for Bessellignende LP_{0X}-bølgetyper. Denne effekt, kendt som butterflyeffekten, giver bølgetypen en azimutal afhængighed såvel som en kvasi-radiel polarisation modsat den linære polarisation som er kendetegnende for LP_{0X}-bølgetypen. Effekten undersøges i en dobbelt-kappe-fiber Ved en ydre luftkappe med brug af en fuldvektoriel bølgetypeløser. Butterfly-bølgetypen undersøges eksperimentelt i samme type fiber, hvor bølgetypen exciteres ved hjælp af et lang-periode-gitter. Frirumsegenskaberne samt polarisationstilstanden karakteriseres i denne undersøgelse. For den undersøgte fiber sker overgangen til butterfly-bølgetypen for LP_{011}. De karakteristika, der sædvanligvis associeres med Bessel-lignende bølgetyper såsom lang diffraktionsfri propagationslængde og gendannelse af bølgetypen efter en forhindring, er også kendetegnende for butterfly-bølgetypen på trods af den manglende azimutale symmetri.

I anden del afhandlingen præsenteres en ny formalisme for *chirpet* mikrobøjnings-langperiodgitre. Det er alsidig platform, hvor *chirpet* kan tilpasses fasetilpasningsprofilen for den ønskede højere-ordens-bølgetype-konvertering. Denne implementering giver mulighed for et ikke-lineært *chirp*. Resultaterne modelleres numerisk ved hjælp af koblet bølgetype-teori. Herved kan det vises, at konverteringsbåndbredden kan mere end firdobles.

Den sidste del af afhandlingen omhandler billedliggørelse som et karakteriseringsværktøj for højere ordens bølgetyper. Tre forskellige karakteriseringsmetoder undersøges. Først introduceres divergensvinklen som en kvalitetsparameter i stedet for den konventionelle M^2. M^2 sammenligner diffraktionen af en given bølgetype med diffraktionen fra en gaussisk bølgetype, og det fører til en tvetydighed ved blandinger af bølgetyper. Dernæst undersøges fasefindingsmetoden. Den bruges til at finde faseprofilen ved hjælp af en volumenintensitetsmåling for bølgetypeblanding i en fiber, der understøtter få bølgetyper. For at etablere metoden undersøges en blanding af LP_{01} og LP_{11} i et numerisk eksempel. I den eksperimentelle del undersøges to blandinger af LP_{01} og LP_{11} i henholdsvis et 50/50- og et 88/12-forhold. I begge tilfælde giver metoden pålidelige resultater. Til sidst præsenteres en ny metode til fastsættelse af gruppehastighedsdispersionen uafhængigt af fiberens længde. Metoden kan bestemme gruppehastighedsdispersionen for LP_{0X}-, LP_{1X}-, og LP_{2X}-bølgetype-grupperne udfra en analyse af det elektriske felt. Metoden reproducerer værdien af gruppehastighedsdispersionen bestemt med en skalær bølgetypeløser i et numerisk eksempel.

ACKNOWLEDGEMENTS

Initially I would like to thank all my colleagues at DTU Fotonik. It has been four educational, hard and fun years. I would especially like to thank my office mates who have been very encouraging - especially during the many hours in the lab and during the thesis writing process.

I would like to thank my supervisor Karsten Rottwitt for an always open door, and for supporting and encouraging the multiple ideas I have had during the PhD-studies. I would also like to thank Jesper Lægsgaard for his help discussing the bowtie modes. The staff at the mechanical workshop have throughout my time at DTU Fotonik been very helpful in realising complicated setups for the lab.

Secondly, I would like to thank my collaborators abroad and in the industry, that includes NKT Photonics, Siddharth Ramachandrans group at Boston University, OFS Fitel, and Aart Verhoef and Alma Fernandez at TU Wien. Here, Lars Risøj and Lars G.-Nielsen have been very helpful for discussions.

Lastly, I would like to thank my family, my husband and my daughter, for all their love and support. A special thanks to my husband Niels for his meticulous proff reading.

List of publications

This list includes all publications to which I have contributed during my PhD-studies.

Published journal papers and conference contributions:

- Larsen, S. H. M., Pedersen, M. E. V., Grüner-Nielsen, L., Yan, M. F., Monberg, E. M., Wisk, P. W., and Rottwitt, K. (2012). Polarization-maintaining higher-order mode fiber module with anomalous dispersion at 1 μm. Optics Letters, 37(20), 4170-4172.
- Ingerslev, K., Israelsen, S. M., and Rottwitt, K. (2013). S2-imaging of Bessel-like Beams. Abstract from Australia and New Zealand Conference on Optics and Photonics (ANZCOP 2013), Perth, Australia.
- Israelsen, S. M., and Rottwitt, K. (2013). Effect of Aircladding on Bessel-Like Modes. Abstract from Australia and New Zealand Conference on Optics and Photonics (ANZCOP 2013), Perth, Australia.
- Larsen, S. H. M., Rishøj, L. S., and Rottwitt, K. (2013). All-fiber Raman Probe using Higher Order Modes. In Advanced Photonics Congress. (pp. SM2D.6). Optical Society of America.
- Zhu, L., Verhoef, A. J., Grüner-Nielsen, L., Israelsen, S. M., Baltiska, A., and Fernández, A. (2014). Self-starting all-polarization maintaining Yb-fiber laser with a polarization maintaining anomalous dispersion higher-order-mode fiber. Abstract from 6th EPS-QEOD EUROPHOTON CONFERENCE, Neuchatel, Switzerland.
- Israelsen, S. M., Rishøj, L. S., and Rottwitt, K. (2014). Selfhealing of asymmetric Bessel-like modes. In Proceedings of 2014 OSA Specialty Optical Fibers & Applications (SOF) meeting. . Optical Society of America (OSA).
- Israelsen, S. M., and Rottwitt, K. (2014). Divergence Angle as a Quality Parameter for Fiber Modes. In Proceedings of 2014 Conference on Lasers and Electro-Optics (CLEO). IEEE.
- Israelsen, S. M., Rishøj, L. S., and Rottwitt, K. (2014). Break up of the azimuthal symmetry of higher order fiber modes. Optics Express, 22(10), 11861-11868.
- Verhoef, A. J., Zhu, L., Israelsen, S. M., Grüner-Nielsen, L. E., Unterhuber, A., Kautek, W., Rottwitt, K., Baltuška, A., and Fernández, A. J. (2015). Sub-100 fs pulses from an all-polarization maintaining Yb-fiber oscillator with an anomalous dispersion higher-order-

mode fiber. In The European Conference on Lasers and Electro-Optics 2015. Optical Society of America.

- Verhoef, A. J., Zhu, L., Israelsen, S. M., Grüner-Nielsen, L. E., Unterhuber, A., Kautek, W., Rottwitt, K., Baltuška, A., and Fernández, A. J. (2015). Sub-100 fs pulses from an all-polarization maintaining Yb-fiber oscillator with an anomalous dispersion higher-order-mode fiber. Optics Express, 23(20), 26139-26145.

In submission:

- Israelsen, S. M., and Rottwitt, K. Broadband Higher Order Mode Conversion using Chirped Microbend Long Period Gratings. Submitted for Optics Express. See full text in App. A.
- Israelsen, S. M., and Rottwitt, K. Determining the Group Velocity Dispersion by Field Analysis for the LP_{0X}, LP_{1X}, and LP_{2X} Mode Groups Independently of the Fiber Length. Submitted for JOSA B. See full text in App. B.

In preparation:

- Lægsgaard, J., Israelsen, S. M., and Rottwitt, K. Bowtie modes - a theoretical model

Table of Contents

Page

1 Introduction **1**

2 Introduction to the Optical Fiber and Higher Order Modes **3**

2.1 The optical fiber . . . 3

2.2 Fiber modes . . . 5

2.3 Excitation of higher order modes . . . 9

2.4 Summary . . . 12

3 State of the Art for Higher Order Modes **15**

3.1 Applications of higher order modes . . . 15

3.2 Characterization of modal purity . . . 18

4 Breaking of the Aximuthal Symmetry of Bessel-like Higher Order Modes **21**

4.1 The bowtie effect . . . 22

4.2 Polarization effects of bowtie modes . . . 29

4.3 Free space properties . . . 30

4.4 Selfhealing . . . 33

4.5 Summary . . . 33

5 Chirped Microbend Long Period Gratings **37**

5.1 Proof of principle . . . 38

5.2 Numerical investigation . . . 41

5.3 Experimental results . . . 45

5.4 Summary . . . 48

6 Imaging as a characterization tool **49**

6.1 Divergence Angle as a Quality Parameter for Fiber Modes . . . 49

6.2 Phase retrieval - retrieval of the phase for pure and mixed modes . . . 53

6.2.1 Numerical example . . . 54

6.2.2 Experimental results . . . 55

6.3 Determining the Group Velocity Dispersion by Field Analysis for the LP_{0X}, LP_{1X}, and LP_{2X} Mode Groups Independently of the Fiber Length 58
6.3.1 Numerical results 61
6.3.2 Experimental results 64
6.4 Summary 66

7 Conclusion **67**

A Appendix A **69**

B Appendix B **79**

C List of Abbreviations **85**

Bibliography **87**

CHAPTER 1

INTRODUCTION

This chapter introduces the work presented in my PhD thesis "Higher order fiber modes". The first two chapters introduces the basic theory and state of the art for the application and characterization of higher order modes (HOMs). Hereafter is the research conducted during my PhD project presented.

In Ch. 2, the basic principles of the optical fiber is reviewed, that includes the operation, and the modal solutions. The second part considers the HOMs and the special characteristics linked to the HOMs. The third part of the chapter considers the excitation of HOMs. Both free space solutions and in-fiber components, which are the ones used in for the work presented in this thesis.

In Ch. 3, state of the art for applications and characterization of the purity of HOMs are considered. Among the applications of HOMs reviewed are space division multiplexing for increasing the bandwidth in optical communications, group velocity dispersion (GVD) compensation, sensing, and nonlinear processes such as four wave mixing.

The purity of HOMs is an essential parameter in most applications and the standard techniques for determining the modal purity are reviewed. These includes among others M^2, spatial and spectral spectroscopy, and cross correlated imaging.

In Ch. 4, the research on the break of the azimuthal symmetri for Bessel-like modes is presented. This research includes the first time demonstration of these modes both numerically and experimentally. The modes are excited using a long period grating (LPG) in a specially designed aircladding fiber.

In Ch. 5, a new scheme for designing chirped LPGs for HOM excitation using microbends are presented. The scheme is demonstrated experimentally and the results are predicted using a coupled mode theory model.

In Ch. 6, imaging used as a characterization tool for HOMs is presented. The chapter falls in three parts. The first part presents the divergence angle as a possible quality parameter for pure HOMs. The second part uses a phase retrieval algorithm for retrieval of a phase profile for a mode mixture in a few moded fiber. Lastly, the third part introduces a new fiber length independent characterization method for GVD in a weakly guiding step index fiber for the LP_{0X}, LP_{1X}, and LP_{2X} modes.

The conclusion is presented in Ch. 7 and sums up the contents of the thesis and presents an outlook.

In the Appendices, App. A and App. B, two unpublished manuscripts are included. In App. A, the manuscript: "Broadband Higher Order Mode Conversion using Chirped Microbend Long Period Gratings", which have been submitted for publication in Optics Express is included. The second manuscript "Determining the Group Velocity Dispersion by Field Analysis for the LP_{0X}, LP_{1X}, and LP_{2X} Mode Groups Independently of the Fiber Length", which is submitted for publication in JOSA B, is presented in App. B.

CHAPTER 2

INTRODUCTION TO THE OPTICAL FIBER AND HIGHER ORDER MODES

This chapter introduces the optical fiber and the equations that governs the propagation of light in the fiber. In particular, the concept of fiber modes including HOMs are reviewed. The characteristics of HOMs are considered and the methods for excitation of HOMs in fibers are presented.

2.1 The optical fiber

The optical fiber was invented during the 1960's, and in 1970's large progress where made in terms of reducing the loss. Charles Kao was awarded the Nobel prize in Physics in 2009 for his contributions to this work [1].

A sketch of a standard step index fiber is seen in Fig. 2.1. The core of the fiber has a large refractive index with refractive index n_c and is surrounded by a lower refractive index material called the cladding with refractive index n_{cl} [1].

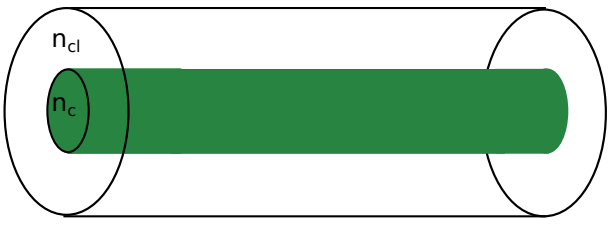

Figure 2.1: Sketch of a simple step index fiber, where the refractive index of the core, n_c, is larger than the refractive index of the cladding, n_{cl}.

The full wave equation, derived from Maxwells equations, is given by [1, 2]:

$$\nabla^2\mathbf{E} + k_0^2\epsilon\mathbf{E} = 0, \tag{2.1}$$

(2.2)

where $\mathbf{E}$ is the electric field vector, k_0 is wave number, and ϵ is the permittivity.

In the scalar approximation, also known as the weak guiding approximation where the step in refractive index between core and cladding is small, the wave equation in cartesian coordinates in Eq. (2.2) is modified to [1, 2]:

$$\frac{\partial^2\Psi}{\partial x^2} + \frac{\partial^2\Psi}{\partial y^2} + k_0^2\epsilon(r)\Psi = \beta^2\Psi, \tag{2.3}$$

where Ψ is the wave function, k_0 is wave number, $\epsilon(r)$ is the permittivity dependence of r, $r = \sqrt{x^2+y^2}$, and β is the eigenvalue also known as the propagation constant. It may be rewritten in polar coordinates, and for the core region and cladding region, respectively, to perform a separation of variables, yielding the following equation for the radial dependence in the core [1, 2]:

$$\frac{\partial^2 R_m(r)}{\partial r^2} + \frac{1}{r}\frac{\partial R_m(r)}{\partial r} - \frac{m^2}{r^2}R_m(r) + k_0^2 n_c^2 R_m(r) = \beta^2 R_m(r), \tag{2.4}$$

and in the cladding:

$$\frac{\partial^2 R_m(r)}{\partial r^2} + \frac{1}{r}\frac{\partial R_m(r)}{\partial r} - \frac{m^2}{r^2}R_m(r) + k_0^2 n_{cl}^2 R_m(r) = \beta^2 R_m(r). \tag{2.5}$$

$R_m(r)$ is the radial mode profile for the m'th solution, and n_c and n_{cl} are the refractive indices of the core and cladding, respectively. The solution to this form of equation is well known and introducing new scaled parameters, $\kappa = \sqrt{k_0^2 n_c^2 - \beta^2}$, and $\sigma = \sqrt{\beta^2 - k_0^2 - n_{cl}^2}$, the solution may be written as follows [1, 2]:

$$\Psi(r,\phi) = AJ_m(\kappa r)\cos(m\theta), \quad \text{for} \quad r < a, \tag{2.6}$$

$$\Psi(r,\phi) = BK_m(\sigma r)\cos(m\theta), \quad \text{for} \quad r > a, \tag{2.7}$$

where J_m and K_m are Bessel functions of the first and second kind, respectively, θ is azimuthal coordinate, and a is radius of the core. To ensure continuity in the field and the derivative of the field across core cladding interface, following conditions must be fulfilled [1, 2]:

$$AJ_m(\kappa a) = BK_m(\sigma a), \tag{2.8}$$

$$A\kappa J_m'(\kappa a) = B\sigma K_m'(\sigma a). \tag{2.9}$$

Each mode is thus associated with a wavelength dependent eigenvalue, β. From β, an effective refractive index is introduced:

$$n_{eff} = \frac{\beta}{k_0}. \tag{2.10}$$

The wavelength dependence of the effective refractive index leads to a mode dependent GVD. The modes in the fiber, described by the weakly guiding approximation, are indexed according to the LP-terminology. LP stands for "linearly polarized". The modes are indexed as LP_{ml} modes where the $2m$ denotes the number of nodes (zerocrossings of the magnetic field) for the full 2π at a constant radius and $l-1$ denotes the number of nodes in the radial direction. From the boundary conditions, a cutoff condition for the modes may be defined by introduction of the normalized frequency, V [1, 2]:

$$J_m(V) = 0, \tag{2.11}$$

$$V = \frac{2\pi a}{\lambda}\sqrt{n_c^2 - n_{cl}^2}. \tag{2.12}$$

In Fig. 2.2, the normalized electric field of the first four fiber modes, LP_{01}, LP_{11}, LP_{02}, and LP_{21}, in the LP-terminology are shown.

In the case, where the weakly guiding approximation is not valid, the guiding mechanism of the optical fiber is defined as strong guiding. That is the case for large index contrast fibers [1, 2]. In that case the solutions are no longer uniquely linearly polarized, and these modes are described as vectorial modes. Classes of fibers that exhibit strong guiding include among others: Photonic crystal fibers [3], aircladding fibers [4], and vortex fibers [5–7].

2.2 Fiber modes

In the previous section, the fiber modes was introduced as different spatial solutions to the wave equation. In this sections, different classes of fiber modes and their characteristics are reviewed. Both the free space and the in-fiber properties of HOM distinguish them from the fundamental mode.

Examples of the abilities of HOMs include the ability to carry orbital angular momentum [5, 7]. One example of the generation of these modes is a linear combination of two HE_{21} with a $\pm\pi/2$ phase shift in a vortex fiber [7]. The vortex fiber splits up the mode group, formed by the TE_{01}, TM_{01}, and two HE_{21}, constituting the LP_{11} mode in the scalar approximation, so that vectorial modes are no longer degenerate, that allows for the excitation of only the two HE_{21} modes with $\pm\pi/2$-phase shift [6].

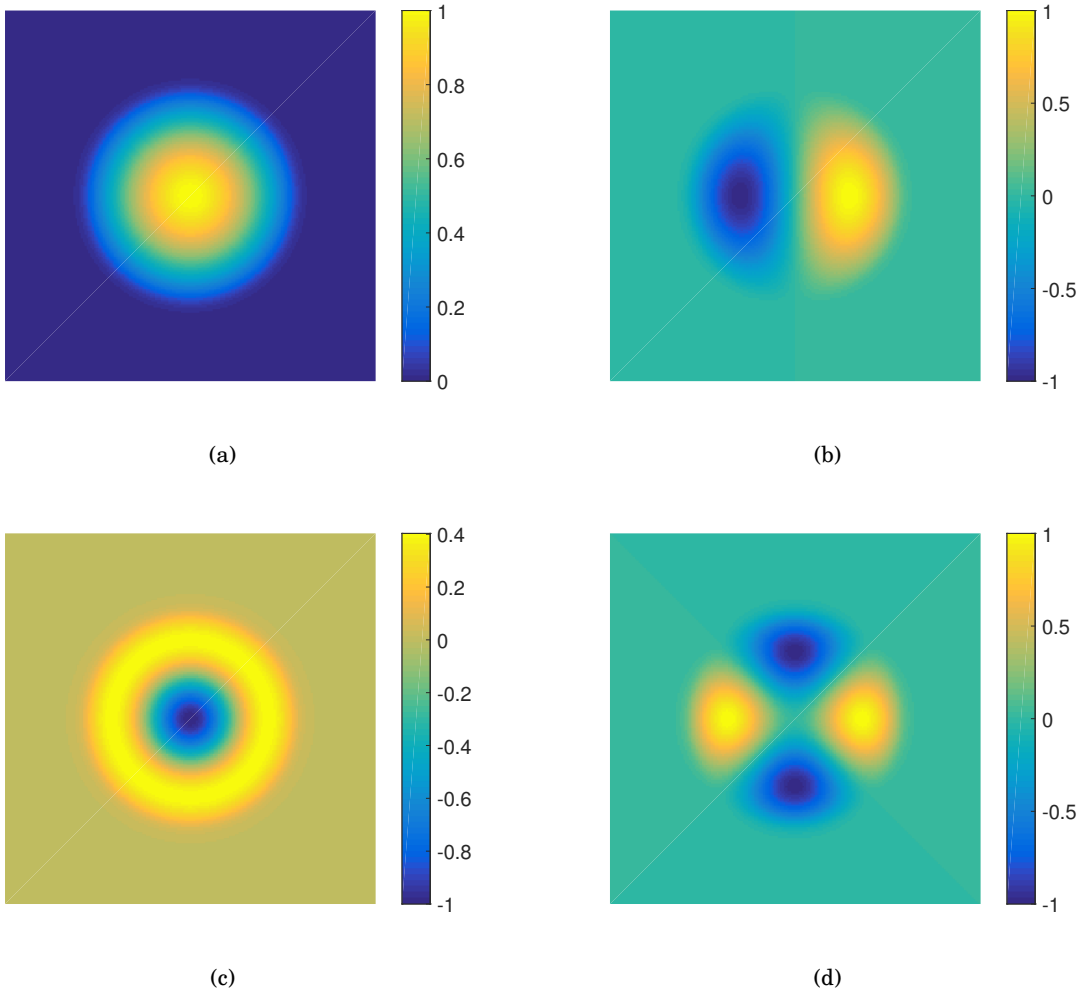

Figure 2.2: The normalized electric field of the first four fiber modes in the LP-terminology, that is (a) LP_{01}, (b) LP_{11}, (c) LP_{02}, and (d) LP_{21}. The change in the sign of the electric field indicates a shift in the phase.

One class of fibers of fibers that have shown large potential, and significantly different properties compared to the fundamental mode is the Bessel-like mode in the LP_{0X} mode group, also known as the HE_{1X} modes in the full vectorial picture.

In free space, the zero order Bessel beam have been shown to support a central bright spot propagating without diffraction many times further than the Rayleigh range [8].

When considering the scalar solution to the wave equation, see Eq. (2.7), the solution in the core for the LP_{0X} modes is described by the zero order Bessel J function, and is thus a close approximation to the Bessel beam [9]. An actual Bessel beam have infinite spatial extent and thus carry infinite energy, hence being unphysical [8], and the mode excited in the fiber is thus only an approximation. An LP_{0X} mode have been excited in a HOM fiber with more than 99 %

conversion efficiency using an LPG [9]. The principle of the increased diffraction free length, z_{max}, and its dependence on mode order is illustrated in Fig. 2.3 [8].

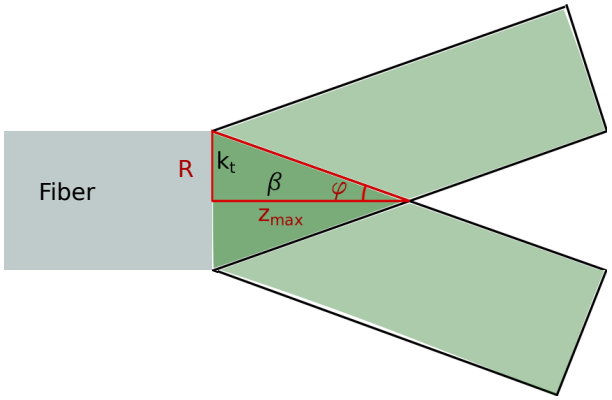

Figure 2.3: A Bessel-beam is formed of two plane waves forming a cone with a cone angle ϕ. A Bessel-like beams may be excited in a fiber, and using the propagation constant, β, and the transverse wavevector, k_t, the diffraction free length may be estimated.

Bessel beams are formed by interfering plane waves on a cone with cone angle ϕ. It can be showed $\tan(\phi) \approx R/z_{max}$, where R is the radius of the full beam. Using the same argument, a similar equation may be written in k-space as illustrated in Fig. 2.4, where $\tan(\phi) = k_t/k_z$, where k_t and k_z, is transverse and longitudinal wave vector, respectively. In an optical fiber, k_z is simply the propagation constant β. Assuming that the power is guided in the entire fiber, as illustrated in the figure, k_t is the transverse wave vector in the fiber. As the effective refractive index, n_{eff}, decreases with mode order, so does β and the fraction k_t/β increases indicating an increasing cone angle and inherently a shorter diffraction free length, z_{max}. The diffraction free length may be estimated: $z_{max} \approx R\beta/k_t$ [9]. The higher the mode order, the better the approximation to a true Bessel beam.

A second property of the Bessel-like beams is their ability to pass an obstruction without casting a shadow, this is also known as selfhealing, and has been observed in Bessel-like beams excited in optical fibers [9].

One of the allures of HOMs is the ability to tailor the GVD and the effective area - both highly relevant parameters for design of nonlinear processes [10, 11]. The GVD has two contributions - the material dispersion and the waveguide dispersion. As the name suggests, tailoring the waveguide and hence the guiding mechanisms, it is possible to tailor the waveguide dispersion. That is true for both the fundamental mode and HOMs. Strong confinement of the fundamental mode, as seen in for instance photonic crystal fibers, allows for anomalous dispersion below the zero dispersion wavelength of silica at approximately 1300 nm [12].

As a consequence of the GVD being proportional to the second derivative of the effective refractive index with respect to the wavelength, each mode has a distinctive GVD profile. Ex-

ploiting the possibility to selectively excite the mode with the desired GVD, GVD management is possible. Furthermore, as the GVD is strongly dependent on fiber design and the fiber may thus be designed so that both the GVD and the GVD slope can be compensated, something which is not possible using the fundamental mode of a photonic crystal fibers where the parameter space for GVD design is more limited [13].

The effective area is a parameter important in nonlinear processes, as well as when the nonlinearity is undesired, that could for instance be in the design of high power lasers [10]. The effective area is defined as [2]:

$$A_{eff} = \frac{\left(\int |\mathbf{E}|^2 dA\right)^2}{\int |\mathbf{E}|^4 dA}, \tag{2.13}$$

where $\mathbf{E}$ is the electric field and dA is the spatial element. From Eq. (2.13), it is evident that the effective area strongly depend on the spatial distribution of the electric field.

When scaling the fiber there is however an important concern: The mode stability. Stable mode propagation for the fundamental mode with large effective area have been demonstrated in rod type fibers [14]. In solid silica fibers, the fundamental mode, however becomes unstable when scaling the effective area [10]. The instability have two sources: Mode distortions and mode coupling. HOMs are more resistant to mode distortions, which makes them good candidates for scaling the effective area. That may be explained by the natural bend immunity of HOMs [15].

A bend is typical perturbation to the fiber, and can generally be explained by considering a tilted index profile. The concept is illustrated in Fig. 2.4. In Fig. 2.4(a), the effect of the bend on the fundamental mode is considered. When the fiber is bent, an evanescent or forbidden region is created due to the fact that $\Delta n_{bend} > \Delta n_{LP_{01}}$, and the power carried by the mode leaks into the evanescent region. Also the mode assumes a non-Gaussian like shape as it is only guided in one side of the fiber, and the effective area is reduced up to 70 % [15]. In 2.4(b), a HOM configuration is presented. As $\Delta n_{bend} < \Delta n_{HOM}$, no evanescent region is created and the mode may propagate stably without shape distortions [15].

For the second source of instability, mode coupling, HOMs typically couples to the nearest neighbour as a result of small pertubations, that could for instance be fabrication inhomogenities. In the case of LP_{0X}, previously mentioned for their free space properties, the nearest neighbor is the LP_{1X} mode in case of bend perturbations. Sufficient splitting in the refractive index of these two mode groups is necessary for stable propagation without mode coupling. It has been shown that this splitting increases with mode order, being an order of magnitude larger than the splitting between the fundamental mode, LP_{01}, and it's nearest neighbor LP_{11} [10]. Coupling to other mode groups need also be considered for the full picture of the mode coupling. Despite the selection rules for direct mode coupling via bend perturbations demanding coupling to a neighboring mode group, indirect coupling to the LP_{2X} and LP_{6X} mode group has been observed experimentally [10].

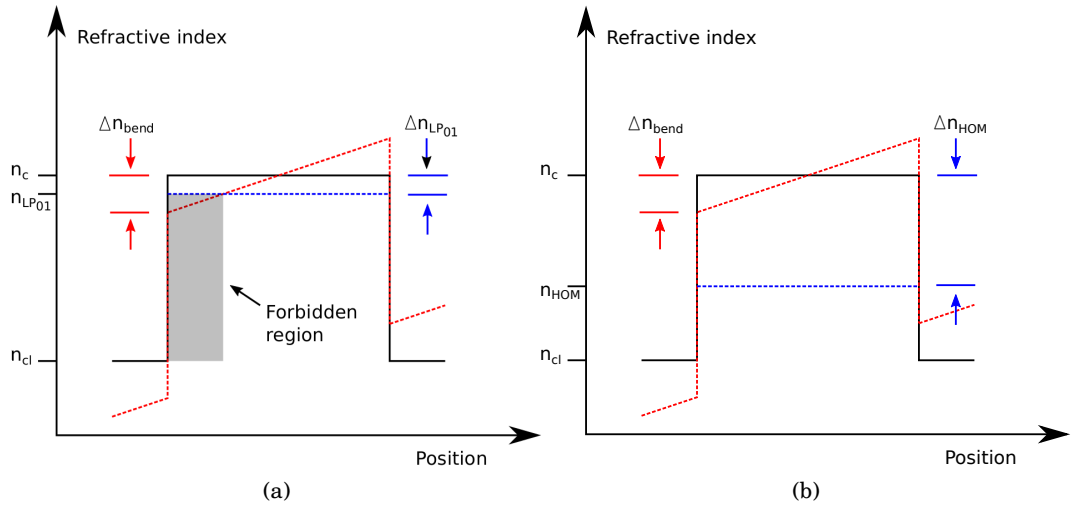

Figure 2.4: The refractive index profile of the unbent fiber is plotted in black. The red dotted lines indicate the perturbation to the refractive index profile caused by the bend. In (a), the fundamental mode, LP_{01}, considered. When the fiber is bent, the mode leaks out into the forbidden (evanescent) region. In (b), a HOM is considered. As indicated by the dotted blue line, the HOM is well guided in both the bent and the unbent fiber.

2.3 Excitation of higher order modes

In this section, a selection of the most common methods of exciting HOMs is reviewed. This section falls in three parts: In the first part the principle of the LPG is reviewed. In the second part, free space methods such as phase plates, spatial light modulators (SLMs) and q-plates are considered. The third and last part covers the remaining methods such as tapered couplers and photonic lanterns.

LPG is preferred method of excitation for the work presented in this thesis. LPGs used as in-fiber band rejection filters was first presented by Vengsarkar *et al.* and present many interesting features such as low loss and small back reflection [16]. The LPG as opposed to the conventional Bragg grating couples two co-propagating modes. Conventionally, the coupling takes place from the fundamental mode (LP_{01} or HE_{11}) to a HOM. Each of these modes is characterized by a propagation constant, $\beta_{\text{fundamental}}$ and β_{HOM}, respectively. To achieve phase matching between the two modes, following condition must be fulfilled [16–18]:

$$\beta_{\text{fundamental}} - \beta_{HOM} = \frac{2\pi}{\Lambda}. \tag{2.14}$$

In Fig. 2.5, the schematics of a LPG is illustrated. The pertubation is shown as a variation of the refractive index of the core.

Λ is the pitch of the LPG - that is period of the grating along the axis of propagation. Optimum conversion is thus met when this criterion is fullfilled, the equation may be rewritten

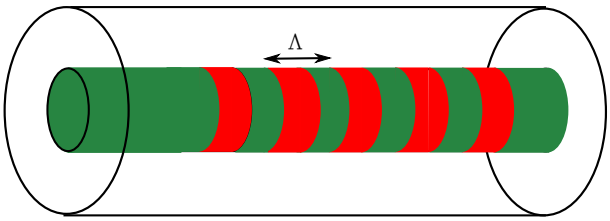

Figure 2.5: Sketch of a LPG in simple step index fiber where the pertubation is a change of the refractive index in the core. The period of the pertubation is given by the pitch, Λ.

introducing a wavelength dependent detuning parameter, $\delta(\lambda)$

$$\delta(\lambda) = \frac{1}{2}\left(\frac{2\pi}{\Lambda} - \Delta\beta(\lambda)\right). \tag{2.15}$$

The coupling is optimum for $\delta(\lambda) = 0$ and trails of for wavelengths shorter and longer. The phasematching condition Eq. (2.14) describes the simple case of first order diffraction. The equation may be generalized to include higher order diffraction by modifying it to [19]:

$$\beta_{\text{fundamental}} - \beta_{HOM} = \frac{2\pi N}{\Lambda}, \tag{2.16}$$

where N is an integer. Higher order diffraction LPGs have been demonstrated on several occations [20–23]. Higher order diffraction may lead to increased number of spectral features in the conversion spectrum [20].

As the propagation constant is wavelength dependent, the phase matching condition also has a spectral response.

The LPG is a reversible device and may thus couple both from the fundamental mode to HOM but also from a HOM to the fundamental mode.

The response of the LPG may be described by coupled mode theory [17]:

$$\frac{\mathrm{d}E_A}{\mathrm{d}z} = -i\sigma E_A(z) - i\kappa^* E_B(z)\exp(i\delta z), \tag{2.17}$$

$$\frac{\mathrm{d}E_B}{\mathrm{d}z} = -i\sigma E_B(z) + i\kappa E_A(z)\exp(-i\delta z), \tag{2.18}$$

where E_A and E_B are the amplitudes of the electric field of the two modes, δ is detuning parameter, and κ is the cross coupling coefficient. The general self-coupling coefficient, σ, is defined as [17]:

$$\sigma_x \propto \int \Delta n_{\text{average}} E_x E_x dS, \tag{2.19}$$

where as the cross-coupling coefficient is defined as [17]:

$$\kappa \propto \int \Delta n_{\text{max}} E_A E_B dS. \tag{2.20}$$

E_x is the electric field strength of the given mode, $\Delta n_{\text{average}} = (n_{\max} + n_{\min})/2$ is average refractive index of the pertubation (n_{min} being the minimum refractive index, and $n_{\max}$ being the minimum refractive index), $\Delta n_{\max} = n_{\max} - n_{\min}$ is maximum refractive index of the pertubation, and dS is the cross section area of the pertubation [17, 18]. It may easily be shown that the optimum coupling is achieved, without overcoupling, when $\kappa L \leq \pi/2$, where L is the length of the LPG [17, 18].

Several schemes for implementation of the LPG have been demonstrated. Roughly speaking, the implementations can be categorized in two groups: UV-induced LPGs and mechanical LPGs.

UV-induced LPGs are traditionally used for the conversion from the symmetrical fundamental mode to symmetrical HOMs [10], unless in a tilted version where it may couple from a symmetrical to an asymmetrical mode [24].

UV-induced LPGs can produced both in a point-by-point UV-writing setup [9] and using an amplitude mask [10]. The deuterium loaded germanium co-doped fiber core is exposed to UV light in a periodic pattern as illustrated in Fig. 2.5. That gives rise to a permanent increment of the refractive index of the core [10]. The change in the refractive index is permanent. The UV-writing is typically performed at 248 nm [16].

A class of LPGs related to the UV-induced LPGs are LPGs formed with high intensity lasers such as fs-lasers [25–27]. The LPGs formed with fs-lasers may be inscribed in all-silica fibers, as opposed to UV-written LPGs, all though greater refractive index change is achieved in germanium co-doped fibers [25]. The process relies on the ability of high intensity light to make changes to the refractive index of silica glasses by damaging the silica bonds [25].

For the second class of LPGs, classified as mechanical LPGs, a periodic deformation of the fiber is performed and that leads to a coupling to a HOM. This class of LPGs couple a symmetric mode e.g. the fundamental mode to an asymmetric HOM [11, 28] or a cylindrical vectorial mode [5, 6]. Several implementations of mechanical LPGs have been demonstrated and includes helical LPGs [29, 30], microbend LPGs [11, 31], CO_2-written LPGs [28, 32], and a thermally induced LPG created with a heat wire [31]. LPGs are attractive as they are potentially low loss [10], high conversion in-fiber devices which may be implemented in for instance all-fiber lasers [33, 34]. Microbend LPGs have an inherent polarization dependency as the asymmetric modes to which they couple consist of a group of vectorial fiber modes, that leads to a polarization dependent conversion resonance [35]. They are also potentially temperature stable [32], the temperature dependence present for most LPGs may however also be used in sensing applications [36].

LPGs can both be employed as narrowband rejection filters [16], but may also be implemented in a broadband configuration. In the narrowband configuration, conversion efficiencies as large as 30 dB have been demonstrated [10]. Broadband mode conversion may be achieved in several ways, one is to increase Δn_{max} [28], another is to employ chirped LPGs [37] , and thirdly

socalled turn-around-point (TAP) LPGs can be used [10, 11, 38, 39]. The TAP is the point where the group delay difference between the two modes in the conversion process is zero [38]. With a TAP LPG, mode conversion bandwidths up to 94 nm have been realized [10]. This number does however depend on the group velocity dispersion profile and inherently the fiber design and is hence an increasing number.

The second group of mode converters covers the large range of free space elements which may be used to excite HOMs in fibers. Whereas LPGs typically, though not exclusively [24], require the fiber to have a single moded core making them sensitive to nonlinear effects in high power applications, free space elements are independent of such considerations. Possible free space elements include axicons [40, 41], used for the excitation of Bessel-like modes. Phase plates have also been demonstrated for the conversion of LP_{0X} modes to a nearly fundamental Gaussian output [42]. Another free space element, the q-plate has been used for selective excitation of optical angular momentum modes (OAM) [43]. A fourth method is to use computer generated holograms [44, 45]. Lastly, SLMs have been shown to excite Bessel-like modes with conversion rates up to 17 dB [46].

In common for all of these elements is that either or both the phase and amplitude of the phase of the beam is modified upon input or output of the fiber.

In the last group of mode converters, tapered couplers and photonic lanterns is reviewed. In photonic crystal fibers and other holey fibers, LPGs as mode converters have limited effect, though they have been demonstrated [47, 48]. Using a UV-induced LPG requires a co-doping of germanium for high coupling [10], and microbend LPGs tends to damage the holey fibers. Another form of in-fiber coupler is the tapered coupler, designing the taper mode conversion from the fundamental mode to LP_{11} and LP_{02} have been demonstrated [49]. Other close related forms of mode converters was presented by Witkowska *et al.* and consist of either carefully designed hole collapse or a twisted fused coupler as known from conventional fiber optics [50].

Using photonic lanterns is another option, where several fibers are fused into one allowing for efficient multimode to single mode coupling [51, 52]. The photonic lantern has also been demonstrated in a mode selective form for use in for instance mode division multiplexing (MDM) [53]. This is not the direct form of HOM generation as seen in the other mode converters but nonetheless an applicable device in the HOM to fundamental mode conversion process.

2.4 Summary

In this section, the introductory theory used as a prerequisite throughout the remaining thesis is reviewed. That includes the governing equations for the optical fiber as well as the modal solutions in the weak guiding approximation and an overview of the implications of strong guiding. Hereafter fiber modes and in particular HOMs are review in terms of the characteristics and

properties which eliminates them from the fundamental mode. Lastly, the excitation of HOMs is presented with strong focus on the workings of the LPG.

CHAPTER 3

STATE OF THE ART FOR HIGHER ORDER MODES

This chapter focuses on state of the art of applications of the HOMs introduced in Ch- 2. When using HOMs, purity of the modes is essential and several characterization methods are therefore reviewed as well in the second part of the chapter.

3.1 Applications of higher order modes

HOMs have had applications within fiber optics for more than two decades. Applications of HOMs include, not exclusively, usage for space-division multiplexing in optical communication, GVD compensation, sensing, and nonlinear frequency conversion.

Initially, the use of HOMs for optical communication is considered. Within conventional fiber optics, researchers have within the last decades, exploited and optimized multiplexing in time, wavelength, polarization and phase to reach more capacity for the ever growing demand. The capacity limit approaches, and spatial multiplexing is now a possibility being explored. Generally, space-division multiplexing operates with two regimes: Multicore fibers and multimoded fibers [54]. A crucial factor in both schemes is the ability to separate the channels to limit cross talk.

The multicore fiber is not strictly within the regime of HOMs, but is nonetheless briefly reviewed. The multicore fiber is a fiber with a number of single mode cores. The cores may either work in a decoupled manor or a coupled manor with a number of supermodes [54]. Up to 30 separate cores within a limited fiber diameter ($\approx 200\mu$m) have been demonstrated [55], this is however a constantly improving number.

In terms of mode multiplexing in few mode fibers, both demonstrations in LP-mode basis

with mode selectivity larger than 28 dB [56] and in the vectorial basis [54] have been documented. More complex formats using modes that carry optical angular momentum have also been reported [5].

Besides the issues concerning mode mixing during propagation due to for instance fiber inhomogenities, the modes generally exhibit differential mode group delay and differential modal loss or gain. As a result of mode coupling and differential mode group delay, the energy of a given data symbol launched into a spatial mode spreads into adjacent symbol time slots, and the quality of data transmission rapidly diminishes. To mitigate some of these issues, the multiple input multiple output (MIMO) technique is used [54].

A second application of HOMs is for GVD compensation, and in particular for the implementation in ultra short pulse fiber lasers. The concept of HOM GVD compensation was introduced by Poole *et al.* using an LP_{11} to compensate the GVD in the fundamental mode, however as the LP_{11}-mode consists of four vectorial modes, this scheme suffers from polarization mode dispersion, which is hard to compensate [13]. Instead, Ramachandran *et al.* suggested using LP_{02} for GVD compensation around 1 μm. This scheme also offers GVD slope compensation [13]. The scheme has also been demonstrated in a polarization maintaining (PM) fiber, where there is increased stability for implementation in ultra short pulse fiber lasers [33, 39].

Several demonstrations of HOM compensation in fs-fiber laser have been demonstrated both in a non-PM configuration with a pulse duration of 62 fs [34] and in a PM configuration, with increased environmental stability, and a pulse duration of 95 fs, which is currently state of the art for all-fiber PM lasers [33].

The third group of applications is sensing. Sensing using HOMs is very wide disciplin and the mentioned examples thus only covers part of the research carried out.

As previosly mentioned, the resonance wavelength of LPGs is sensitive to for instance temperature. That may be exploited in a sensing scheme. In the typical LPG sensor, the LPG couples to a series of cladding modes, resulting in a number of attenuation bands in the transmission spectrum. The resonance of the attenuation band is sensitive to the local environment, and a change in the local environment results in a change in the transmission spectrum. LPG sensoring have been demonstrated for the measurement of temperature, strain, load, bend radius, and the refractive index surronding the fibre. As the effect on the transmission spectrum depends on the measurand, it is possible to construct multiple parameter sensor using a single LPG [57]. A simultaneous temperature and bend sensor has been reported by Ye *et al.* [58]. A change in the temperature results in a shift in the resonance wavelength in the transmission band, whereas a bend results in one of two possibilities: Either a splitting of the resonance, where split depends on the bend radius, or a shift in the central wavelength of the attenuation band. The first manifestation is a result of the breaking of symmetry in the fiber indicating two degenerate cladding

modes become non-degenerate. This effect have been observed in Ge-B-codoped fibers. The second manifestation is accompanied by a reduction of the loss and a broadening of the resonance. The magnitude of the wavelength shift has been showed to depend on the orientation of the LPG with respect to the plane of the bend, this obviously works best in fibers with an eccentric fiber core [57].

The sensitivity to a specific measurand is dependent on fiber composition and the order of the cladding mode to which the LPG couples, that makes it possible to tailor the LPG to the wanted sensor. More specifically, appropriate fiber and LPG design allows for attenuation bands insensitive to e.g. temperature or strain, allowing for multiparameter sensing. Alternatively differential shifts in minimum two resonance bands of a single LPG may used for multiparameter sensing [57].

A temperature sensor has also been constructed using the HOM itself, or to be more precise the interference of two HOMs. Li *et al.* reported a temperature sensor constructed of a single mode fiber (SMF) and a multimode fiber [59]. Two HOMs are excited, LP_{06} and LP_{07} - determined by the intermodal difference - and the wavelength difference between destructive interference between the two modes is temperature dependent. The sensor is able to measure temperature differences up to 800 °C.

Another use of the HOMs is the use of the long diffraction free length of the Bessel-like LP_{OX} modes to make a all-fiber Raman probe. The HOMs are excited using a LPG, the concept offers the possibility of an all-fiber Raman probe with controllable penetration depth [60].

Also an all-fiber STED microscope have been demonstrated using OAM modes excited with a UV-induced LPG in a vortex fiber offering nanoscale resolution. This implementation offers low loss and tolerance to perturbations as well as excitation and depletion beams with sizes and depletion ratios comparable to free space implementations [61].

The last subset of applications reviewed is nonlinear processes using HOMs. Soliton self frequency shift in optical fibers is a process where Raman self-pumping continuously transfer energy from higher to lower frequencies. That may be exploited to construct widely frequency-tunable fs pulse sources with fiber delivery. Anomalous GVD is required for the generation and maintenance of solitons, that is achievable for HOMs below the zero dispersion wavelength (ZDW) of silica, approximately 1300 nm, as also exploited in the GVD compensation scheme described earlier [11, 13, 39]. Soliton self-frequency shifts have been demonstrated in an all-silica fiber from 1064 nm to 1200 nm by van Howe *et al.* [62].

The first demonstrations of non-linear frequency mixing using Bessel-like modes were reported by Steinvurzel *et al.* [63], and improved results leading to continuum generation again exploiting the Bessel-like LP_{0X}-modes were demontrated by Demas *et al.* [64]. The Bessel-like modes offer stable propagation and is thus not limited in their use by uncontrollable mode cou-

pling as demonstration in few moded fibers has been limited by [10]. Using the difference in propagation constant allows for intramodal nonlinear mixing demonstrated for the LP_{06}-mode and intermodal nonlinear mixing LP_{06} to a continuum of mode ranging from LP_{07} to LP_{016}. The process exploited is fourwave mixing, pumping hard allows for cascaded four wave mixing, and 11 resolvable modes covering two octaves may excited in this process [64].

3.2 Characterization of modal purity

An important characteristic for the HOMs is the modal purity. A variety of methods have been reported during the last decades, and this section highlights the workings of the most used.

The original method for characterizing nearly Gaussian beams, the M^2-method, was adapted by Yoda *et al.* for characterizing the beam quality of HOMs [65]. The M^2-method compares the free space diffraction of a given beam to diffraction of a perfect Gaussian beam and supplies the ratio, thus an M^2 of 1 indicates a perfect Gaussian. This method has been critiqued as it is not very sensitive to modal mixtures and an excellent M^2 of 1.1 might actually cover up to 30 % HOM content [66]. M^2 of modal mixtures is strongly dependent on the intermodal phase [66].

In stead, the beam quality of a mixed beam may instead be characterized by a method providing modal decomposition. The free space properties of a pure mode may be determined measuring the divergence angle [22]. Most beams however are not pure.

The methods for modal decomposition may be divided into two groups: One where the modal basis for decomposition is known, and one where the basis is unknown. For the methods where the basis is known, it corresponds to knowing the fiber parameters such as guiding mechanism, index contrast and core radius.

The first method presented relies on the basis of phase retrieval schemes [67]. Shapira *et al.* are able to uniquely decompose the vectorial modes in a fewmoded photonic crystal fiber [68]. The method uses on two images: One of the intensity distribution immediately upon exiting the fiber and one of the far field. The method relies on the principles of the phase retrieval algorithm [67]. An *a priori* constraint of the field distribution is key for this type of method to provide a unique solution. The phase retrieval algorithm is inherently a 2D problem, given by the dimensions of the intensity measurements [67]. The modal decomposition may however be reduced to 1D problem since the field is constrained to be a linear superposition of the fiber eigenmodes that can be determined from the fiber structure. The modal decomposition provides the expansion coefficients and thus reduces the size of the computation [68]. The algorithm is constructed to minimize an error function with respect to a set of independent variables representing the expansion coefficients for the chosen basis. Since the basis is formed of vectorial fiber modes, four squared-error functions for two orthogonally polarized components in the near and far field

are constructed. The fields are reconstructed with the 16 lowest energy modes, restricting the angular momentum to $m < 4$. Repeating the decomposition with five distinct pairs of orthogonal polarization directions, and the correlation coefficients between the decomposition results exceeds 0.98 [68].

A second method relying on *a priori* knowledge in form of basis of fiber eigenmodes is the modal decomposition based on computer generated holograms [69]. Flamm *et al.* excites and decomposes a modal mixture in a large mode area fiber using SLMs, the basis used is the LP-modes of the weak guiding approximation. In Ch. 2, the excitation of pure modes using SLMs was reviewed [46]. The modal mixture is projected onto a digital hologram, and the modal components are split, and the intermodal phase is found from reference to a dominating mode [69].

The second group of modal decomposition methods is independent of *a priori* knowledge.

A widely used technique not requiring any *a priori* knowledge is the S^2-technique. First documented by Nicholson *et al.* [70], and later optimized [71–73]. The S^2-method refers to spatially and spectrally resolved imaging of modal content. The method requires a dominant mode, preferably the fundamental mode as it does not have any areas with zero or very low intensity within the guiding area [72]. The method is able to discriminate HOM content down to 50-60 dB below the power level of the fundamental mode. Nicholson *et al.* explains the concept of S^2 [70]:

"S^2 imaging is based on the idea that modes propagating in optical fibers can be identified by both the group delay difference which leads to a spectral interference pattern in a broadband source propagating through the fiber, as well as by a distinct spatial interference pattern between the high-order mode and the fundamental mode. "

A broadband source illuminates the fiber under test (FUT). After the FUT, the light passes through a polarizer. The light is then collected in a SMF in a rectangular grid. The presence of multiple modes leads to an interference beating in the SMF, assuming that all intensities may be related by a space dependent constant. Through simple mathematics, the group delay and Fourier transform of the measured spectrum, the space dependent constant may be determined, allowing for the evaluation multipath interference (MPI) and the intensity distribution [70]. This concept has continually been improved, first using a wavelength swept source and a camera [71] and in real-time version using a wavelength swept source and camera, where the wavelength swept source is triggered by the camera [73].

Whereas S^2 relied on a dominant mode, C^2 - cross correlated imaging - is free of such constraints [74]. The method is based on optical low-coherence interferometry. It is based on cross-correlations of the fiber output with a reference beam. The analysis of the low-coherence interferometry is based on the slowly varying envelope. The setup is based on a GVD compensated Mach Zender interferometer with a reference arm with a varible delay, a broadband source, a bandpass filter, and a camera. The setup provides information on the modal weights, intensity

profiles, relative group-delays and GVD of all guided or quasi-guided (leaky) modes [74]. The method has also been demonstrated in the frequency domain, employing a wavelength swept source and a camera [75]. In the frequency domain, the measurements are performed on a sub-second time scale and it may thus be used for the alignment of the free space excitation of HOMs [75].

CHAPTER 4

BREAKING OF THE AXIMUTHAL SYMMETRY OF BESSEL-LIKE HIGHER ORDER MODES

HOMs have many applications as discussed in Ch. 3, and in particular Bessel-like modes, have recently attracted much attention within fiber optics. This chapter focuses on the Bessel-like modes in the LP_{0X} mode group - also known as HE_{1X} modes in the full vectorial theory [1]. Their long diffraction free propagation may for instance be use to create optical bottles [76, 77].

Bessel beams were first introduced by Durnin *et al.* and possess many interesting properties such as diffraction resistant propagation and selfhealing [8]. Bessel-like beams may be excited in optical fibers, the so-called LP_{0X} modes in the scalar approximation and HE_{1X} modes in the full vectorial theory [1], using a UV-induced LPG [9] and with SLMs employing free space incoupling [46].

For high mode orders, break up of the azimuthal symmetry in LP_{0X} modes is demonstrated. That effects the polarization state, effective areas, mode conversion efficiencies, and free space properties [78, 79].

Degeneracy and symmetry groups of microstructured fibers have earlier been investigated for low order modes [80–82]. Here, the analysis shows a tendency towards non-degeneracy of the modes [80].

The investigations in this chapter are both numerical and experimental. Bessel-like modes excited in a double cladding structure are considered. The outer cladding in the fiber structure is an aircladding. The modes are excited with a UV-induced LPG inscribed in the singlemoded core and propagate in the inner cladding using the point-by-point method. Such modes have earlier been investigated by e.g. Ramachandran *et al.* [10]. For very high order Bessel-like modes,

it has been observed that the azimuthal symmetry is broken and the intensity profile of the mode assumes a bowtie shape, these modes have been denoted bowtie modes [78]. These modes are investigated experimentally, by considering an LP_{016} mode generated with minimum 90 % conversion efficiency over a narrow 2 nm bandwidth. Israelsen *et al.* introduced a new notation to denote the bowtie modes as they are both experimentally and numerically shown to be non-linearly polarized and the scalar approximation no longer is valid [78]. For the bowtie mode corresponding to an LP_{0X} mode, the notation BT_{0X} is used, and the enumeration of the modes is thus similar. The first 0 indicates a central lobe and the X denotes the number of rings plus one [78]. The generated mode is hence forward denoted BT_{016}.

In this chapter, the onset of the investigated bowtie effect and the dependence of this effect on the fiber design are investigated numerically using a full vectorial modesolver, COMSOL [78]. An explanation of the properties of these modes recently presented by Rishøj *et al.* is also included [83]. The free space properties of the simulated modes are investigated using fast Fourier transform (FFT) propagation, designed after the principles described by Delen *et al.* [84]. These properties are compared to those of an ideal mode - with no azimuthal dependence - generated with a scalar modesolver. The selfhealing property observed for Bessel-like modes [9] is also evaluated [79].

4.1 The bowtie effect

To describe the break up of the azimuthal symmetry experimentally, a narrowband LPG is inscribed in a double cladding fiber to excite a high order Bessel-like mode [78]. A microscope image and a sketch of the refractive index profile of the fiber are depicted in Fig. 4.1.

The aircladding is designed to minimize the size of the bridges, so that the shape of the bridges does not effect the guiding mechanisms of the aircladding.

The conversion efficiency of the LPG, converting from LP_{01} to BT_{016}, is plotted in Fig. 4.2a. The conversion efficiency is measured by splicing the FUT to a SMF and measuring the transmission of a broadband source, assuming no other losses in the system, this may be converted to a conversion efficiency. This is a standard method for measuring the conversion efficiency for an LPG [16]. Around 810 nm, there is an artefact from the illuminating supercontinuum source. An image of the generated mode is shown in Fig. 4.2b, note, the camera is unsaturated. The LPG is here illuminated with a narrowband source. Due to the large difference in intensity across the mode and the limitation in the camera given by a dynamic range of 8 bit, the features in the outer rings of the mode are hard to observe. The conversion efficiency shows very little MPI indicating excitation of a single mode by the LPG, which verifies the assumption of no other losses in the transmission measurement. From the modal image, it is seen that the mode has a central peak but the azimuthal symmetry is broken compared to an ideal LP_{0X} mode. This effect is denoted the bowtie effect and was first documented by Israelsen *et al.* [78], and the mode is

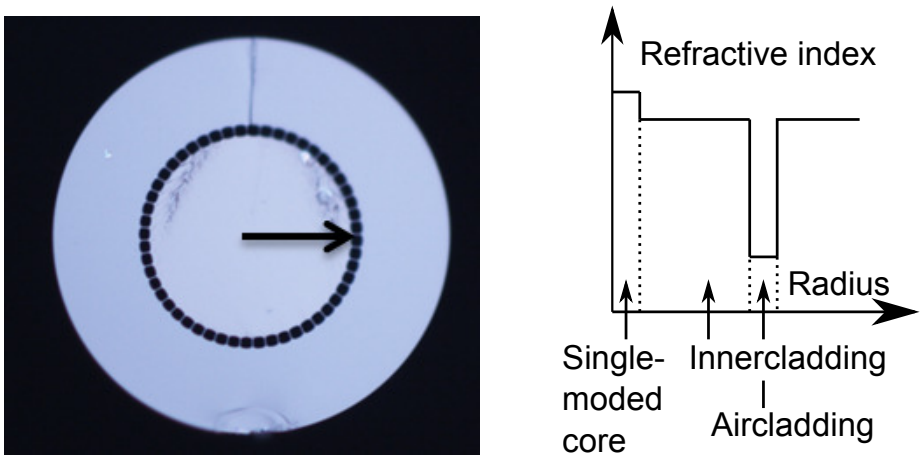

(a) (b)

Figure 4.1: (a) Microscope image of the fiber end facet. The outer diameter of the fiber is 156 μm. The radius of the inner cladding is 39 μm and the airholes have a radius of 2 μm. The fiber is designed and drawed in collaboration with NKT Photonics. (b) A sketch of the refractive index profile of the fiber along the direction indicated by the arrow in (a).

thus BT_{016}. By slight pertubation of the fiber, the orientation of the bowtie may easily be shifted, indicating that two degenerates modes with orthogonal orientation are present [78]. The mode is propagated 76 cm, showing that the mode propagates stably in the fiber.

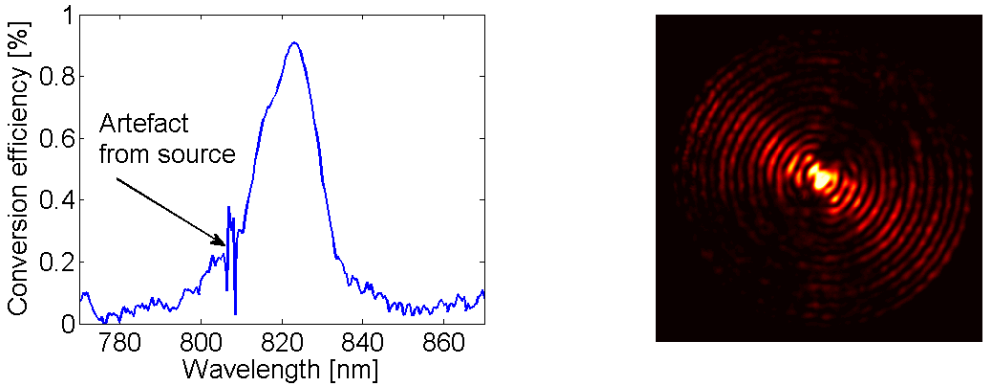

(a) (b)

Figure 4.2: (a) Conversion efficiency of the LPG converting LP_{01} to BT_{016} in the aircladding fiber. (b) Image of the BT_{016} mode after 76 cm of propagation in the aircladding fiber.

To show that the break up of the azimuthal symmetry is neither an imaging nor an interference effect but is in fact a guided mode of the fiber, the fiber structure is investigated with a full vectorial modesolver to find the guided modes in a double cladding structure, more specifically COMSOL [78]. The modes are found employing a triangular grid. A double cladding structure

with an aircladding as the outer cladding is considered. The radius of the holes in the aircladding is varied while maintaining the number of holes in the aircladding to find the onset of the bowtie effect. Varying the holes effectively varies index contrast between the inner and outer cladding. A sketch of the full simulated fiber geometry and a zoom-in on the aircladding region is shown in Fig. 4.3a and in Fig. 4.3b, respectively. Notice when the radius of the holes in the aircladding is decreased the width of the silica bridges between the airholes is increased as the number of holes and the aircladding radius is maintained [78]. A zoom-in on the mesh in aircladding region is depicted in Fig 4.3c, this zoom-in shows the smallest mesh features in the fiber geometry. The size of the mesh changes across the structure and is smallest around the small features in the fiber design, such as the airholes and the core region. The size of mesh may be compared against the feature size in Fig. 4.3c.

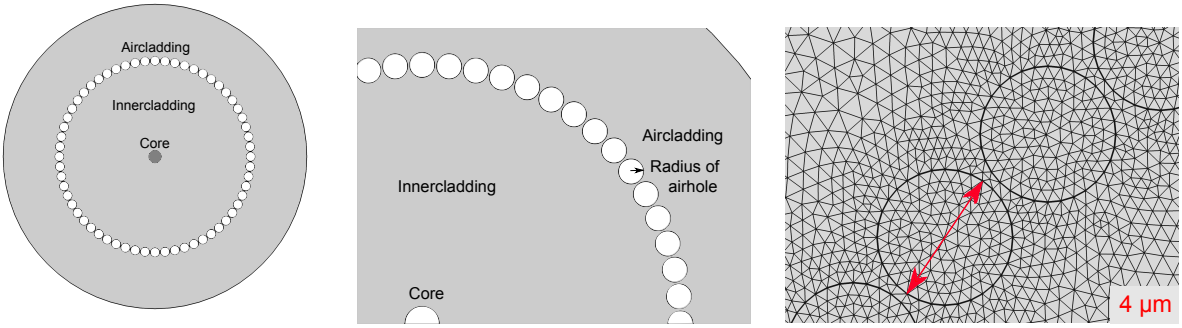

(a) (b) (c)

Figure 4.3: (a) Sketch of the simulated fiber geometry. (b) Zoom-in on the airholes in the simulated fiber geometry. (c) Zoom-in on the mesh in the aircladding region where the mesh has the finest structures. The length of the arrow is as indicated in the figure 4 μm.

As the holes become smaller, a smaller amount of field interacts with the holes, the bowtie effect is expected to be less pronounced [78]. Using the full vectorial modesolver, it has been demontrated that for mode orders above a certain threshold, the azimuthal symmetry is broken and the mode assumes a bowtie shape [78]. For every mode order, there are two degenerate solutions where the orientations of the bowties are orthogonal. The degeneracy of the solutions allows for every orientation of the bowtie by linear combination. In Fig. 4.4, the bowtie modes of orders 11, 14, and 16 are plotted in both orientations. Here it is seen that the pronouncement of the bowtie effect increase with mode order.

The grid size for the simulation is chosen so that the shape of the mode does not change when choosing a finer resolution. In Fig. 4.5a, a simulated modal image of BT_{011} for a hole radius of 2 μm is depicted, the chosen fiber geometry, depicted in Fig. 4.3a, is a close approximation to the fiber investigated experimentally. Here the bowtie effect is seen. The normalized variation in the first norm squared of the transverse electric field vector along the first ring in the mode is plotted in Fig. 4.5b, along the arrow indicated in Fig. 4.5a. A sinosoidal variation which is not present for ideal LP_{0X} modes is observed, the threshold for the onset of the bowtie effect

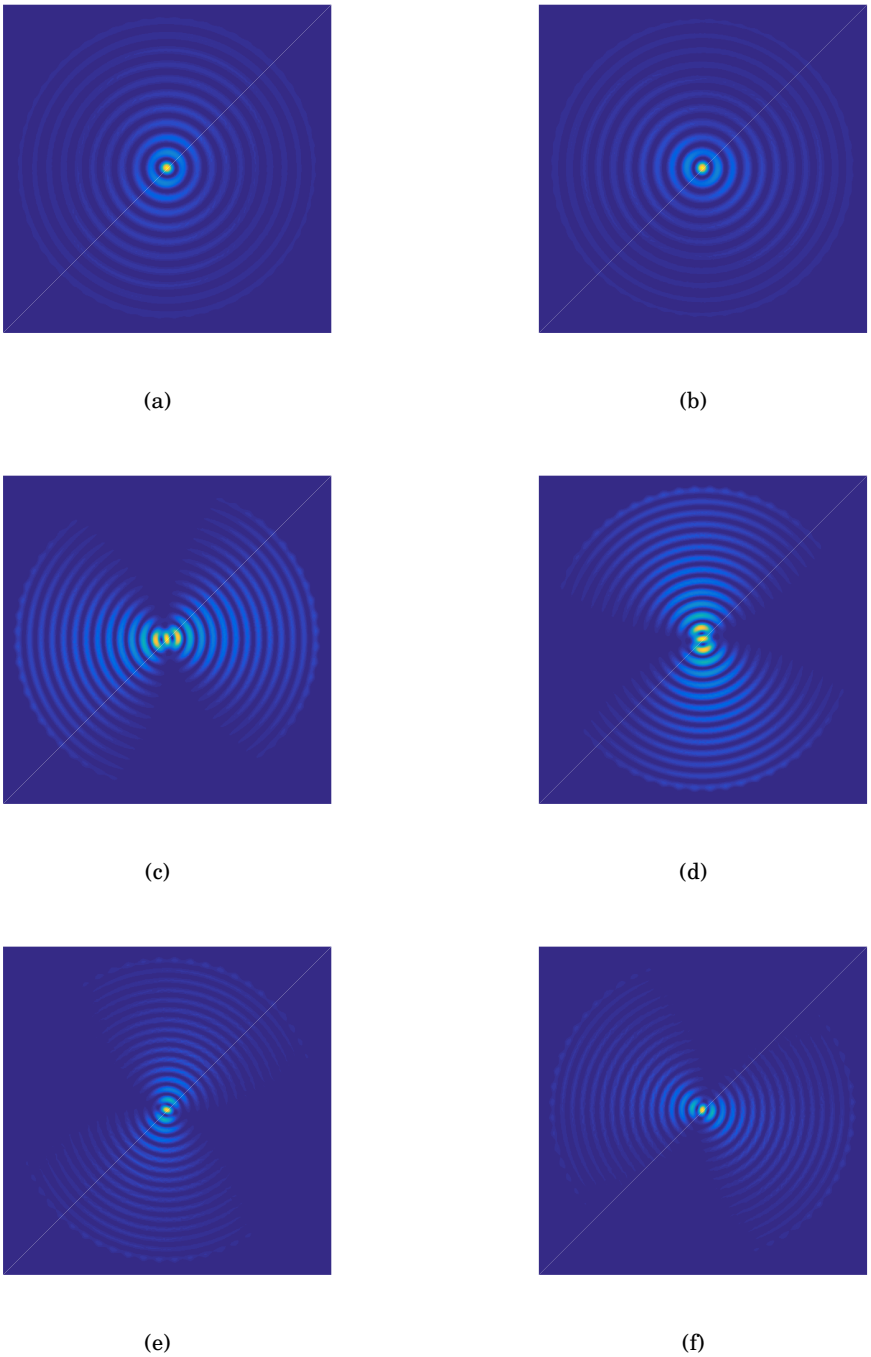

(a) (b)

(c) (d)

(e) (f)

Figure 4.4: Plots showing the two degenerate bowtie solutions for three different mode orders in the aircladding fiber with a hole radius of 2 μm. (a), (b) $BT_{011a,b}$. (c), (d) $BT_{014a,b}$. (e), (f) $BT_{016a,b}$

is predefined to a 25 % variation [78]. Thus it may be concluded that the onset of the bowtie effect for $r = 2$ μm is BT_{011}. As seen in Fig. 4.5b the bowtie effect is not above threshold for lower hole radii and it may be concluded that the threshold is for higher mode orders as the

bowtie effect becomes more pronounced with increasing mode order as also seen in Fig. 4.4. The rippling in the curves originates from the fact the this analysis is performed on the data set up in a cartesian system.

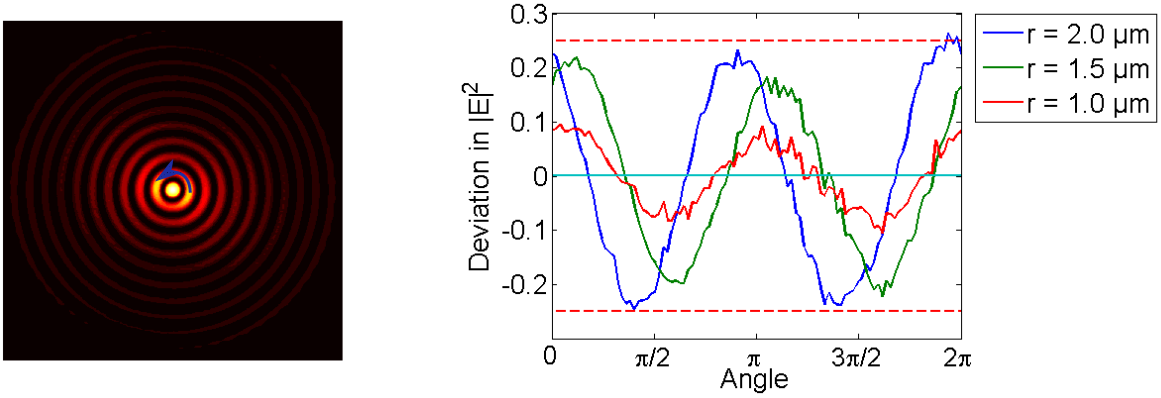

(a) (b)

Figure 4.5: (a) BT_{011} in aircladding fiber where the airholes have a radius of 2 μm. The deviation in the first norm square of the transverse electric field vector is to be evaluated along the first ring in the mode. (b) Deviation of the first norm square of the transverse electric field vector along the first ring in BT_{011} guided in the aircladding fiber, the radius of the airholes are varied and the number of holes are conserved.

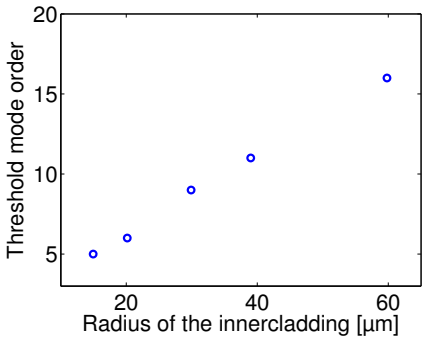

Figure 4.6: Onset of the bowtie effect as a function of the radius of the innercladding.

Numerical analysis also shows a large dependence on fiber design such as the radius of the inner cladding, which makes it an important effect to consider in designing optical fiber systems employing HOMs [78]. For smaller radii the bowtie sets in for lower mode order. In Fig 4.6, the onset of the bowtie effect given by the radial mode order is plotted as function of the radius of the innercladding. The fiber geometry is an aircladding geometry as the one depicted in Fig. 4.3a. In this analysis, the radius of the airholes and the width of the bridges is maintained, indicating that when reducing the radius of the innercladding the number of holes in the aircladding is reduced. The radius of the airholes and the width of the silica bridges is

maintained as a dependency of the airhole radius on the onset of the bowtie effect has just been demonstrated.

To exclude the ellipticity as the source of the bowtie effect, a numerical study of an elliptical fiber is conducted. Without loss of generality, the studied fiber is scaled down for better resolution. A step index fiber with an NA of 0.22 guiding LP_{02} but not LP_{03} is studied to investigate the origin of the bowtie effect by stepwise making the fiber elliptical. With a ellipticity of 0.2, an effect similar to the bowtie effect is observed but with two notable differences. The first difference is that in the elliptical fiber, the bowtie is always oriented along the semi-major axis in the ellipse, which does not allow for all orientations of the bowtie, which have been observed experimentally [78]. The second difference is the fact that all solutions for the elliptical fiber are linarly polarized. In the next section it is demonstrated that it is not the case for bowtie modes. Ellipticity is thus not the source of the bowtie effect [78].

To illustrate the effect of the ellipticity, the LP_{02}/BT_{02} modes for varies degrees of ellipticity is plotted in Fig. 4.7 in a step index fiber with the ellipticity along the vertical axis.

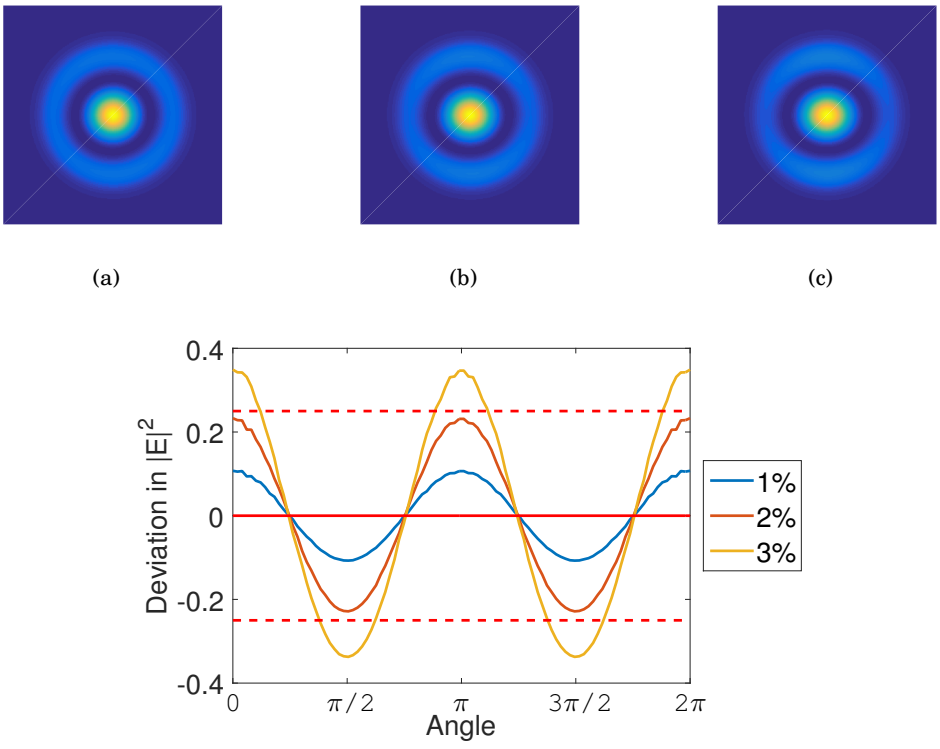

Figure 4.7: Imaging of the LP_{02}/BT_{02} modes for varies degrees of ellipticity in a step index fiber with the ellipticity along the vertical axis. (a) Ellipticity of 1%. (b) Ellipticity of 2%. (c) Ellipticity of 3% (d) Threshold for the onset of a bowtie-like effect.

It is expected that the bowtie effect can be attributed to the fact that the boundary conditions

of the radial and the azimuthal component of the electric field are different, thus with increasing field at the boundary as a result of the increasing mode order the effect becomes more dominant and the solutions for the two components differs yielding a resulting bowtie power distribution [78]. It is an effect also expected in an ideal circular fiber as since it is in fact a full vectorial effect and has been shown experimentally in a simple fiber structure [83]. The effect could be an analogue to the effect for hollow core fibers described in a ray picture by Golowich [85]. That is elaborated in the following section.

When considering the modes in the vectorial description, that is strong guiding, there are two contributions from Bessel modes of different orders to the HE_{1X} modes, which is the accurate description of the LP_{0X} modes considered in the scalar approximation. In the scalar approximation where the electric and magnetic field of the LP_{0X} modes are described by the J_0-Bessel function. From Okomato, the electric and magnetic field in the core region in polar coordinates may be written as [2]:

$$E_r = -iA\beta\frac{a}{u}\left[\frac{1-s}{2}J_{n-1}\left(\frac{u}{a}r\right) - \frac{1+s}{2}J_{n+1}\left(\frac{u}{a}r\right)\right]\cos(n\theta+\phi). \tag{4.1}$$

$$E_\theta = iA\beta\frac{a}{u}\left[\frac{1-s}{2}J_{n-1}\left(\frac{u}{a}r\right) + \frac{1+s}{2}J_{n+1}\left(\frac{u}{a}r\right)\right]\sin(n\theta+\phi). \tag{4.2}$$

$$H_r = -iA\omega\epsilon_0 n_1^2\frac{a}{u}\left[\frac{1-s_1}{2}J_{n-1}\left(\frac{u}{a}r\right) + \frac{1+s_1}{2}J_{n+1}\left(\frac{u}{a}r\right)\right]\sin(n\theta+\phi). \tag{4.3}$$

$$H_\theta = -iA\omega\epsilon_0 n_1^2\frac{a}{u}\left[\frac{1-s_1}{2}J_{n-1}\left(\frac{u}{a}r\right) + \frac{1+s_1}{2}J_{n+1}\left(\frac{u}{a}r\right)\right]\cos(n\theta+\phi). \tag{4.4}$$

where A is a constant, β is the propagation constant, a is the core radius, u is the transverse wave number, s is a constant depending on n and the transverse wave numbers in the core and cladding (u, w, respectively), likewise with s_1, n_1 is the refractive index in the core, and ϕ is the offset in the phase. Only the r- and θ-components are considered as they are the only contributing factors to the measured intensity proportional to the z-component of Poyntings vector, $S_z = E_r H_\theta - E_\theta H_r$.

From Eq. (4.1)-(4.4), it is evident, that in the full vectorial description of the HE_{1X}/LP_{0X} modes there is a second contribution in form of the J_2-Bessel function as well as an azimuthal dependence proportional to $cos(n\theta+\phi)$. This becomes increasingly dominant when increasing the refractive index difference and/or the mode order.

A second feature adding to the bowtie effect is the fact that for most fibers, HE_{1X} and EH_{1X-1}, which is part of the LP2X mode group in the scalar approximation, are nearly degenerate. For increasing mode order and increasing refractive index contrast, this effect becomes more dominant. This effect is not a feature, which is a problem in the realization of the bowtie modes which are excited using an LPG which uses the refractive index difference as well as on axis pertubation of the refractive index and thus couples to a symmetric mode. Rishøj *et al.* excites the bowtie modes using an SLM and are thus dependent on the intensity profile, which is

similar for the two modes when entering the bowtie regime, and as much as 3 dB is thus coupled into the undesired mode [83].

4.2 Polarization effects of bowtie modes

As the bowtie effect sets in the polarization of the modes is no longer linear [78, 83]. That it is also one of the features that separates the effect from the effect seen for elliptical fibers, where the mode with azimuthal dependency in the intensity distribution are linearly polarized. In this section, the nature of the polarization of the bowtie mode is reviewed. In Fig. 4.8a, the BT_{016}

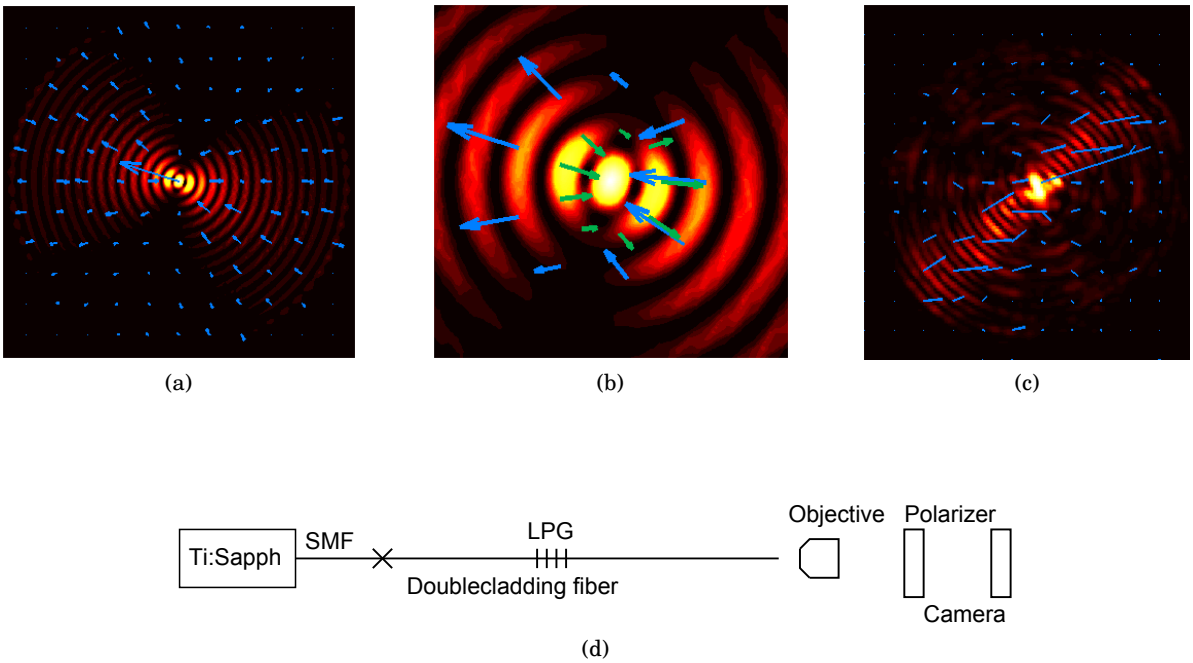

Figure 4.8: (a) BT_{016} mode found with the full vectorial modesolver for an aircladding fiber with a hole radius of 2 μm is plotted with arrows indicating the polarization. (b) Zoom-in on the central rings in the simulated mode. (c) Measured modal image with arrows indicating the polarization of the mode. There are no arrow heads as the measurement cannot distinguish a π-phase shift. (d) Setup for measuring the polarization state of the mode.

mode found with the full vectorial modesolver for an aircladding fiber with a hole radius of 2 μm is plotted with arrows depicting the polarization. It is seen that the polarization is orthogonal to the intensity rings in the mode [78]. In the zoom-in on the central rings of the mode in Fig. 4.8b, it is seen that there is a π-phaseshift between the polarization of the rings, as is the case for the linearly polarized mode LP_{0X}. The tail of the arrow is the point of evaluation. This non-linearity of the polarization sets in along with the bowtie effect, the LP_{0X} modes below the bowtie threshold are approximately linearly polarized. A gradual transition from the linearly polarized LP_{0X} mode to the non linear polarization configuration of the bowtie modes depicted

in Fig. 4.8b is not observed [78]. That is a result of the fact that evaluating the polarization configuration as a function of mode order is a discrete sampling, when instead maintaining the mode order and sweeping the wavelength, a gradual transition from a linearly polarized mode to the characteristic non-linearly polarized bowtie mode is found. The excitation of a bowtie mode is not dependent on a polarized excitation source showing the stability of the bowitue mode. The bowtie effect has been observed using an unpolarized excitation source [86].

In Fig. 4.8c, an experimental mapping of the polarization is depicted. The polarization is measured with the setup in Fig. 4.8d, the polarizer is turned and for every 10° an image is recorded. Summarizing the intensities for the different angles, it is possible to map the polarization of the mode however, only in an angle of π as the polarizer cannot discriminate a π-phaseshift and the polarization is depicted therefore without arrowheads [78].

Comparing to the experimental results with the numerical investigations, it is seen that the experimental realization shows the same tendency of a polarization orthogonal to the intensity rings in the mode. The purity of the mode and the dynamic range of the camera limit further comparisons of numerical and xperimental results.

Rishøj *et al.* concludes that, the two mode types exhibiting a bowtie like effect, namely the HE_{1X} modes and the EH_{1X-1} modes show two different type of polarization effects. Where as the HE_{1X} modes go from a linear polarization to a quasi-radially polarization with the onset of the bowtie effect, the EH_{1X-1} modes become quasi-azimuthally polarized [83]. Using this observation, it may be concluded that the modes excited in the aircladding fiber is of the HE_{1X} type.

4.3 Free space properties

One of the widely applicable properties of the Bessel-like modes is the diffraction resistant free space propagation, where the diffraction free propagation distance is increased up 36-fold [9]. To evaluate the performance of the bowtie modes, the free space propagation of the bowtie modes is compared against ideal LP_{0X} mode [78].

To find the diffraction free propagation distance experimentally, measurements on the BT_{016} mode depicted in Fig. 4.2b. The setup in Fig. 4.9a is used. Initially, the fiber is placed so that the mode at the end facet of the fiber is imaged onto the camera, the distance between the FUT and the objective is afterwards increased. The images of the mode upon propagation are stacked and a cross sectional line through the center of the stacked images is used to depict the free space propagation, the data along the horizontal axis is plotted in Fig. 4.9b. It is speculated, that the airholes in the outer cladding slightly distorts the mode which results in the lack of smoothness in the propagation measurement. In Fig. 4.9c, images from the free space propagation are plotted. Note that the bowtie shape is preserved throughout the propagation.

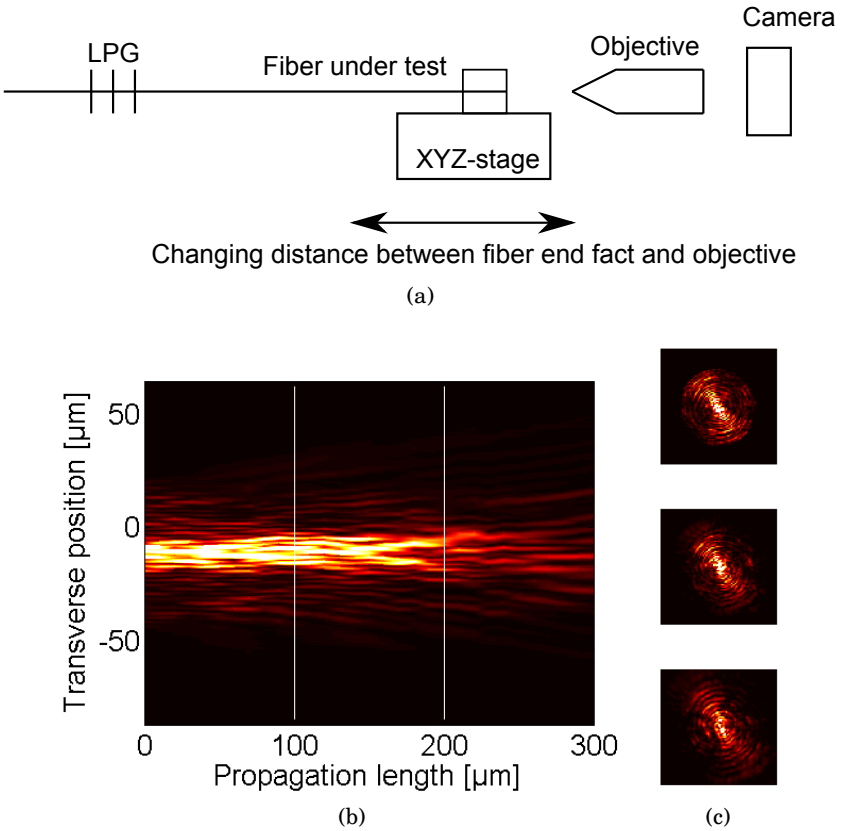

Figure 4.9: (a) Setup for measuring the free space propagation of a mode excited by a LPG. (b) Images from the measurements are stacked and plotted along a single axis - the horizontal axis in the mode images in (c). (c) Mode images after, from the top, 0 μm, 100 μm, and 200 μm of free space propagation.

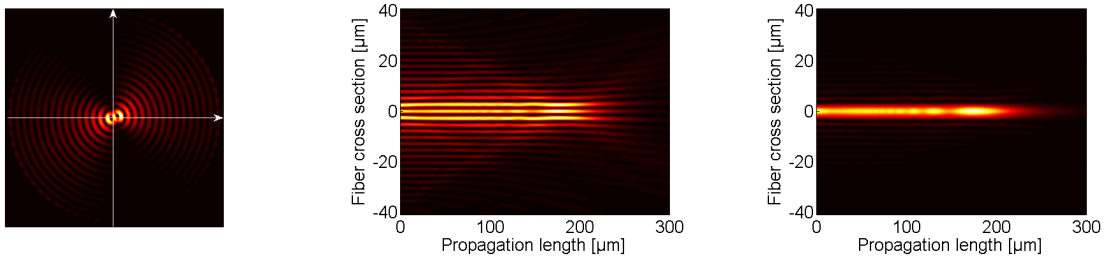

Figure 4.10: Numerical calculation of the free space propagation of BT_{016}. (a) Modal image of BT_{016} at 823 nm calculated for the aircladding fiber, where the holes have a radius of 2 μm. The axes along which the free propagation is imaged in (b) and (c) are indicated. (b) Free space propagation of BT_{016} along the horizontal axis. (c) Free space propagation of BT_{016} along the vertical axis.

A numerical calculation of the free space properties is performed using a FFT propagation

method based on the principles of Delen *et al.* [84]. The FFT propagation method is based on following equation:

$$A(x,y,z=L) = \mathscr{F}^* \left\{ \mathscr{F} \{(A(x,y,z=0)\} \cdot e^{-ik_z L} \right\},$$
$$kz = \sqrt{k_0^2 - (k_x^2 + k_y^2)}, \tag{4.5}$$

where A is the electric field, k_0 is vacuum wave number and k_x, k_y, and k_z are components of the wave vector, where k_x and k_y are found in the Fourier transform.

The contribution from E_z is neglected as it is at least 30 dB smaller than the contributions from E_x and E_y. The contributions from E_x and E_y are propagated separately and subsequently added [78]. The calculations are performed on BT_{016} at 823 nm found in the aircladding fiber where the holes in the aircladding have a radius of 2 μm in order to compare to the experimental investigation. The mode and the propagation along the horizontal and the vertical axis through the center of the mode are plotted in Fig. 4.10. The diffraction free propagation distance is defined as the point where the absolute value of the electric field squared in the center of the beam has dropped to e^{-1} compared to the point of maximum absolute value of the electric field squared [9]. The BT_{016} mode has a diffraction free propagation distance of 218 μm as compared to 216 μm for an ideal LP_{0X} mode found with a scalar mode solver for a similar fiber structure. The bowtie modes shows the same diffraction-resistant behaviour as the Bessel-like modes [9, 78]. When comparing to the experimental measurement, the diffraction free propagation distance is comparable to numerically predicted distance.

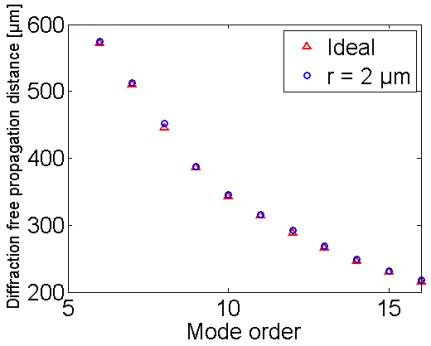

Figure 4.11: Diffraction free propagation distance as function of modeorder for LP_{0X} modes/BT_{0X} modes in an aircladding fiber and for ideal LP_{0X} modes found with a scalar mode solver.

The diffraction free propagation distance of LP_{0X} modes/BT_{0X} modes (dependent on whether or not the bowtie threshold is reached) guided in the aircladding fiber, where the airholes have a radius of 2 μm, is plotted as function of mode order and for the modes solved with the scalar modesolver for a similar stepindex fiber, see Fig. 4.11. Modes of lower order propagate unstably in any fiber [10], and they are thus not included in the plot. It is observed that the diffraction free propagation distances are much like that of the ideal Bessel-like modes [78].

4.4 Selfhealing

LP_{0X} modes are selfhealing, which means that they may regenerate their shape after an obstruction [9]. In this section, it is numerically investigated if bowtie modes also selfheal. Secondly the selfhealing is quantified [79].

The BT_{016} investigated previosly is considered again. The guided modes are found using a full vectorial mode solver, COMSOL. Part of the beam is blocked by an absorbent bar and the mode is propagated in free space using the FFT propagation routine used to consider the free space propagation in Sec. 4.3 [84]. In Fig. 4.12a, the mode immediately after the absorbent bar is depicted. To evaluate the angular dependency of the self-healing ability of the bowtie mode, the degree of self-healing is quantified by the overlap integral:

$$\eta = \frac{\left|\int \mathbf{E_p}^* \cdot \mathbf{E_{unp}} dA\right|^2}{\int |\mathbf{E_p}|^2 dA \int |\mathbf{E_{unp}}|^2 dA}, \tag{4.6}$$

where $\mathbf{E_p}$ is the perturbed electric field, $\mathbf{E_{unp}}$ is the unperturbed electric field, the integral spans across the full beam cross section. As for the free space propagation, only the transverse components of the electric field are considered. In Fig. 4.12b, the selfhealing overlap for BT_{016} with an absorbent bar at angle 0 is evaluated as function of the propagation length. The selfhealing overlap reaches a steady level maintained for at least 100 μm of free space propagation. The free space propagation of the mode after the absorbent bar is plotted along the first axis in Fig. 4.12c and along the second axis in Fig. 4.12d. The angular dependence of the selfhealing overlap is plotted in Fig. 4.12e. after 2 μm of free space propagation, where a steady overlap was reached. The selfhealing overlap follows a sinosoidal curve with minimum at the angle corresponding to the orientation of the bowtie.

4.5 Summary

Experimentally, it has been observed that guiding high order Bessel-like modes in an aircladding structure may lead to a break up of the azimuthal symmetry. This was verified numerically with a full vectorial modesolver, which shows that the break up results in two degenerate modes. The break up of the azimuthal the bowtie effect is named after the characteristic shape of the mode. The effect is showed not to originate from an ellipticity of the fiber.

The effect may instead be explained considering the full vectorial solutions to the wave equation, where the HE_{1X} mode is described by both the J_0-Bessel function, as its equivalent in the scalar approximation the LP_{0X} modes, and the J_2-Bessel function as well as an azimuthal dependence proportional to $cos(n\theta + \phi)$. The effect is dependent on the mode order and becomes stronger when going to higher mode orders and is vice versa dependent on the radius of the fiber and lowering the radius results in lowering the onset of the bowtie effect.

Once the effect sets in, the mode is no longer linearly polarized but instead orthogonal to the intensity rings in the mode.

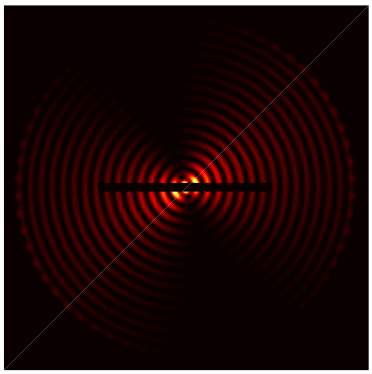

(a)

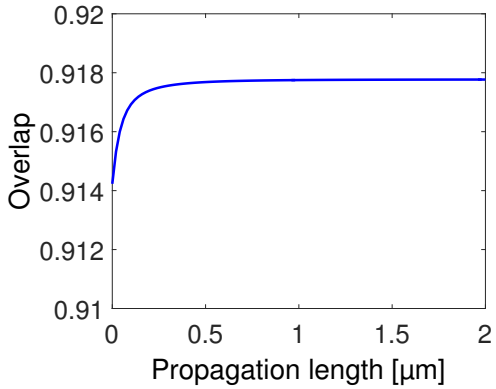

(b)

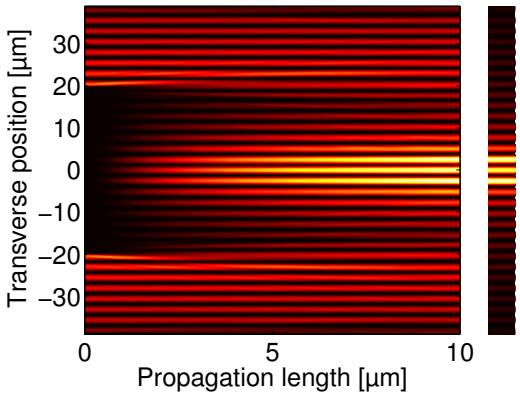

(c)

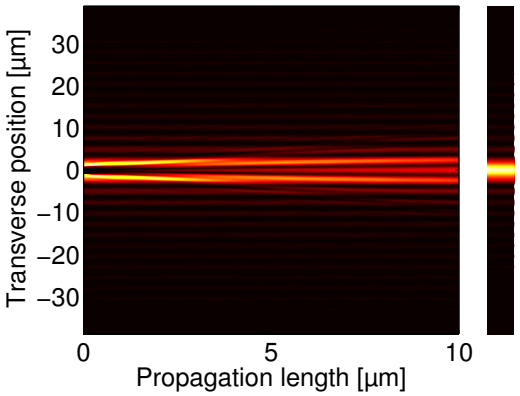

(d)

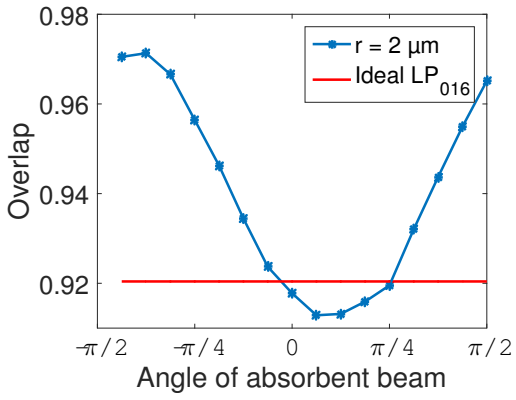

(e)

Figure 4.12: (a) The BT_{016} mode after the absorbent bar of length 40 μm and width 2 μm. (b) Selfhealing overlap as function of propagation length for the distorted mode plotted in (a). (c-d) Selfhealing in free space of BT_{016} plotted along the vertical and horizontal through the beam center, respectively. The unperturbed mode after 10 μm of propagation is plotted to the right. (e) Angular dependence of selfhealing overlap.

A second feature observed in the literature, is decreasing separation between the HE_{1X} mode group and EH_{1X-1} mode group, which both assume a bowtie like shape when increasing the mode order and/or the refractive index constrast. This feature was observed in a perfectly symmetric fiber.

The free space propagation of the modes are investigated both numerically and experimentally and the both investigations show that the modes may propagate just as far as the ideal Bessel-like modes and that the modes maintain their bowtie shape throughout the propagation.

Finally, the selfhealing properties are investigated and it is shown that the bowtie modes may regenerate themselves as do Bessel-like modes.

CHAPTER 5

CHIRPED MICROBEND LONG PERIOD GRATINGS

Broadband mode conversion have several applications e.g. within GVD compensation [11, 39, 87] which may be used in ultrashort pulse lasers [33, 34], but also within sensing [88]. The ability to achieve a broader and tailorable conversion bandwidth is highly desirable. This is possible either by engineering the fiber and using the TAP, e.g. the point where the group delay difference between the two modes in the conversion process is zero [11, 38, 39, 87] or as demonstrated in this chapter using a chirped LPG [89]. Chirped LPGs are a very versatile platform in terms of designing broadband mode conversion, as only design of the chirp of the LPG is required and the method is thus in principle applicable to all fibers. It has also been showed that chirped LPGs have a GVD compensating effect by them selves, this has been demonstrated both theoretically [90] and recently also experimentally [91]. Strong oscillatory spectral effects in chirped LPGs [92] have until recently limited their use, since the oscillatory spectral features are bandwidth limiting and results in unwanted highly oscillatory GVD [13, 88].

In this section, the focus is on broadband mode conversion. Chirped fiber LPGs for broadband mode conversion was first suggested by Östling *et al.* [37]. The scheme presented in this section elaborates on the idea presented by Östling and shows a straight forward way to implement linear and nonlinear chirp in a microbend LPG and was first presented by Israelsen *et al.* [89]. Microbend LPGs are due to asymmetric implementation limited to the mode conversion between symmetric and anti-symmetric modes [11].

Chirping have also been demonstrated for UV-induced LPGs [91, 92] which allows for coupling to symmetric modes.

The principle of implementation of chirped microbend LPGs used as mode converters is out-

lined in Fig. 5.1 [89]. However, instead of holding the FUT straight as is customary [31], the FUT

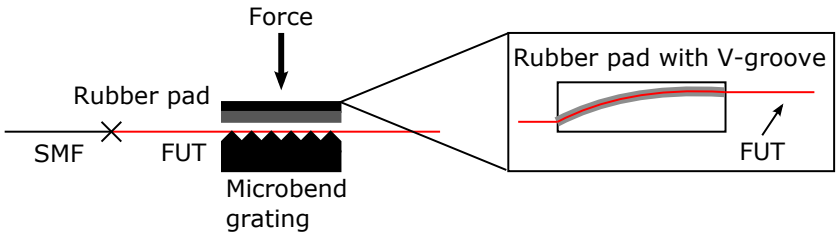

Figure 5.1: Principle of the chirped microbend LPG. The FUT is perturbed by a microbend LPG. The chirp in the LPG is made by a curved groove in the rubberpad used to press the FUT onto microbend LPG.

is curved upon the microbend LPG [89]. The curve is achieved by placing the FUT in a groove in the rubber pad pressing the FUT onto the microbend LPG fabricated in aluminum. The groove feature enables a simple and versatile tool for tailoring the chirp of the LPG; the shape of the groove principally defines the chirp.

Initially, a proof of principle of the method is presented. In this presentation, the shape of the chirp is not tailored to the specific fiber, and the full potential of the method is thus not demonstrated. In stead this section presents initial tries using grooves in the shape of circles with different curvatures.

5.1 Proof of principle

In this section, the effects of a chirped LPG based on the microbend setup presented in Fig. 5.1 are presented in a proof of principle matter. A few moded fiber is used as the FUT.

Initially, an unchirped mode conversion scheme is considered and the transmission of the fundamental mode through the mode converter as function of the conversion efficiency. The conversion efficiency given by the translation of the rubber pad to the microbend. When the rubber pad is moved, there is an increased force on the FUT and hence a larger conversion efficiency [89]. The FUT is a socalled vortex fiber where the full vectorial modes in the LP_{11}-mode group are non-degenerate [6].

To measure the transmission, the vortex fiber is spliced to a SMF. It is assumed that all the power equaling the measured loss is coupled into the desired mode. This is a standard procedure for determining the mode coupling [16]. The transmission is plotted in Fig. 5.2 for the conversion from the fundamental mode to the TE_{01}- and HE_{21}-modes. The pitch of the LPG is 800 μm. The two HE_{21}-modes are degenerate and thus represent the same dip in the transmission spectrum [93]. Increasing the translation of the rubber pad shows the effects overcoupling: Broader transmission bands accompanied by more spectral features.

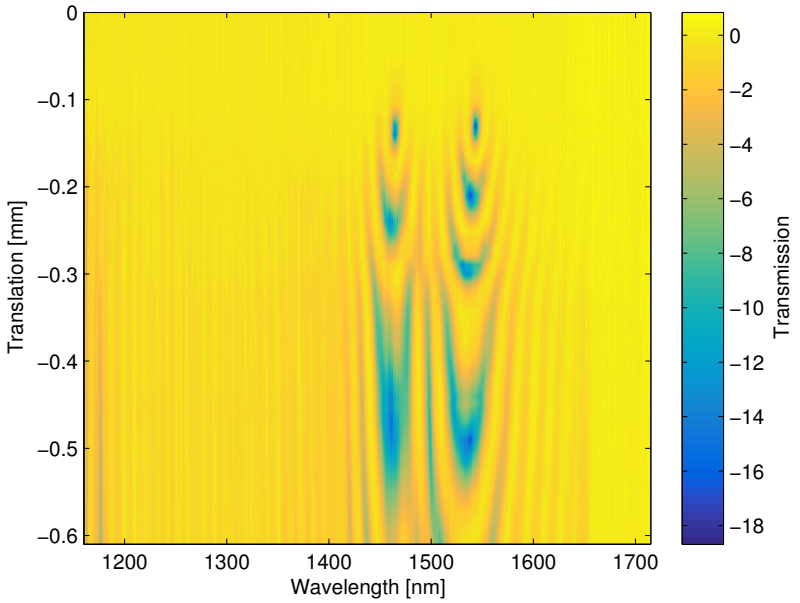

Figure 5.2: The transmission for the conversion from the fundamental mode to the TE_{01}- and HE_{21}-modes plotted as function of the translation of the rubber pad. The pitch of the unchirped LPG is 800 μm.

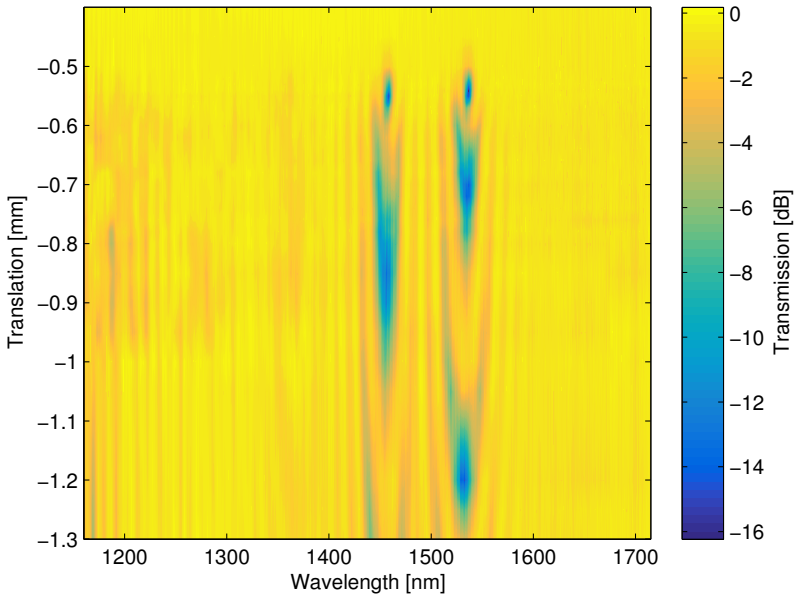

Figure 5.3: The transmission for the conversion from the fundamental mode to the TE_{01}- and HE_{21}-modes plotted as function of the translation of the rubber pad. The pitch of the LPG is 800 μm. The FUT is embedded in a circular arc groove with a radius of 30 cm in the rubber pad.

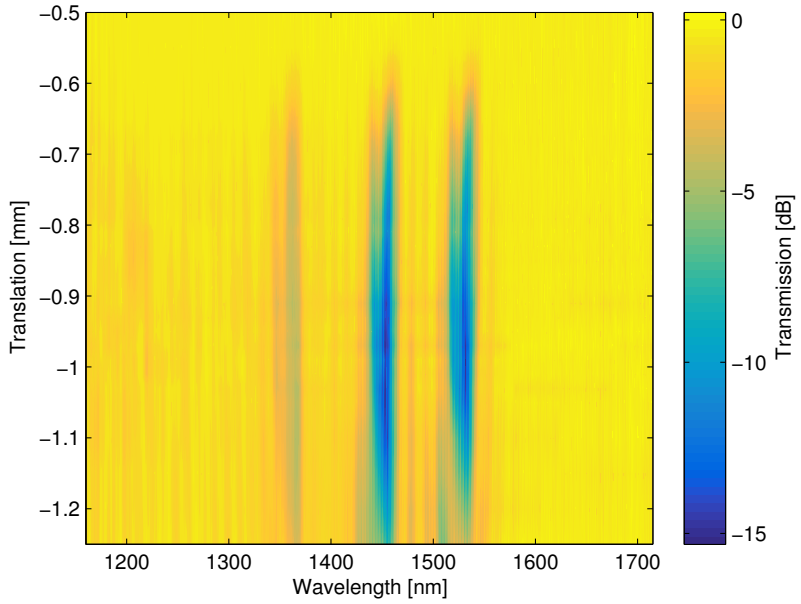

Figure 5.4: The transmission for the conversion from the fundamental mode to the TE_{01}- and HE_{21}-modes plotted as function of the translation of the rubber pad. The pitch of the LPG is 800 μm. The FUT is embedded in a circular arc groove with a radius of 20 cm in the rubber pad.

In Fig. 5.3 and 5.4, a chirped configuration of the measurement is presented. The chirp consist of a circular arc with a radius of 30 cm and 20 cm, respectively. The groove in the rubber pad is approximately half of the outer diameter of the FUT with coating that is approximately 250 μm. The smoothness of the groove in the rubber pad is very important as ripples in the groove adds extra unwanted pertubations resulting in uncontrolled mode coupling. Two conclusions are drawn from the results. First, more broadband conversion is achieved. Secondly, the conversion efficiency here represented by the translation of the rubberpad is needed to achieve conversion. This feature especially prominent for the measurement where the circular arc groove has a radius of 20 cm.

Despite the fact that the chirp is not tailored to the phase matching curves, a significant increase in the bandwidth of the mode conversion is observed. In Fig. 5.5, the best possible transmission for the conversion from the fundamental mode to the TE_{01}- and HE_{21}-modes in a non-overcoupled configuration is plotted. The dip at approximately 1370 nm respresents the conversion to the HE_{21}-mode group. The 10 dB conversion bandwidth is increased 1.3 times using the circular arc groove with a radius of 30 cm and 2.7 times for the circular arc groove with a radius of 20 cm. For the conversion to the TE_{01}-mode, at approximately 1470 nm, the 10 dB conversion bandwidth is increased 1.7 times using circular arc groove with a radius of 30 cm and 4 times for the circular arc groove with a radius of 20 cm.

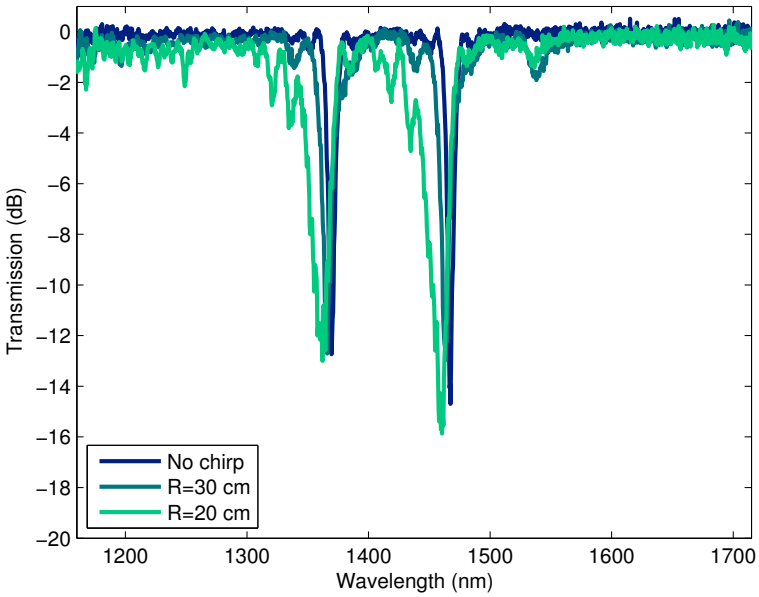

Figure 5.5: Comparison of the transmission spectra for the conversion from the fundamental mode to the TE_{01}- and HE_{21}-modes for the unchirped and two chirped LPG configurations in the vortex fiber. The transmission is plotted for the best conversion in non-overcoupled setup.

5.2 Numerical investigation

In this section, a numerical prediction of the effects of the chirped LPG is considered. Östling *et al.* limited their investigation to linearly chirped microbend LPGs [37]. Israelsen *et al.* also present nonlinearly chirped LPGs [89]. In this section, the coupled mode theory is used to simulate the conversion efficiency of the chirped microbend LPG [37], and the features of this method are reviewed. The two main equations governing the coupling process are given in Eq. (5.2), which describes the interaction between two co-propagating modes coupled by a z-dependent pertubation in the slow growth approximation [37, 94].

$$\frac{\mathrm{d}a_{01}}{\mathrm{d}z} = -i\kappa a_{11}\exp\left(i\int_0^z \Delta\beta(\lambda,x)\mathrm{d}x\right), \tag{5.1}$$

$$\frac{\mathrm{d}a_{11}}{\mathrm{d}z} = -i\kappa^* a_{01}\exp\left(-i\int_0^z \Delta\beta(\lambda,x)\mathrm{d}x\right). \tag{5.2}$$

where a_{01} and a_{11} are the complex modal amplitudes of LP_{01} and LP_{11}, respectively, κ is the coupling coefficient. The z-dependence of the pertubation is described by

$$\Delta\beta(\lambda,z) = 2\pi[1/L_B(\lambda) - 1/\Lambda(z)]. \tag{5.3}$$

where $L_B(\lambda)$ is the beat length between the two modes and $\Lambda(z)$ is the pitch of the LPG. The beat length is measurable quantity and is given by $L_B = \dfrac{\lambda}{\Delta n_{eff}}$ [95]. The pitch of the fiber may

be described as $\Lambda(z) = \Lambda_0 + \delta(z)$, where the perturbation, $\delta(z)$, describes the linear or nonlinear chirp. κ is the coupling coefficient proportional to the force applied to the rubber pad; κ is assumed constant along z. Changing κ along z would beneficial in the design of LPG spectra with reduced number of sidebands for GVD compensation [91]. However, this is difficult to implement in this scheme as it requires very high precision in the design of the rubber pad thickness as well as knowledge of the material properties of the used rubber. The coupled mode equations are solved numerically employing an ODE solver, as Eq. (5.2) does not yield a physically intuitive closed form solution [92].

To achieve the widest conversion bandwidth, a nonlinearly chirped LPG with pertubation in form of a 2nd order polynomial is employed. To find the set of coupled differential equations to implement in the ODE solver, the integral

$$\begin{aligned}\int_0^z \Delta\beta(\lambda,x)\mathrm{dx} &= \int_0^z 2\pi\left(\frac{1}{L_B(\lambda)} - \frac{1}{\Lambda(x)}\right)\mathrm{dx} \\ &= \int_0^z 2\pi\left(\frac{1}{L_B(\lambda)} - \frac{1}{ax^2+bx+c}\right)\mathrm{dx}, \end{aligned} \tag{5.4}$$

is solved. In the simple case, $b = 0$, the solution is:

$$\begin{aligned}\int_0^z \Delta\beta(\lambda,x)\mathrm{dx} &= \int_0^z 2\pi\left(\frac{1}{L_B(\lambda)} - \frac{1}{ax^2+c}\right)\mathrm{dx} \\ &= 2\pi\left[\frac{x}{L_B(\Lambda)} + \frac{\arctan\left(\frac{x}{\sqrt{ca}}\right)}{\sqrt{c*a}}\right]. \end{aligned} \tag{5.5}$$

The full solution is given by

$$\begin{aligned}\int_0^z \Delta\beta(\lambda,x)\mathrm{dx} &= \int_0^z 2\pi\left(\frac{1}{L_B(\lambda)} - \frac{1}{ax^2+bx+c}\right)\mathrm{dx} \\ &= 2\pi\left[\frac{x}{L_B(\Lambda)} + \frac{2\arctan\left(\frac{2ax+b}{\sqrt{4ac-b^2}}\right)}{\sqrt{4ac-b^2}}\right]. \end{aligned} \tag{5.6}$$

A TrueWave® fiber operated at approximately 800 nm, where it is fewmoded and guides LP_{01} and LP_{11} [89]. This fiber and not the vortex fiber considered for the proof of principle is used as the fiber is a simple weakly guiding step index fiber and vectorial effects can be neglected in the calculations. The object is to couple LP_{01} to LP_{11}. A higher order diffraction LPG to achieve phase matching [19]. The first order diffraction is not usable due to a mechanical constraint: For pitches comparable to the fiber diameter (that is including the coating), the mechanical grating is not able to bend and perturb the fiber.

To find the fitting parameters for the chirp, the measured beat length within the desired wavelength range is approximated with a second order polynomial using the longitudinal axis of the LPG as the independent variable of the fit. The second order polynomial is used in accordance with (5.4). The aim is to achieve broadband conversion without overcoupling around 800 nm

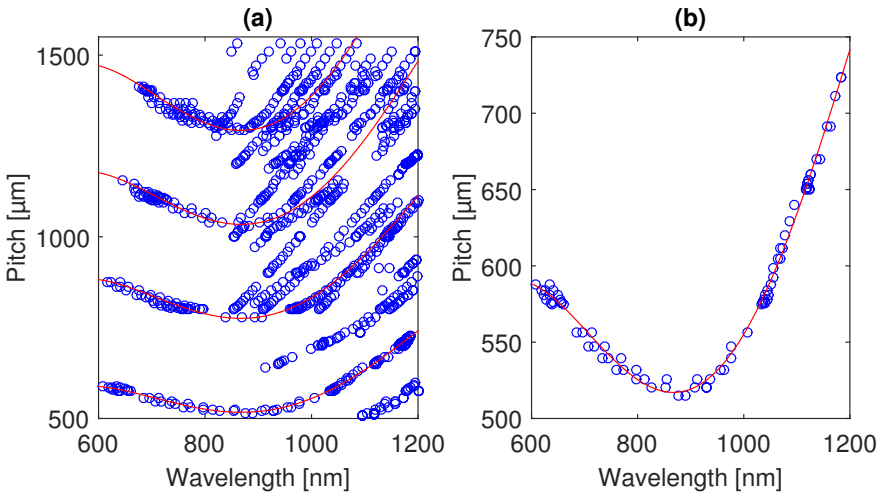

Figure 5.6: Phase matching curves for the conversion of LP_{01} to LP_{11} in a TrueWave® fiber operated in a fewmoded regime. (a) Full measurement of phase matching curves for higher order conversions corresponding to $\Lambda = 2L_B$, $\Lambda = 3L_B$, $\Lambda = 4L_B$, and $\Lambda = 5L_B$. The red lines in the plot correspond to 4th order polynomial fit in (b) scaled to the order of conversion. (b) Selected data for the pitch corresponding to $\Lambda = 2L_B$. The data is fitted to 4th order polynomial.

and the optimization of the chirp parameters is limited to the lower wavelength limit of the beat length measurement and the turn-around-point around 870 nm [38].

In Fig. 5.6(a), the full measurement of the beat length is plotted. The multiple curves are a result of the higher order diffraction and their sidebands [89]. The higher order diffraction curves are marked with a red line corresponding to the fit in Fig. 5.6(b) which is scaled to the diffraction order. The remaining points not following the red curves are sidebands. The first order diffraction is not achievable as previously explained. The phase matching measurement corresponding to second order diffraction is plotted in Fig. 5.6(b), where the order of the diffraction is identified from the full phase matching measurement in Fig. 5.6(a). The phase matching measurement for second order diffraction is fitted to a fourth order polynomial.

In Fig. 5.7 the transmission, that is the power remaining in the fundamental mode after the LPG, is plotted as function of the wavelength and conversion efficiency for an unchirped LPG with a Λ = 525 μm which corresponds to conversion at 800 nm employing second order diffraction. -20 dB transmission is achieved with a 1.8 nm bandwidth without overcoupling, that corresponds to the lowest conversion efficiency κ that allows for -20 dB transmission [89]. The transmission of a nonlinearly chirped LPG optimized for broadband conversion around 800 nm is plotted in Fig. 5.8 as a function of the wavelength and the conversion efficiency. With a -20 dB transmission across a 8.6 nm bandwidth, a 4.8-fold increase of the bandwidth is achieved [89]. The broadest conversion bandwidth is achieved when matching the chirp curve to broadest possible selection of the phase matching curve which in this case is from 649 nm to the TAP. As for the unchirped LPG, the transmission is found using coupled mode theory as described in

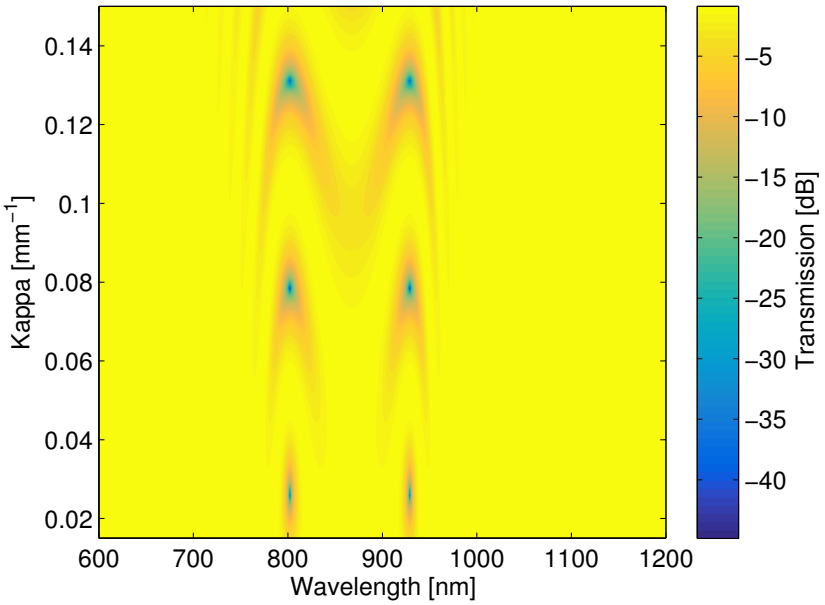

Figure 5.7: Transmission data for the conversion of LP_{01} to LP_{11} in a TrueWave® fiber operated in a fewmoded regime. The applied mode converter is an unchirped LPG with a pitch of 525 μm which corresponds to conversion at 800 nm.

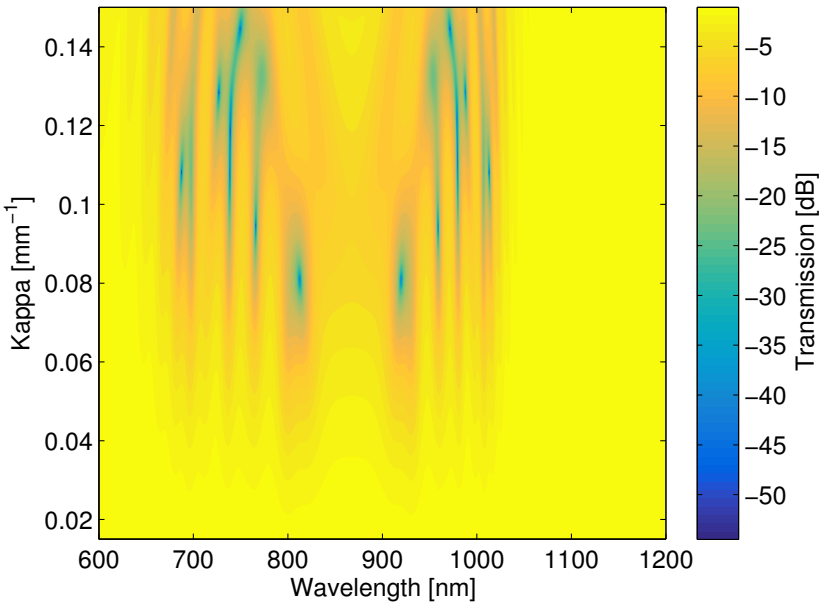

Figure 5.8: Transmission data for the conversion of LP_{01} to LP_{11} in a TrueWave® fiber operated in a fewmoded regime. The applied mode converter is a nonlinearly chirped LPG where the chirp is optimized for conversion around 800 nm.

Eq. (5.2) with the condition of Eq. (5.4). Note that the conversion to LP_{11} is achieved for higher values of the coupling coefficient, κ, corresponding to a larger force upon the rubber pad, hence there is a trade off between conversion bandwidth and possible permanent deformation and possible breakage of the fiber due to the larger load [89].

For closer examination, the transmission of the microbend LPGs in the chirped and unchirped configuration is plotted in Fig. 5.9 applying the conversion coefficient κ corresponding the largest possible conversion to LP_{11} without overcoupling. In this figure, it is evident that the chirped LPG has a significantly broader bandwidth, if the 3 dB bandwidth is considered, there is an 23-fold increment. However with conversion efficiencies of 0.026 mm^{-1} and 0.081 mm^{-1} for the unchirped and chirped configuration, respectively, the risk of permanent deformation of the fiber is much larger for the chirped LPG.

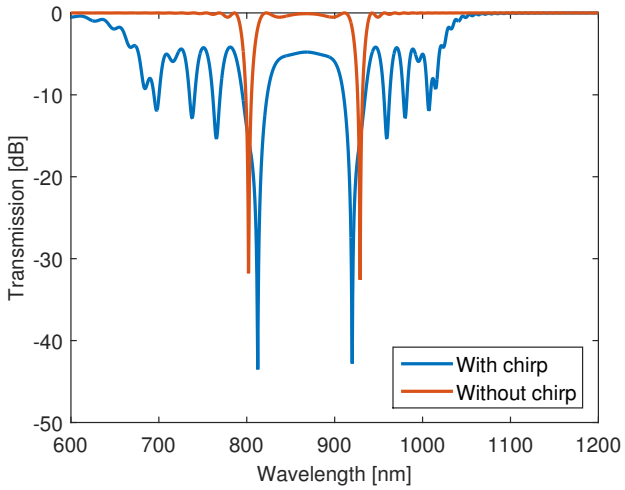

Figure 5.9: Transmission plot of the chirped and the unchiped LPG. For the chirped LPG, a conversion efficiency of 0.08115 mm^{-1} is applied and for the unchirped LPG, a conversion efficiency of 0.0258 mm^{-1}.

5.3 Experimental results

In this section, an experimental investigation of the tailored chirp configuration presented in the previous section is reviewed. For the experimental investigations, the shape of the V-groove must be designed according desired nonlinear chirp. Thus the parametric curve describing the chirp, $\mathbf{r}(u)$ is written as [89]

$$\oint_L = \int_0^z |\mathbf{r}'(u)| \mathrm{d}u = \Lambda(z). \tag{5.7}$$

Thus the line integral along the V-groove is equal to the pitch as function of z. This equation is however not easily solved. Instead, it is approximated with a piecewise linear function. To

carve a smooth curve in the rubberpad, the piecewise linear function is approximated with a third order polynomia [89]. The smooth curve is important to induce only the desired pertubation leading to mode coupling between LP_{01} and LP_{11}.

The chirp in this experimental realization is tailored to the phase matching curve as in the numerical calculation in Fig. 5.8. The transmission is measured by launching a broadband source in to the fundamental mode of the FUT as illustrated in Fig. 5.1 and after the chirped microbend LPG the FUT is spliced to a SMF (@ 800 nm). The transmission is measured as function of the translation of the rubber pad. In principle, the translation of the rubber pad is linearly proportional to the force on the rubber pad and thereby the conversion efficiency, κ, but due to mechanical restraints of the setup and the mechanical properties of the rubber pad, there is not complete linearity.

Initially, a reference measurement given by a nonchirped microbend LPG tailored for conversion at 800 nm corresponding to pitch of 525 nm is given. The transmission spectrum as function of the translation of the rubber pad is plotted in Fig. 5.10.

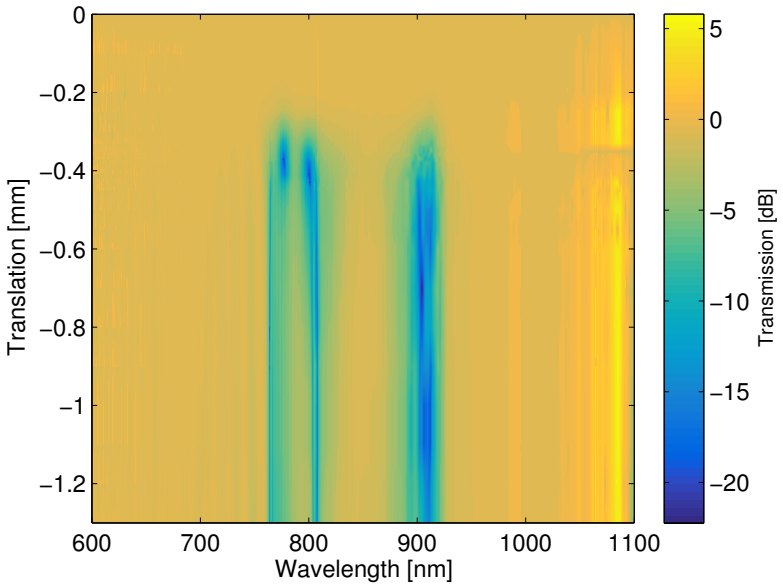

Figure 5.10: Experimental transmission data for the conversion of LP_{01} to LP_{11} in a TrueWave® fiber operated in a fewmoded regime. The conversion efficiency is given by the force applied to the rubberpad given in a unitless number. The applied mode converter is an unchirped LPG with a pitch of 525 μm which corresponds to conversion at 800 nm.

A transmission spectrum as function of the wavelength and the translation of the rubber pad for the nonlinearly chirped LPG is plotted in Fig. 5.11. In both the transmission spectrum of the chirped and the unchirped LPG, there are some features around 1050 nm independently of the translation of the rubber pad, which is a result of unstable excitation source, a supercontinuum

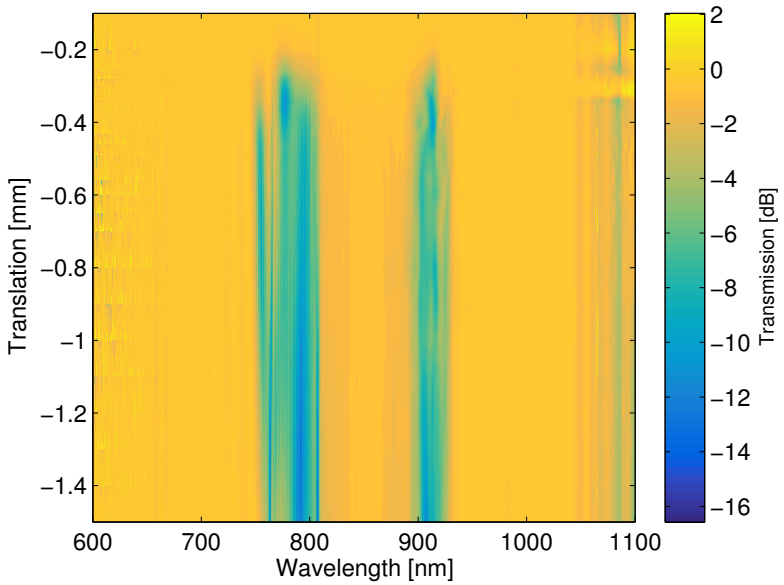

Figure 5.11: Experimental transmission data for the conversion from LP_{01} to LP_{11} in a TrueWave® fiber operated in a fewmoded regime. The conversion efficiency is given by the force to the rubber pad which is given by a unitless number. The applied mode converter is a nonlinearly chirped LPG where the chirp is optimized for conversion around 800 nm.

laser. These features are a result of the pump, and not the microbend LPGs.

In the experimental transmission spectrum of the nonlinearly chirped LPG, many of the same features as seen in the numerical results are observed. Unfortunately, the high conversion efficiency effects can not be measured. That is a result of the use of second order diffraction for the LPG demanding high conversion efficiencies and the mechanical constraint of a microbend LPG limiting the conversion to HOMs to what is possible without permanently damaging or potentially breaking the fiber [89]. The linearity between the plotted force and the conversion efficiency is also limited by the relaxation of the microbend LPG as described by G.-Nielsen *et al.* [31], however as a rubber pad is employed the relaxation is reduced compared to the effect described by G.-Nielsen *et al.*.

In Fig. 5.12, the best possible conversion for the chirped and the unchirped LPG in the TrueWave® fiber is plotted. In both the numerical and experimental studies, the chirped LPG requires a higher coupling efficiency, κ, - here given by the translation of the rubber pad - for optimum coupling [89]. There are several features to notice in this plot: The first thing is that the transmission plot for the unchirped LPG does not only show one dip as the simulations.It is expected that this is a result of the second order diffraction used [89]. The second is the squareness of the transmission spectrum for the chirped LPG, a feature which has been achieved without overcoupling and unwanted spectral oscillatory behavior [92]. This feature is especially attractive for GVD compensation using chirped LPGs [90, 91]. There is no significant broadening in

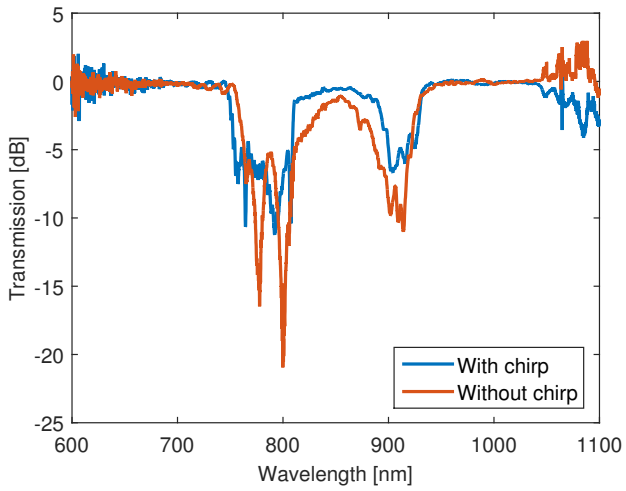

Figure 5.12: Measured transmission plot of the chirped and the unchiped LPG in the TrueWave® fiber. For the chirped LPG, translation of the rubber pad of -0.41 mm is used and for the unchirped LPG, a translation of the rubber pad of -1 mm is used.

the chirped LPG if both dips in the transmission spectrum close to 800 nm for the unchirped LPG are considered. However, recalling that the chirp was designed only for the dip at 800 nm. Using this fact, the conversion bandwidth is enhanced 2.7-fold at 5 dB conversion. Due to mechanical constraints of this system, it is not possible to achieve higher conversion efficiencies for this system, which would most likely have resulted in larger conversion. There is increased need for the high conversion efficiencies in this system due to the use of higher order diffraction [89]. Much higher conversion ratios are achievable as seen in Sec. 5.1.

5.4 Summary

A new and versatile platform for chirped LPGs coupling from a symmetrical to an anti-symmetrical mode and cylindrical vector modes has been demonstrated [89]. The transmission characteristics of this scheme has been modelled using coupled mode theory and a 4.8-fold increase of the bandwidth is achieved for conversion from LP_{01} to LP_{11} in a TrueWave® fiber operated in a fewmoded regime.

CHAPTER 6

IMAGING AS A CHARACTERIZATION TOOL

This chapter focuses on using imaging of the near field of a mode as a characterization tool. The chapter falls in three parts. Initially, the divergence angle as a quality parameter for HOMs in free space is considered. Secondly, phase retrieval of mode mixtures is presented. This procedure is used for retrieving size and phase of a field by considering a volume intensity measurement. Lastly, the near field of a pure HOM in a weakly guiding step index fiber is analyzed for determining the GVD.

6.1 Divergence Angle as a Quality Parameter for Fiber Modes

The parameter M^2 has earlier been suggested for determining the modal quality of a beam radiated from a fiber [65, 66]. M^2 compares the second order intensity moment at the beam waist to that of a Gaussian mode [65]. Wielandy shows that M^2 for modal mixtures may be indistinguishable from that of the fundamental mode and as such not a unique parameter for characterising beams emanating from a fiber [66]. For characterising modal mixtures, S^2 and C^2 have shown excellent results [70, 74]. Yoda *et al.* demonstrates high values of M^2 for pure HOMs in fibers indicating poor mode quality [65]. If the object is illumination with small divergence, it has recently been shown that LP_{0X}-modes may propagate in free space with small divergence [9]. The divergence angle is thus a more general parameter for the evaluation of the free space properties of pure fiber modes [22].

In this section, the use of the divergence angle as a quality parameter for the propagation of pure fiber modes in free space is considered. The divergence angle is formed using a volume measurement of the intensity exciting the fiber in free space. Using the divergence angle, the comparison of the second order intensity mode of HOMs against that of a Gaussian mode is

avoided and a modal parameter applicable for comparison of the free space properties of HOMs is obtained [22]. As proof of principle, the divergence angle of LP_{11} in a weakly guiding fiber is measured. The method may be generalized to other fiber modes and that is done numerically for modes in the LP_{0X}-, LP_{1X} and LP_{2X}-mode groups in a weakly guiding step index fiber. This section only considers weakly guiding step index fibers as the investigation carried out by Yoda *et al.* [65]. LP_{11} is not a true eigenmode of the fiber but for weakly guiding fibers the vector modes which constitutes LP_{11} are degenerate and the lack of a true eigenmode is not an issue.

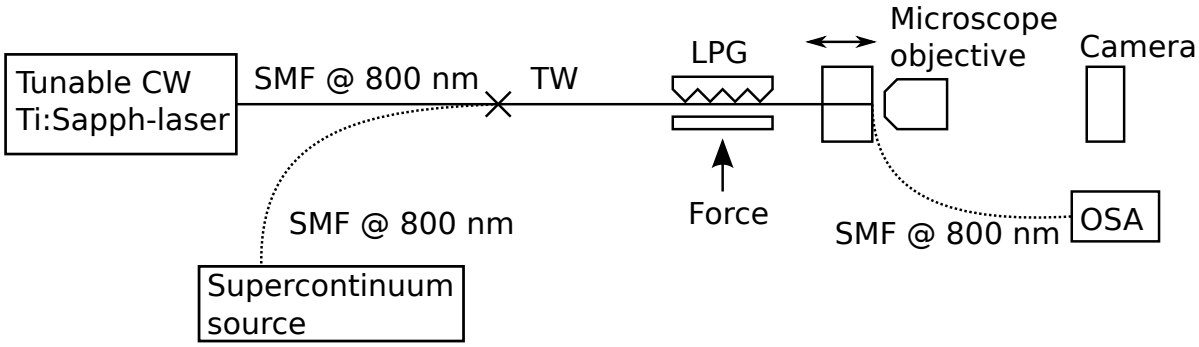

Figure 6.1: Setup for measuring the conversion efficiency (dotted SMF @ 800 nm) and the free space propagation (solid SMF @ 800 nm). CW Ti:Sapph-laser: Continuous wave Titanium:Sapphire laser. TW: TrueWave® fiber.

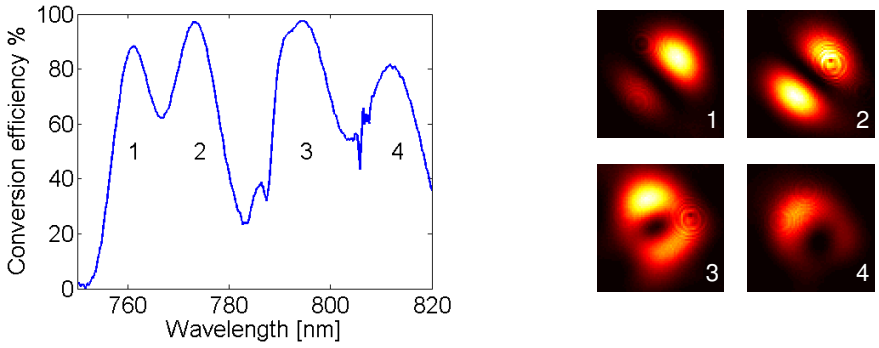

(a) (b)

Figure 6.2: (a) Conversion efficiency for the coupling to LP_{11}. (b) Modal images of the modes at the resonanses indicated in (a).

As a proof of principle, the divergence angle of the LP_{11} guided in a TrueWave® fiber at 773 nm, where the TrueWave® fiber is fewmoded, is measured [22]. The LP_{11} mode is excited using a microbend LPG to couple from the fundamental mode, LP_{01}. The microbend LPG consists of an aluminium block and a rubber pad to which a force is applied. The force is adjusted for maximum conversion efficiency. The LP_{11}-mode is excited using second order diffraction as the first order

diffraction is not accessible due to a mechanical constraint - the pitch of the LPG must be larger than the diameter of the fiber including the coating in order perturb the fiber, as the case of the chirped LPGs in Ch. 5.

The conversion effiency is measured with the setup in Fig. 6.1 using the connections with a SMF @ 800 nm indicated with the dotted lines which connects a supercontinuum source to the fiber guiding the HOM to an optical spectrum analyzer (OSA). The conversion efficiency is plotted in Fig. 6.2a and a maximum conversion efficiency of 97 % is obtained. The images of the modes at the conversion efficiency peaks are plotted in Fig. 6.2b. These are measured with the setup with the solid SMF @ 800 nm connections in the setup using a CCD camera. To map the free space propagation, the distance between the fiber end facet and the objective is increased - starting at the distance where the intensity profile at the fiber end facet is imaged onto the camera.

The divergence angle for a given fiber mode is determined at the divergence free propagation length, L_{prop}, which is the length where the maximum intensity has dropped with a factor of 1/e. The beam radius at the L_{prop} is determined by the $1/e^2$-intensity edge of the beam and the divergence angle may then be determined as the inverse tangent of the ratio of the beam radius and L_{prop} [22], a sketch is depicted in Fig. 6.3.

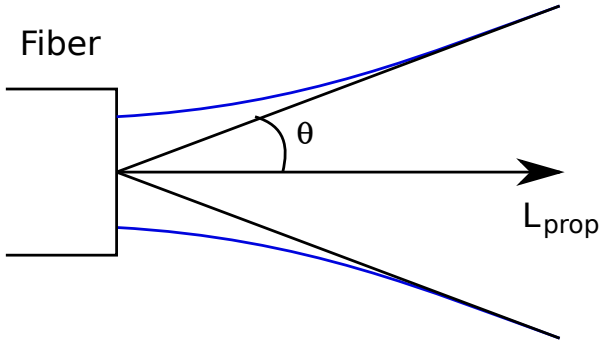

Figure 6.3: Definition of divergence angle, θ, determined as the inverse tangent of the ratio of the beam radius and L_{prop}.

The experimental results for the free space propagation of LP_{11} are depicted along one axis through the beam center in Fig. 6.4a. L_{prop} is determined to be 40 μm and the divergence angle to be 0.13. The experimental measurement of the free space propagation of LP_{11} are compared against numerical simulations. The modes in the TrueWave® fiber is found using a scalar mode solver. The free space propagation is simulated using a FFT routine applying the principles in [84], see Eq. (4.5), and depicted for LP_{11} at 773 nm along one axis in Fig. 6.4b. L_{prop} is determined to be 50 μm and the divergence angle to be 0.13 [22]. The divergence angle is thus determined with 2-digit accuracy and agreement between the numerical prediction and the experimental realization is observed. L_{prop} is also determined close to the numerical prediction.

In Fig 6.5, the divergence angle of all guided LP-modes as a function of the normalized

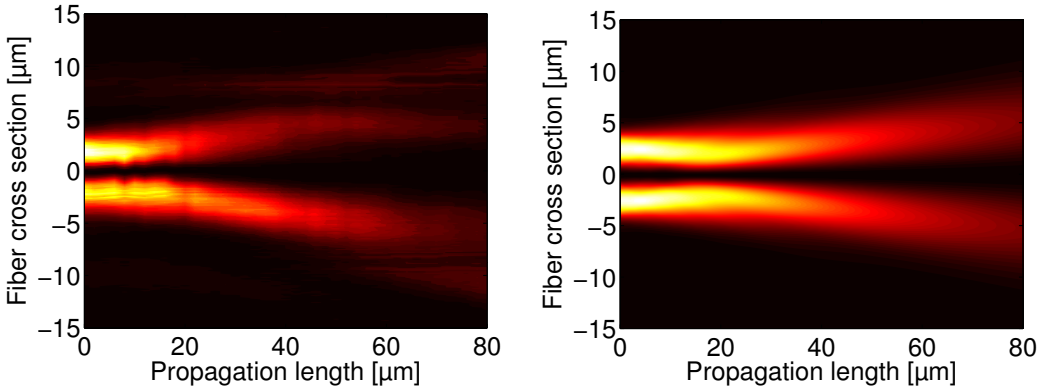

Figure 6.4: (a) Experimental measurement of the free space propagation length of LP_{11} guided in TrueWave® fiber at 773 nm plotted along the horizontal axis going through the beam center in Fig. 6.2b in the modal image of the second resonance. (b) Numerical simulation of the free space propagation length of LP_{11} guided in TrueWave® fiber at 773 nm.

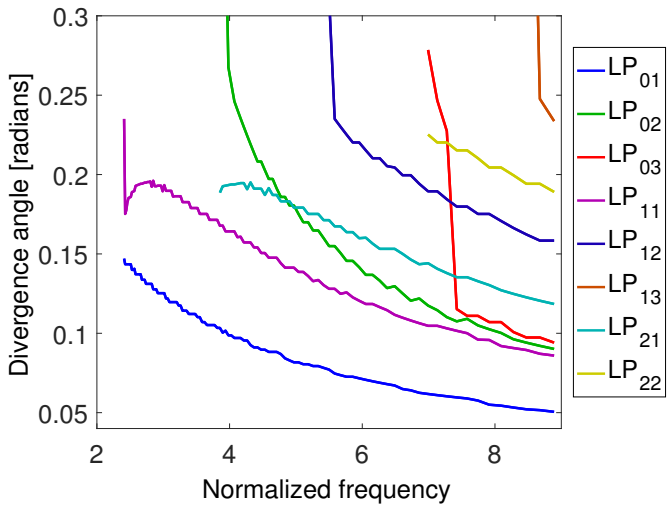

Figure 6.5: Divergence angle for fiber modes in a weakly guiding step index fiber as function of the normalized frequency.

frequency for a weakly guiding step index fiber is plotted. From the figure, the divergence angle for HOMs away from cutoff approaches that of the fundamental mode. It is expected that modes with the largest propagation constants diverges the least, indicating the fundamental mode always has the smallest divergence angle.

HOMs with large mode areas have been shown to have small bend losses [15].Some applications needs of large mode areas for instance to avoid nonlinear effects such as high power lasers [96]. Thus combining these two properties, one may operate in a single HOM and achieve a compact high power device with predictable free space divergence angle.

6.2 Phase retrieval - retrieval of the phase for pure and mixed modes

In this section, phase retrieval of mixed fiber modes are considered. Phase retrieval of fiber modes have been investigated earlier for mode decomposition purposes [68]. As discussed in Ch. 3, the mode decomposition presented by Shapira *et al.* considers fibers, where the eigenmodes of the fiber are well known [68]. In this section, a demonstration of the phase retrieval process on mixed modes in a weakly guiding step index fiber is presented. This is done in order to show that the field profile at the fiber end facet may be retrieved from an volume intensity measurement. Shapira *et al.* considers only the near and the far field, whereas this work shows phase retrieval measurements based on the procedure of volume speckle interferometry [97] where a series of intensity measurements are performed. It was shown, that the reconstruction improves with more intensity measurements [97]. The scheme is illustrated in Fig. 6.6. Initially, an image of the end facet of the fiber is recorded, afterwards the distance between the fiber end facet and the microscope objective (MO) is increased to record the volume intensity distribution.

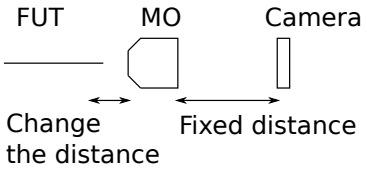

Figure 6.6: Setup for phase retrieval. A series of images is recorded, initiated by an image of the end facet of the fiber.

To find the phase, the electric field is propagated stepwise according to the principle of FFT propagation [84, 97]. To find the complete wavefront, it is assumed that at a given plane that (usually either the plane at the end facet of the fiber or the plane furthest away from the end facet of the fiber), the field amplitude can be described as $A(x,y,z) = \sqrt{I(x,y,z)}$, where $I(x,y,z)$ is the measured intensity. The phase distribution across the beam is initialized using a set of random numbers between -1 and 1. The phase in the final result is expected to be distributed between $-\pi$ and π and that would be the obvious starting guess, too large differences in the phase guesses does however lead to large boundary reflections which then lead to large distortions in the recovered mode. Knowing the amplitude and phase at a given plane, FFT propagation is used, see Eq. (4.5), to numerically propagate the field to the next plane. At the next plane, the phase distribution of the field numerically propagated and the square root of the measured intensity as the amplitude is used to propagate to the next plane. A numerical propagation to the third plane is then performed. This iterative process yields the phase distribution. This

process may be repeated, propagating back and forth through the measurement series as the homogeneous wave equation is time-reversible [98].

6.2.1 Numerical example

To demonstrate the principle, a numerical example is shown. A weakly guiding fiber with an NA of 0.149, operated at 850 nm that results in a V-number of 2.52, which means that the fiber is fewmoded, is considered. The guided modes of the fiber are found using a scalar mode solver.

A mode mixture of LP_{01} and LP_{11} is propagated in free space using FFT propagation. A 50/50 mix of the two modes with no initial phase difference is considered. An image of the fiber output is plotted in Fig. 6.7 along with across section of the free space propagation.

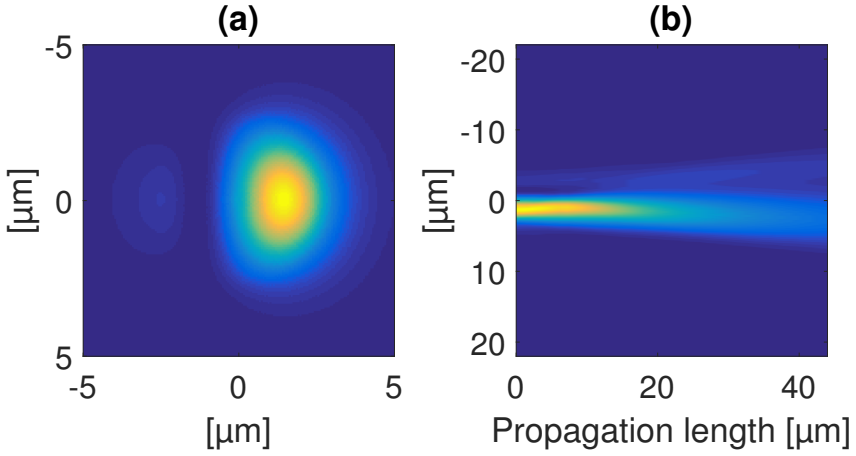

Figure 6.7: (a) Intensity plot of the simulated fiber. (b) A cross section of the free space propagation of the mode mixture plotted in (a). The cross section is the line through the origin along the horizontal axis.

The mode mixture is propagated in steps of 1 μm for a total of 44 μm. The phase retrieval algorithm is employed in a MATLAB scheme. A total of 15 iterations is used, starting furthest away from the fiber facet. The quality of the retrieved phase and intensity profile is strongly dependent on both the number of iterations and the step size. This was initially concluded by Almoro *et al.* [98], and the same effect is seen in these calculations. The minimum step size of 1 μm yields the best results and can the be applied for the experimental investigation, where this is the best achievable resolution in the z-direction with the present experimental setup. The retrieved phase and the initial phase is plotted in Fig. 6.8. The retrieved phase shows strong similarity with the initial phase, it may however only be retrieved in the region where the beam is defined. Another feature observed in the retrieved phase is the stripes in the phase as also described by Fienup [99].

The intensity retrieved in the phase retrieval process is plotted along with the initial phase in Fig. 6.9. The figure also shows the error made by the phase retrieval process which is at no

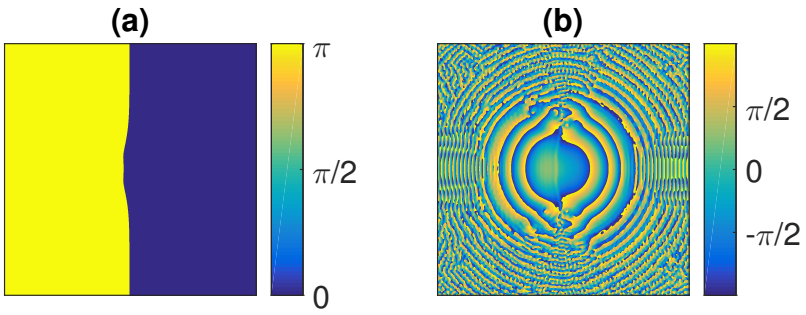

Figure 6.8: (a) The expected phase of the mode mixture in the simulated fiber. (b) The retrieved phase at the end facet of the fiber using a total of 15 iterations in the phase retrieval algorithm. Both plots are showing the full calculation space to illustrate the boundary effects.

pixel larger than 8 %.

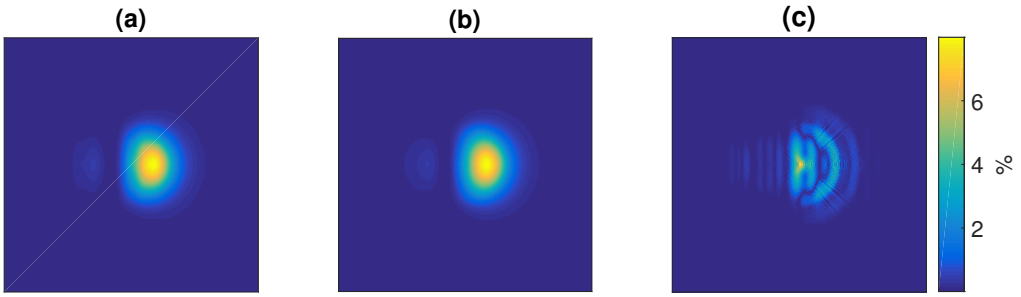

Figure 6.9: (a) The retrieved intensity of the mode mixture in the simulated fiber using the phase retrieval algorithm using a total of 15 iterations. (b) The input intensity of the mode mixture. (c) The error between the input and the retrieved intensity. All plots are slightly zoomed compared to the full calculation space to show the features within the mode mixture.

6.2.2 Experimental results

In this section, the phase retrieval process is performed on experimentally measured data. To perform numerical propagation of a measured field, the pixel size of the camera must be known. The microscope objective magnifies the beam, and the setup is calibrated using a mode of a known size. The fundamental mode of 780HP is imaged at 850 nm, where it is specified to have a mode field diameter of 5 ± 0.5 μm [100]. For the used setup, that results in a magnification of $98 \pm$

11. With a pixel size of the camera of 3.75 μm × 3.75 μm, the numerical Fourier transformations are performed with a spatial resolution of 0.0385 μm times 0.0385 μm. The camera has 960 × 1280 pixels.

The FUT is a TrueWave® fiber operated at approximately 800 nm, where it is fewmoded. A mechanical microbend grating is used to couple the fundamental mode to an LP_{11}-mode [11]. The conversion efficiency is plotted in Fig. 6.10. Larger conversion efficiencies may be achieved with microbend LPGs [11], but the conversion efficiency is limited to 90 %, for this demonstration of the phase retrieval method. A higher order diffraction LPG to achieve phase matching as for the investigated divergence angle [19].

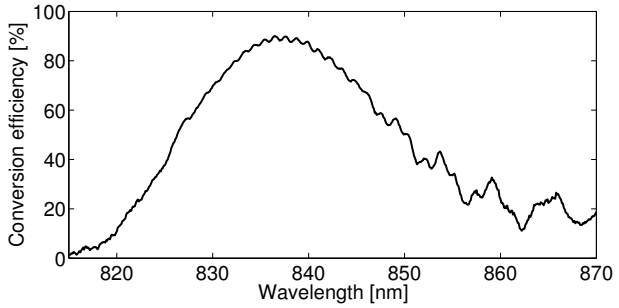

Figure 6.10: Conversion efficiency of the LPG converting the fundamental mode to LP_{11} in a TrueWave® fiber.

The phase distribution is retrieved at two different conversion efficiencies. Effectively, that is achieved by considering two different wavelengths, 837 nm and 850 nm, which corresponds to conversion efficiencies of 88.0 % and 50.4 %, respectively. A near field image of the two mode mixtures is seen in Fig. 6.11. For the phase retrieval at 837 nm 37 images are used, and at 850 nm 45 images are used.

The phase retrieval method is employed to retrieve the phase distribution for both conversion efficiencies, the result is plotted in Fig. 6.12. A very different number of iterations are used for the two modes mixtures. The same principle - of starting at the plane furthest away from the fiber end facet, first stepping backwards, then forwards, then backwards again and so on as presented in [98] - is employed for both measurements. Assuming no phase change at the fiber end facet, the phase distribution inside the fiber is found. At 837 nm where there is a dominating mode, 51 iterations is used, starting the phase retrieval process at the plane furthest away from the end facet. When using such a large number of iterations, a sign difference in between the lobes of in the mode mixture is retrieved as expected. For the mode mixture at 850 nm, only 3 iterations is used, using more iterations causes the boundary effects to dominate. Using only 3 iterations, the expected sign difference between the lobes in the mode cannot be found. It is expected, that a larger an measurement area could mitigate some of the boundary effects and thus allowing for the use of more iteration. Using more iterations would likely reveal a phase difference between the lobes. Note that as for the simulated mode the phase can only

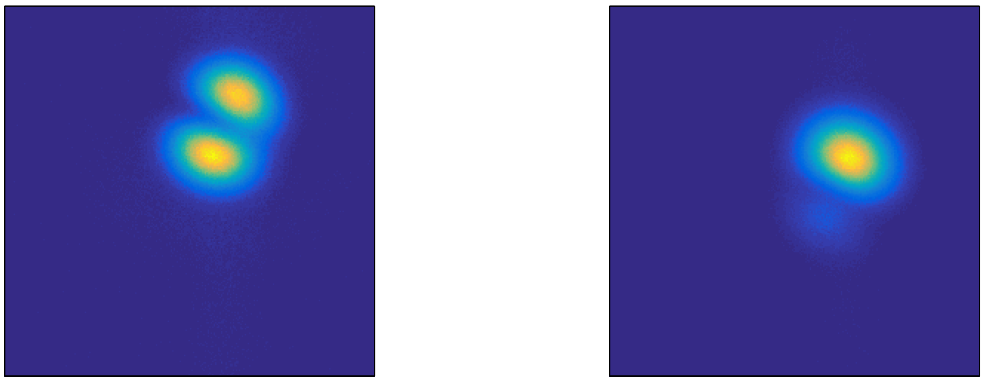

(a) (b)

Figure 6.11: Near field images of mode mixtures at (a) 837 nm and (b) 850 nm, which corresponds to conversion efficiencies of 88.0 % and 50.4 %, respectively.

be retrieved in the area where there is a signal. As opposed to the numerical example, there is no ripples in the retrieved phase, that is likely due to the background noise which acts as a smoothing mechanism.

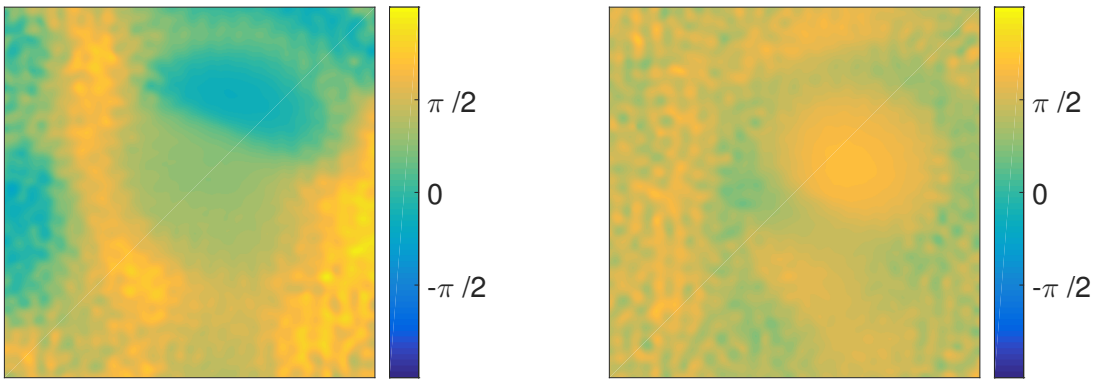

(a) (b)

Figure 6.12: The retrieved phase for the two mode mixtures (a) 837 nm using 51 iterations and (b) 850 nm using 3 iterations.

The retrieved intensity is plotted in Fig. 6.13 along with the measured intensity for both measured mode mixtures. Note that in the high intensity areas, the error in the retrived intensity is limited to 16 %. The error is significantly larger compared with the simulated fiber but that is expected due to originate from the background noise in the measurement.

Summing up, it is concluded that this very simple measurement setup is able to retrieve

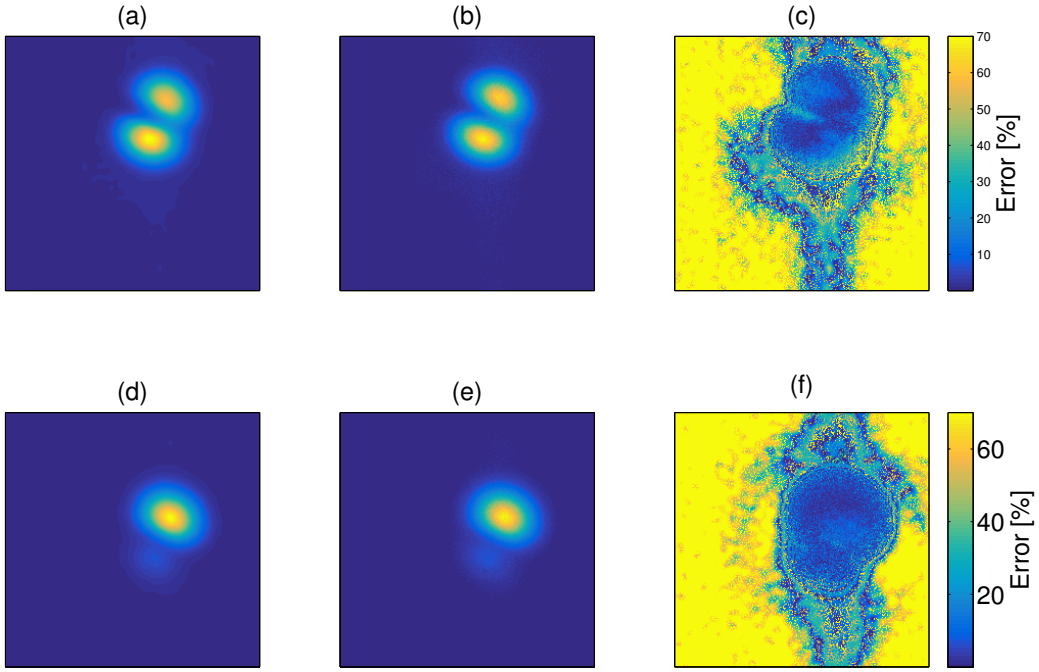

Figure 6.13: The retrieved intensity, the measured intensity and the error made the by the phase retrieval algorithm for the two mode mixtures (a), (b), (c) 837 nm using 51 iterations and (d), (e), (f) 850 nm using 3 iterations.

the phase of mode mixture, and that the retrieved intensity distribution is found with less than 16 % error in the high intensity areas.

6.3 Determining the Group Velocity Dispersion by Field Analysis for the LP_{0X}, LP_{1X}, and LP_{2X}Mode Groups Independently of the Fiber Length

Determining the GVD in optical fibers has been an important discipline for example for the design of optical resonators and amplifiers [33, 101] and for designing setups for parametric processes such as four wave mixing where the selection of the relevant HOM enables the process [63]. Standard techniques for measuring the GVD include time-of-flight measurements, phase shift measurements and interferometric techniques [101]. Both time-of-flight and phase-shift measurements require relatively long fiber lengths [101]. Stable propagation of HOMs in long lengths of fiber is difficult due to mode mixing and determination of the GVD using the standard techniques is thus not straight forward. A few demonstrations of GVD measurements of HOMs

using long fiber length have been demonstrated - however only in few moded fibers [39, 102]. Newer interferometric techniques include S^2 and C^2, though mainly developed for determining the modal content, these methods also yield the GVD of all modes in the decomposition [70, 73, 74]. S^2 and C^2 require fiber lengths in the order of meters and are both comparatively complicated setups as is customary for interferometric techniques. A simpler interferometric technique for measuring the GVD of a HOM was first presented by Menashe *et al.*; in this technique the fundamental mode and a selected HOM are exicted simultaneously and the modal beating is used to determine the GVD [103]. However, this method requires knowledge of the GVD of the fundamental mode.

In this section, the GVD is determined independently of the fiber length of weakly guiding step index fiber by determining the intensity profile of a pure mode in the near field as function of the wavelength. This method was first presentented by Israelsen *et al.* [104].
The only requirement for the determination of the GVD using this method is the field distribution of a purely guided mode, hence it is possible to use this method on very short fiber lengths as opposed to the other methods mentioned. A very simple method for determining the GVD of a HOM without the need for propagation of the mode which may result in mode coupling is here presented. The GVD of HOMs may thus be determined even in fibers where the HOM have poor propagation properties. Depending on the exciting source, the method is potentially very broadband. A predecessor for this method is the mode-field-diameter method, which considers a single mode fiber only and assumes that the field can be described by a Gaussian [105, 106]. In this work no such assumption is made [104].

Initially, the theory of the method is reviewed, then numerical results based on a multimoded fiber is presented, and lastly preliminary experimental results are presented.

The well known solution to the wave equation governing the field of a weakly guiding step index fiber in the core (and cladding) of the fiber is exploited [1]. It is assumed that for a weakly guiding fiber, the modulus of the field is proportional to the square root of the intensity. For weakly guiding fibers the radial field distribution in the core is described by $J_x(\kappa r)$, where κ is given by:

$$\kappa^2 = k_0^2(n_c^2 - n_{eff}^2), \tag{6.1}$$

and k_0 is the wave number, n_c is the refractive index of the core, and n_{eff} is the effective refractive index of the mode. Initially, following assumption is made for the refractive index of the core $n_c = n_{SiO_2}(\lambda) + \Delta n$, where $n_{SiO_2}(\lambda)$ is the refractive index of silica and Δn is the refractive index step between the core and the cladding [104]. The wavelength dependence of silica is given by Sellmeier's formula [1]. The wavelength dependence of germanium, which is generally used as index raising codopant of the core, is assumed to be negligible compared to

that of silica. n_{eff} can then be expressed as:

$$n_{eff} = \sqrt{(n_{SiO_2}(\lambda) + \Delta n)^2 - \kappa^2/k_0^2}. \tag{6.2}$$

The GVD parameter, D, may be determined by [1]

$$D = -\frac{\lambda}{c}\frac{\partial^2 n_{eff}}{\partial \lambda^2}. \tag{6.3}$$

Thus the parameter to determine is κ. In the following paragraphs, procedures to find κ is outlined. To a rough approximation the wavelength dependence of the square of the refractive index of the fiber core is equal to the wavelength dependence of silica: $n_c^2 \approx n_{SiO_2}^2$, and the expression for n_{eff}, see Eq. (6.2), simplifies as does the needed parameters for the FUT.

In the following section, the procedures to find κ for LP_{0X}, LP_{1X}, and LP_{2X} modes are outlined.

For the LP_{0X} modes, the normalized electric field strength is equal to $\Psi(r) = J_0(\kappa r)$ [1]. As there is no azimuthal dependence the orientation of the electric field, it is not considered for this mode group. The first step is to differentiate the radial dependence of the field: $\Psi'(r) = -\kappa J_1(\kappa r)$.

One approach to find κ could be to evaluate the maximum of the derivative which is κ, but the point of evaluation is for LP_{0X} very close to the core-cladding interface and there is uncertainty to the validity of the solution to the electric field strength. Secondly, this evaluation form also be strongly depends on the radial resolution of the field [104]. To have a method valid for all modes in the mode group, instead a Taylor approximation of $\Psi'(r)$ around $r = 0$ is calculated.

$$\begin{aligned} T_{LP_{0X}}(r) &= -\kappa J_1(0) - \kappa^2 \left(J_0(0) - \left.\frac{J_1(\kappa r')}{r'}\right|_{r'\to 0} \right) r \\ &\to -\frac{1}{2}\kappa^2 r \quad \text{for} \quad r \to 0. \end{aligned} \tag{6.4}$$

The derivative of the radial field distribution is then approximated with a straight line through origin to find κ [104].

For the LP_{1X} mode group, the azimuthal dependence may not be neglected. However considering the the radial dependence for the angle yielding the maximum intensity, it possible to omit the azimuthal dependence. The radial dependence of the LP_{1X} mode group may be described as: $\Psi(r) = J_1(\kappa r)$ [1]. Performing a Taylor expansion to first order directly on the radial field distribution around $r = 0$ yields:

$$\begin{aligned} T_{LP_{1X}}(r) &= \kappa J_1(0) + \kappa \left(J_0(0) - \left.\frac{J_1(\kappa r')}{\kappa r'}\right|_{r'\to 0} \right) r \\ &\to \frac{1}{2}\kappa r \quad \text{for} \quad r \to 0. \end{aligned} \tag{6.5}$$

This procedure is valid for all modes in the LP$_{1X}$ mode group. The radial field distribution is then approximated with a straight line through origin that can used to find κ [104].

As with the LP$_{1X}$ mode group, the azimuthal dependence of the LP$_{2X}$ mode group cannot be neglected. The same approach as for the LP$_{1X}$ mode group is used, the radial field dependence for the angle yielding the maximum intensity is considered. For the LP$_{2X}$ mode group it is necessary to differentiate the radial field distribution. The radial field distribution may be described by: $\Psi(r) = J_2(\kappa r)$. The derivative of the radial field distribution is then $\Psi'(r) = \kappa\left(J_1(\kappa r) + \frac{2J_2(\kappa r)}{\kappa r}\right)$. As for the LP$_{0X}$ mode group, a Taylor approximation on the derivative of the radial field distribution around $r = 0$ is performed.

$$\begin{aligned} T_{LP_{2X}}(r) =& \kappa\left(J_1(0) + \frac{2J_2(\kappa r)}{\kappa r}\Big|_{r\to 0}\right) \\ &+ \kappa\left[\kappa\left(J_0(0) - \frac{J_1(\kappa r)}{\kappa r}\Big|_{r\to 0}\right) + \frac{2J_2(\kappa r)}{\kappa r^2}\Big|_{r\to 0}\right. \\ &\left. - \frac{2\left(J_1(\kappa r) - \frac{2J_2(\kappa r)}{\kappa r}\right)}{r}\Big|_{r\to 0}\right] r \\ \to& \frac{1}{4}\kappa^2 r \quad \text{for} \quad r \to 0. \end{aligned} \tag{6.6}$$

The derivative of the radial field distribution is then approximated with a straight line through origin to find κ.

In principle, this form could be expanded to include HOM groups but at the expense of having to expand to higher orders in the Taylor approximation. The investigations are limited to the mode groups where the considered Taylor expansions are straight lines through origin [104].

6.3.1 Numerical results

In this section, a numerical example is presented. This does not represent all weakly guiding step index fibers but illustrates the workings of the method very well. A multimode step index fiber with a numerical aperture of 0.149 and a core radius of 8 μm is considered. The modes in the fiber are found with a scalar mode solver. The fiber supports all three considered mode groups.

Initially, the LP$_{0X}$ mode group is considered. In Fig. 6.14a, κ is plotted for all guided LP$_{0X}$ modes in the guided regions as function of the normalized frequency. The simulated κ from the scalar mode solver is also plotted as a dotted line. Excellent agreement between the simulated values of κ and the κ-values found by the Taylor approximation method is observed. The deviation in κ is less than 1 % for all modes considered [104].

In Fig. 6.14b, the GVD found numerically by differentiating the effective refractive index calculated using the κ found by applying the Tailor approximation method of the LP$_{0X}$ modes

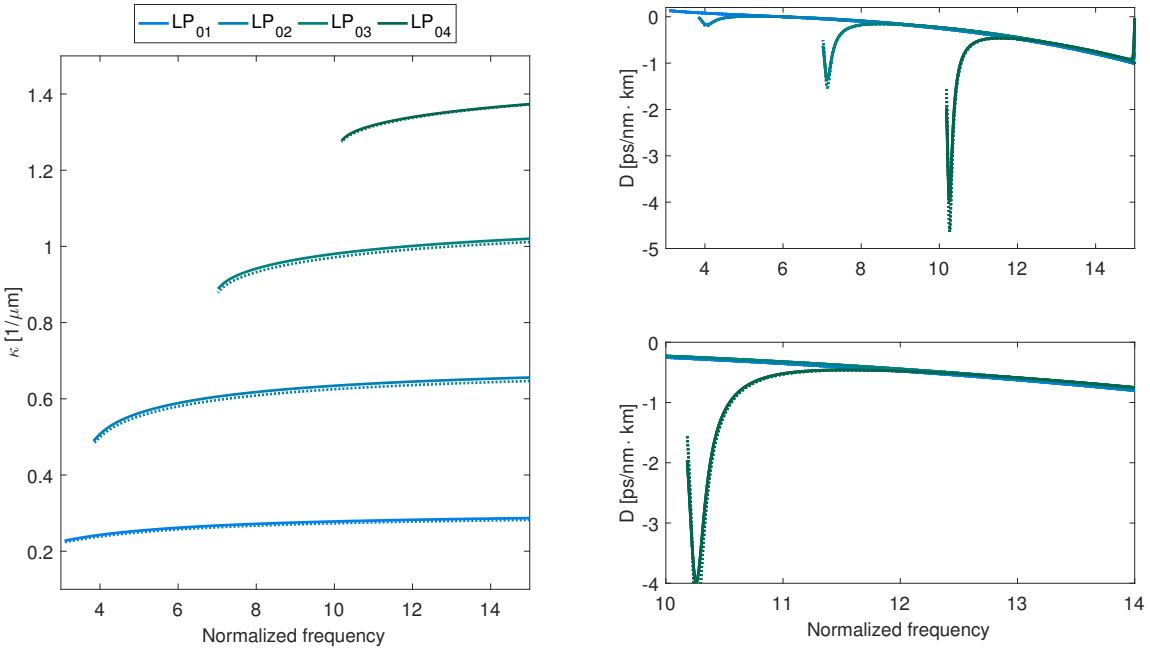

(a) (b)

Figure 6.14: (a) κ found using the Taylor approximation method on the differentiated radial mode field profile plotted for all guided modes in the LP_{0X} mode group. (b) The GVD found using κ is found. The plots are limited to above cutoff. The lower plot shows a zoom in of the GVD plot. For all plots the solid lines correspond to the Taylor approximation method and the dotted lines to the data from the scalar mode solver.

are plotted above cutoff along with the result for the GVD found with the scalar mode solver. Despite the approximation to the squared refractive index of the core, the method is able to very accurately determine the GVD. In the zoom in, the lower plot in Fig. 6.14b, it can be observed, that the method is sufficiently accurate for also determining the modal spacing in the GVD and the spacing in the ZDW [104] - both very important parameters in GVD tailoring using HOMs [33, 63].

In Fig. 6.15a, κ for the LP_{1X} mode group retrieved using the Taylor approximation method is plotted along with κ calculated by the scalar mode solver. Good accordance between the two data sets is observed, the deviation is less than 10 % for all considered modes in the mode group [104]. However, the data agreement decreases with mode order. That is a result of the resolution of the radial dependence of the electric field strength [104]. The resolution used in these simulations is 0.04 μm. In Fig. 6.15b, the GVD of the LP_{1X} mode group based on the data for κ is plotted along with the GVD found with the scalar mode solver. As for the LP_{0X} mode group, the GVD may be determined very accurately, this includes important figures such as the intermodal

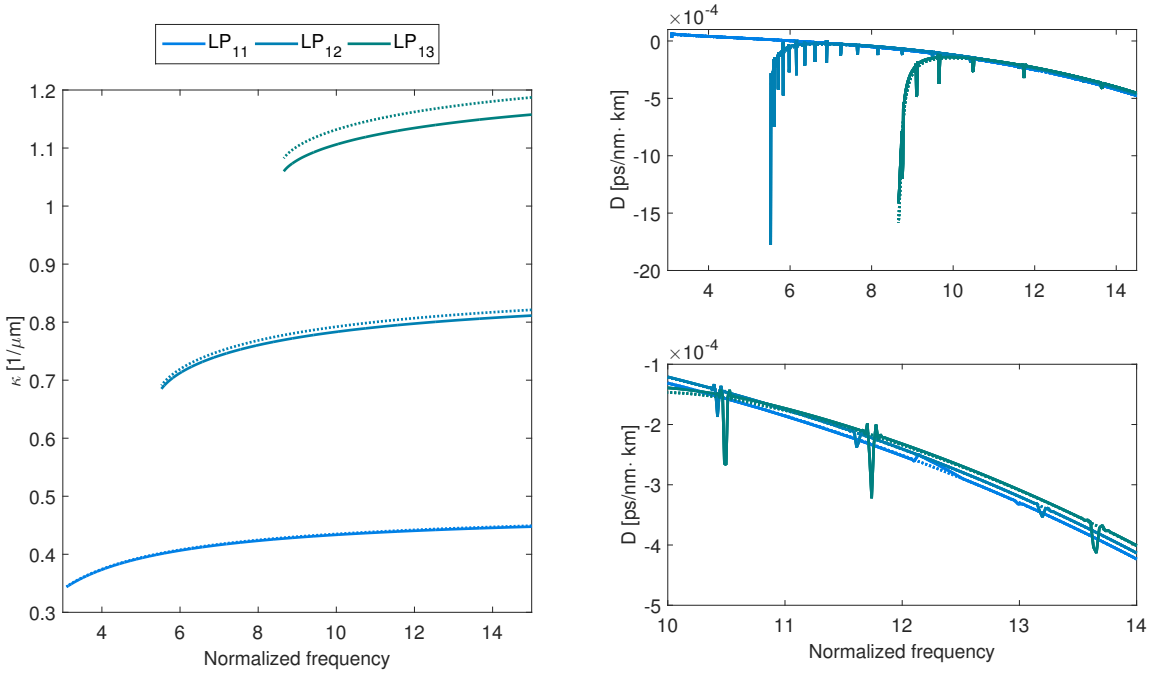

(a) (b)

Figure 6.15: (a) κ found using the Taylor approximation method on the radial mode field profile plotted for all guided modes in the LP_{1X} mode group. (b) The GVD found using κ is found. The plots are limited to above cutoff. The lower plot shows a zoom in of the GVD plot. For all plots the solid lines correspond to the Taylor approximation method and the dotted lines to the data from the scalar mode solver.

spacing and the spacing in the ZDW. The peaks in the plot that do not follow the curve of the GVD yielded by the scalar mode solver are artifacts of the numerical differentiation performed on the effective refractive index [104].

Lastly, the LP_{2X} mode group is considered. The values for κ retrieved with the Taylor approximation method, which are in good accordance with the simulated κ-values, are plotted in Fig. 6.16b, with a deviation less than 1 %. These values are used to find the GVD.

For all considered mode groups, an error in the calculation of κ less than 10 % is achieved. For the LP_{1X} mode group where the analysis is based directly on the electric field profile, the error is significantly larger than for the LP_{0X} and LP_{2X} mode groups, where the analysis is based on the derivative of the electric field. This is intuitive as the derivative is a more sensitive feature [104].

In the calculation of the GVD, some artifacts caused by the numerical differentiation of the effective refractive index. However, good consistency between the two data sets are observed

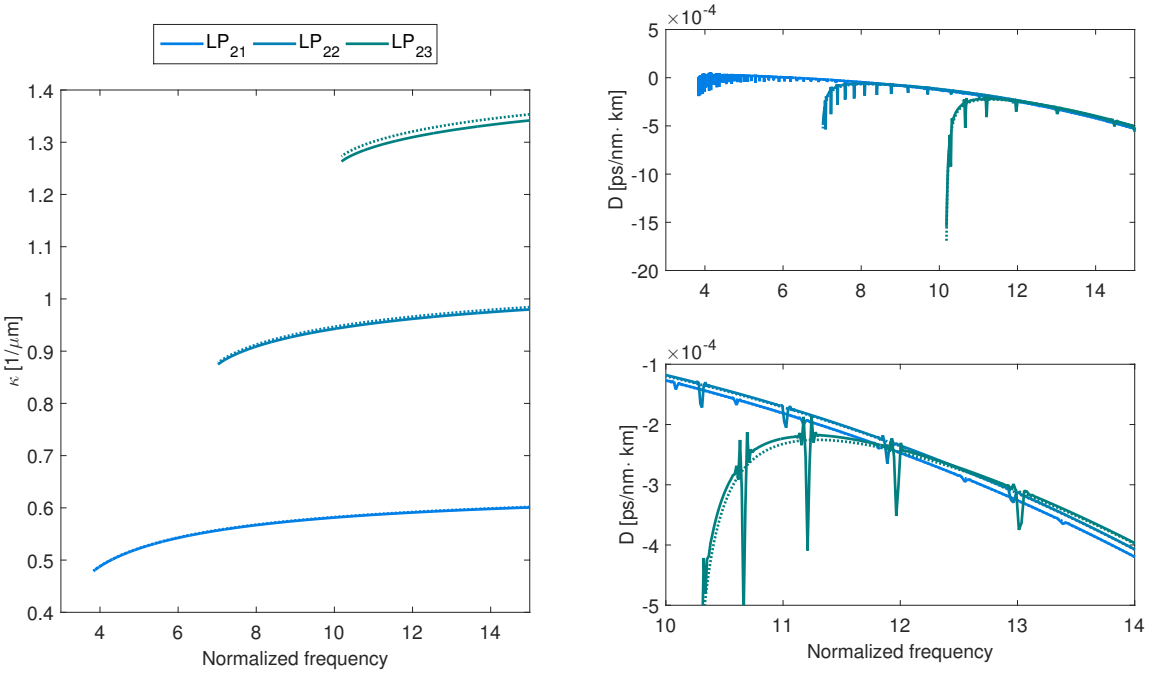

(a) (b)

Figure 6.16: (a) κ found using the Taylor approximation method on the differentiated radial mode field profile plotted for all guided modes in the LP_{2X} mode group. (b) The GVD found using κ is found. The lower plot shows a zoom in of the GVD plot. For all plots the solid lines correspond to the Taylor approximation method and the dotted lines to the data from the scalar mode solver.

showing this method's use in the design process for setups making use of the GVD tailorability of HOMs [33, 39, 63, 102, 104].

For all considered mode groups, the method provides an easy way to find GVD based solely on the radial field profile away from cutoff. As the method only rely on the data in the center of the mode, the method does not depend on the phase of the radial field profile even though that may also be determined easily by a phase retrieval process as presented in Sec. 6.2 [67, 68, 104]. Several fiber types may be considered in a step index fiber approximation [107] and despite the crude approximation, the results show that the method provides significant insight.

A limitation to the method, given that it is to be implemented experimentally, is the ability to excite the HOMs purely [104]. However recently, it has been demonstrated that HOMs may be excited very easily and with good mode discrimination using SLMs [46].

6.3.2 Experimental results

In this section, preliminary experimental results are presented. A series of near field images of the fundamental mode of 780HP from Thorlabs [100]. A narrowband tunable source is coupled

into the fiber, and the near field images are recorded in the spectrum from 727 to 970 nm. Secondly, a line through the center is extracted. The data is filtered for noise and numerically differentiated. The radius axis is scaled to the mode field diameter of the fundamental mode at 850 nm, which is given in the specifications for the fiber [100]. A plot of the raw data at 727 nm, and the noise filtered data is plotted in Fig. 6.17 along the left y-axis. The noise filtering is based on a smoothing mechanism which finds a moving average. Along the right y-axis, the numerical differential of the normalized field strength is plotted. This differential is based on the smoothed data set. The differential of the normalized field strength close to zero is fitted with a linear function through origin to find κ.

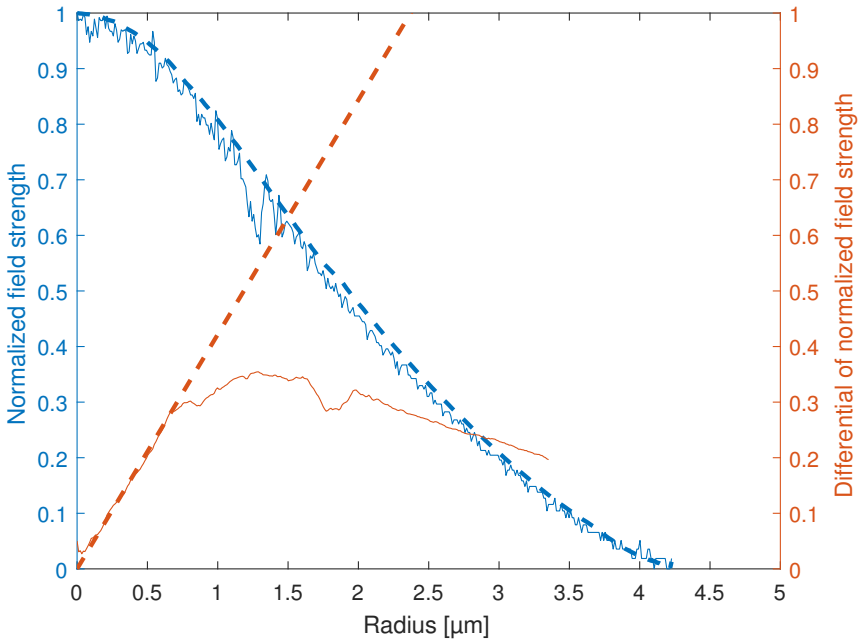

Figure 6.17: Normalized field strength as function of the radius plotted along the left y-axis. Both the raw data and the smoothed data - smoothed with moving average routine - are plotted. At the right y-axis, the differential of the smoothed normalized electric field strength is plotted as function of the radius, a linear fit through the origin based on the center data, is plotted as well. The slope of this function is used to find κ.

In Fig. 6.18, the derived value of κ is plotted as function of the wavelength. An average of the data set is plotted as well along with the data for κ based on the solution from a scalar mode solver. Large fluctuations in κ is observed, but the trend shows the same as the data from the scalar mode solver. However the precision in the data is however to poor for a calculation of the GVD.

The large fluctuations observed in κ is mainly due to the noise in the measurement. Both in terms of finding the correct shape of the measured mode as well as finding the center. When using a Taylor approximation around the origin, the correct position of the origin is of very high

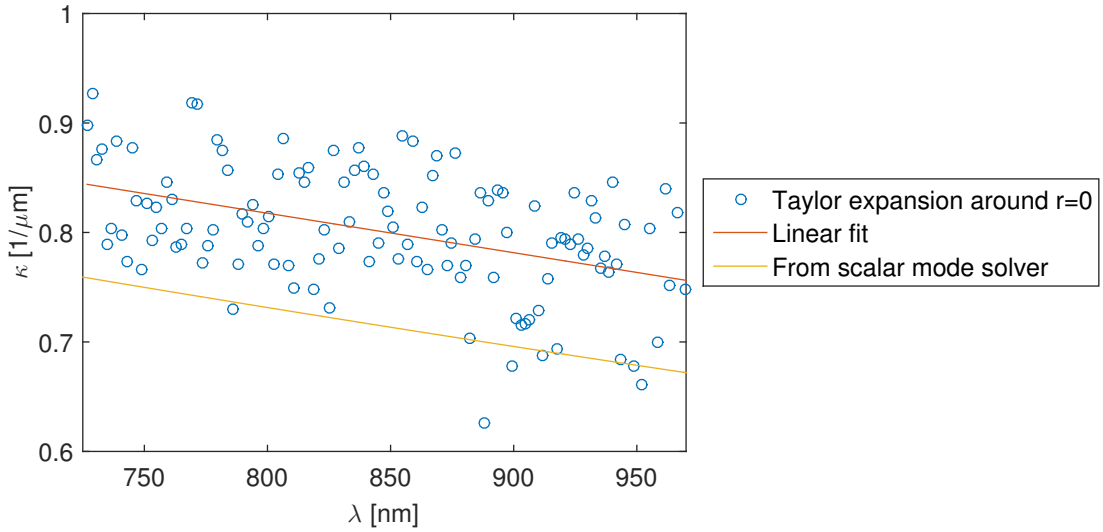

Figure 6.18: κ found using the Taylor approximation method on the differentiated radial mode field profile plotted for the LP_{01}-mode measured in a HP780-fiber. Also plotted is the value of κ found using a scalar mode solver.

importance.

Summing up, it has been showed that the measurement is able to produce the trend in κ.

6.4 Summary

In summary, it has been shown that the divergence angle, which is an easily measurable quantity, may be used as a quality factor for HOMs in fibers.

In the second subsection, phase retrieval of mixed optical fiber modes has been reviewed. Initially, the method is demonstrated with a numerical example. Secondly, the phase of two experimentally measured mode mixes is retrieved.

Lastly, a new method for determining the GVD is presented. The GVD is found based on field analysis of a near field measurement. Very precise numerical determination of the GVD is presented. Preliminary experimental results are also presented. The experimental results however lack precision due to noise and may not be used to determine the GVD.

CHAPTER 7

CONCLUSION

This chapter sums up the research described in this thesis and provides an outlook for new investigations. The work presented in this thesis generally concerns HOMs in optical fibers including their excitation and characterization. The work falls in three parts.

The first part considers the break of the azimuthal symmetry of Bessel-like modes which occurs when increasing the mode order and/or the refractive index difference, this effect is named the bowtie effect after the characteristic shape of the mode. The first time demonstration of the bowtie effect is reported. The effect is demonstrated in an aircladding double cladding structure, later demonstrations also reports the effect in solid perfectly symmetric fibers. In the aircladding fiber, the bowtie effect sets in for modes larger than LP_{011}, this is shown using full vectorial mode solver. The break of the azimuthal symmetry does not significantly inhibit the properties usually associated with Bessel-like fiber modes such a long diffraction free length and selfhealing. The bowtie modes are shown to have a quasi-radial polarization as opposed to the linear polarization of the LP_{0X} modes. Considering the full vectorial solutions to a perfectly symmetric optical fiber, it is seen that increasing the refractive index difference responsible for the guiding or the mode order, the modes assumes a bowtie-like shape. These investigations are expected to be followed up by a more thorough analysis of the mechanisms in the full vectorial method which includes coupling to EH_{1X} modes which have been documented to assume a quasi-azimuthal polarization in the bowtie limit.

In the second part of the thesis, a new scheme for constructing chirped microbend LPGs is presented. The method uses a versatile platform for tailoring the chirp to the phase matching profile of the targeted HOM conversion in the FUT. This implementation allows for the use of a nonlinear chirp. This is the first time demonstration of microbend LPGs with a nonlinear

chirp. The results are modelled using coupled mode theory and it is shown that the conversion bandwidth may be increased more than four fold. In the experimental implementation, coupling from LP_{01} to LP_{11} in a fewmoded fiber using second order diffraction is demonstrated. The conversion bandwidth is more than doubled. The implementation is limited by the use of second order diffraction. In future implementations it is expected that the increase in the conversion bandwidth may be significantly improved using first order diffraction.

In the final part of the thesis, imaging as a characterization tool for HOMs is considered. Three different characterization methods are considered. First, the divergence angle is introduced as a quality parameter to replace the conventional M^2 which compares the diffraction to that of a Gaussian and suffers from ambiguity when considering mode mixtures, and it is established that several HOMs diverge comparable to the fundamental mode. Secondly, the phase retrieval method is used to retrieve the phase profile of a mode mixture in fewmoded fiber based on volume intensity measurement. A mixture of LP_{01} and LP_{11} is considered both using a numerical example to establish the workings of the method and experimental investigations. In the experimental investigation, both a 50/50 and 88/12 mixture is considered, and in both cases the method shows reliable results. Future investigations may consider the use of the volume intensity measurement for mode decomposition without the need for *a priori* information of the fiber composition. Last, a new method for determining independent of the fiber length the group velocity dispersion of modes in the LP_{0X}, LP_{1X}, and LP_{2X} mode groups based on an analysis of the field profile is presented. The method reproduces the group velocity dispersion spectra obtained analyzing a test fiber with a scalar mode solver. Preliminary experimental results are also presented. With further noise reductions, it is expected that the GVD can be found using this method.

APPENDIX A

Here follows the manuscript for the paper "Broadband Higher Order Mode Conversion using Chirped Microbend Long Period Gratings" submitted for Optics Express.

Broadband Higher Order Mode Conversion using Chirped Microbend Long Period Gratings

STINE MØLLER ISRAELSEN,[1], AND KARSTEN ROTTWITT[1,*]

[1] *DTU Fotonik, Ørsteds Plads byg. 343, 2800 Kgs. Lyngby, Denmark*
[*] *karo@fotonik.dtu.dk*

Abstract: We suggest a new scheme to create chirped microbend long period gratings. Employing this scheme, the bandwidth of mode conversion between LP_{01} to LP_{11} is increased 4.8-fold with a conversion efficiency of 20 dB. This scheme includes a first time demonstration of a nonlinearly chirped long period grating. The scheme is investigated both numerically using coupled mode equations as well as experimentally.

OCIS codes: (050.1590) Chirping, (060.2310) Fiber Optics, (060.2340) Fiber Optics Components.

References and links

1. C. D. Poole, J. M. Wiesenfeld, D. J. Digiovanni, and A. M. Vengsarkar, "Optical fiber-based dispersion compensation using higher order modes near cutoff," Lightwave Technology, Journal of **12**, 1746–1758 (1994).
2. S. Ramachandran, Z. Wang, and M. Yan, "Bandwidth control of long-period grating-based mode converters in few-mode fibers," Optics letters **27**, 698–700 (2002).
3. S. H. M. Larsen, M. E. V. Pedersen, L. Grüner-Nielsen, M. Yan, E. Monberg, P. Wisk, and K. Rottwitt, "Polarization-maintaining higher-order mode fiber module with anomalous dispersion at 1 μm," Optics letters **37**, 4170–4172 (2012).
4. L. Zhu, A. Verhoef, K. Jespersen, V. Kalashnikov, L. Grüner-Nielsen, D. Lorenc, A. Baltuška, and A. Fernández, "Generation of high fidelity 62-fs, 7-nj pulses at 1035 nm from a net normal-dispersion yb-fiber laser with anomalous dispersion higher-order-mode fiber," Optics express **21**, 16255–16262 (2013).
5. A. Verhoef, L. Zhu, S. M. Israelsen, L. Grüner-Nielsen, A. Unterhuber, W. Kautek, K. Rottwitt, A. Baltuška, and A. Fernández, "Sub-100 fs pulses from an all-polarization maintaining yb-fiber oscillator with an anomalous dispersion higher-order-mode fiber," Optics express **23**, 26139–26145 (2015).
6. S. Ramachandran, "Dispersion-tailored few-mode fibers: a versatile platform for in-fiber photonic devices," Lightwave Technology, Journal of **23**, 3426–3443 (2005).
7. V. Grubsky and J. Feinberg, "Long-period fiber gratings with variable coupling for real-time sensing applications," Opt. Lett. **25**, 203–205 (2000).
8. C. Poole, H. Presby, and J. Meester, "Two-mode fibre spatial-mode converter using periodic core deformation," Electronics letters **30**, 1437–1438 (1994).
9. P. Steinvurzel, K. Tantiwanichapan, M. Goto, and S. Ramachandran, "Fiber-based bessel beams with controllable diffraction-resistant distance," Opt. Lett. **36**, 4671–4673 (2011).
10. Y. Kondo, K. Nouchi, T. Mitsuyu, M. Watanabe, P. G. Kazansky, and K. Hirao, "Fabrication of long-period fiber gratings by focused irradiation of infrared femtosecond laser pulses," Optics letters **24**, 646–648 (1999).
11. D. B. Stegall and T. Erdogan, "Dispersion control with use of long-period fiber gratings," J. Opt. Soc. Am. A **17**, 304–312 (2000).
12. T. He, L. Rishoj, J. Demas, and S. Ramachandran, "Dispersion compensation using chirped long period gratings," CLEO: Science and Innovations pp. STu3P–7 (2016).
13. D. Östling and H. E. Engan, "Broadband spatial mode conversion by chirped fiber bending," Optics letters **21**, 192–194 (1996).
14. S. Ramachandran, J. Wagener, R. Espindola, and T. A. Strasser, "Effects of chirp in long period gratings," Bragg Gratings, Photosensitivity, and Poling in Glass Waveguides p. BE1 (1999).
15. L. Grüner-Nielsen and J. W. Nicholson, "Stable mode converter for conversion between lp01 and lp11 using a thermally induced long period grating," Proceedings of IEEE Summer Topical Meeting pp. 214–215 (2012).
16. R. C. Youngquist, J. L. Brooks, and H. J. Shaw, "Two-mode fiber modal coupler," Opt. Lett. **9**, 177–179 (1984).
17. R. Kashyap, *Fiber bragg gratings* (Academic press, 1999).
18. X. Shu, L. Zhang, and I. Bennion, "Fabrication and characterisation of ultra-long-period fibre gratings," Optics communications **203**, 277–281 (2002).
19. A. M. Vengsarkar, P. J. Lemaire, J. B. Judkins, V. Bhatia, T. Erdogan, and J. E. Sipe, "Long-period fiber gratings as band-rejection filters," Lightwave Technology, Journal of **14**, 58–65 (1996).

Broadband mode conversion have several applications e.g. within group velocity dispersion

(GVD) compensation [1–3] which may be used in ultrashort pulsed lasers [4,5], but also within sensing [6]. The ability to achieve a broader and tailorable conversion bandwidth is thus highly desirable. This is possible either by engineering the fiber and using the point where the group delay difference between the two modes in the conversion process is zero [1–3, 7] or as we demonstrate in this work using a chirped long period (LPG). LPGs have been demonstrated in many forms including microbend [1], CO_2-formed [8], UV-induced [2, 9] and formed using high intensity light [10]. Chirped LPGs are more versatile in the way that we only need to design the chirp of the LPG to achieve broadband conversion and the method is thus in principle applicable to all fibers. It has also been showed that chirped LPGs have a GVD compensating effect by them selves. This has been demonstrated both theoretically [11] and recently also experimentally [12]. However, in this work, we focus on broadband mode conversion. Chirped fiber LPGs for broadband mode conversion was first suggested by Östling *et al.* [13]. The scheme presented in this work elaborates the idea presented by Östling and shows a straight forward way to implement linear and nonlinear chirp in a microbend LPG. Note that employing a microbend LPG limits the mode conversion to conversion between symmetric and anti-symmetric modes [1]. Chirping have also been demonstrated for UV-induced LPGs [12, 14] which allows for coupling to symmetric modes.

The principle of implementation of chirped microbend LPGs is outlined in Fig. 1.

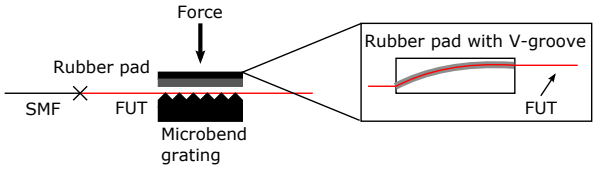

Fig. 1. Principle of the chirped microbend LPG. The fiber under test (FUT) is perturbed by a microbend LPG. The chirp in the LPG is made by a curved groove in the rubberpad used to press the fiber onto microbend LPG.

We employ microbend LPGs as higher order mode converters. However, instead of holding the fiber under test (FUT) straight as is customary [15], the FUT is curved upon the microbend LPG. The curve is achieved by placing the FUT in a groove in the rubber pad pressing the FUT onto the microbend LPG. The groove feature enables a simple and versatile tool for tailoring the chirp of the LPG; the shape of the groove simply defines the chirp.

Initially, the mode conversion is considered numerically. Östling *et al.* limit their investigation to linearly chirped microbend LPGs [13]. Here we also consider nonlinearly chirped LPGs. This is to our knowledge the first demonstration of nonlinearly chirped LPGs.

We use coupled mode theory to simulate the conversion efficiency of the chirped microbend LPG [13]. If a_{01} and a_{11} are the complex modal amplitudes of LP_{01} and LP_{11}, respectively, and κ is the coupling coefficient, then

$$\frac{\mathrm{d}a_{01}}{\mathrm{d}z} = -i\kappa a_{11} \exp\left(i \int_0^z \Delta\beta(\lambda, x)\mathrm{d}x\right) \quad (1)$$

$$\frac{\mathrm{d}a_{11}}{\mathrm{d}z} = -i\kappa^* a_{01} \exp\left(-i \int_0^z \Delta\beta(\lambda, x)\mathrm{d}x\right), \quad (2)$$

where

$$\Delta\beta(\lambda, z) = 2\pi[1/L_B(\lambda) - 1/\Lambda(z)], \quad (3)$$

where $L_B(\lambda)$ is the measurable beat length between the two modes and $\Lambda(z)$ is the pitch of the LPG [16]. The pitch of the LPG in the fiber may be described as $\Lambda(z) = \Lambda_0 + \delta(z)$, where Λ is the unperturbed pitch of the LPG while the perturbation, $\delta(z)$, describes the linear or nonlinear chirp. κ is the coupling coefficient proportional to the force applied to the rubber pad; κ is assumed constant along z. Changing κ along z would beneficial in the design of LPG spectra for example when reducing the number of sidebands for GVD compensation [12]. However, this is difficult to implement in this scheme as it requires very high precision in the design of the rubber pad thickness as well as knowledge of the material properties of the used rubber. The coupled mode equations are solved numerically employing an ODE solver, as Eq. (2) does not yield a physically intuitive closed form solution [14].

To achieve the widest conversion bandwidth, we employ a nonlinearly chirped LPG with pitch in form of a 2nd order polynomial. To find the set of coupled differential equations to implement in the ODE solver, the integral

$$\begin{aligned} \int_0^z \Delta\beta(\lambda, x)\mathrm{dx} &= \int_0^z 2\pi \left(\frac{1}{L_B(\lambda)} - \frac{1}{\Lambda(x)} \right) \mathrm{dx} \\ &= \int_0^z 2\pi \left(\frac{1}{L_B(\lambda)} - \frac{1}{ax^2 + bx + c} \right) \mathrm{dx} \end{aligned} \tag{4}$$

is solved.

We consider a TrueWave® fiber operated at 800 nm, where it is fewmoded and guides LP_{01} and LP_{11}. We want to couple from LP_{01} to LP_{11}. We employ a higher order diffraction LPG to achieve phase matching [17]. The first order diffraction is not achievable due to a mechanical constraint: For pitches comparable to the fiber diameter (that is including the coating), the mechanical grating is not able to bend and perturb the fiber.
To find the fitting parameters of the chirp, the beat length within the desired wavelength range is approximated with a second order polynomial using the longitudinal axis of the LPG as the independent variable of the fit. The second order polynomial is used in accordance with (4). The aim is to achieve broadband conversion without overcoupling around 800 nm and the optimization of the chirp parameters is limited to the lower wavelength limit of the beat length measurement and the turn-around-point around 870 nm [7].

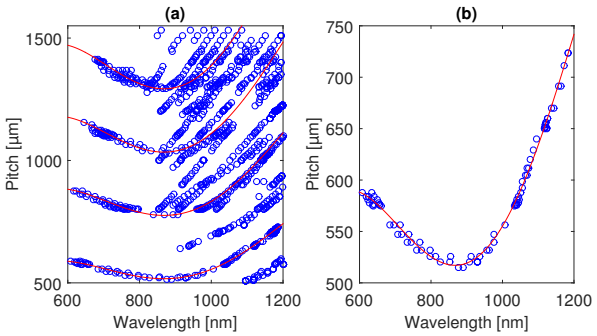

Fig. 2. Phase matching curves for the conversion of LP_{01} to LP_{11} in a TrueWave® fiber operated in a fewmoded regime. (a) Full measurement of phase matching curves for higher order conversions corresponding to $\Lambda = 2L_B$, $\Lambda = 3L_B$, $\Lambda = 4L_B$, and $\Lambda = 5L_B$. The red lines in the plot correspond to 4th order polynomial fit in (b) scaled to the order of conversion. (b) Selected data for the pitch corresponding to $\Lambda = 2L_B$. The data is fitted to 4th order polynomial.

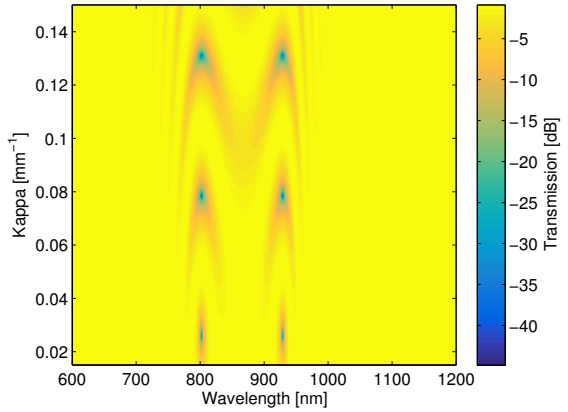

Fig. 3. Transmission data for the conversion of LP_{01} to LP_{11} in a TrueWave® fiber operated in a fewmoded regime. The applied mode converter is an unchirped LPG with a pitch of 525 μm which corresponds to conversion at 800 nm.

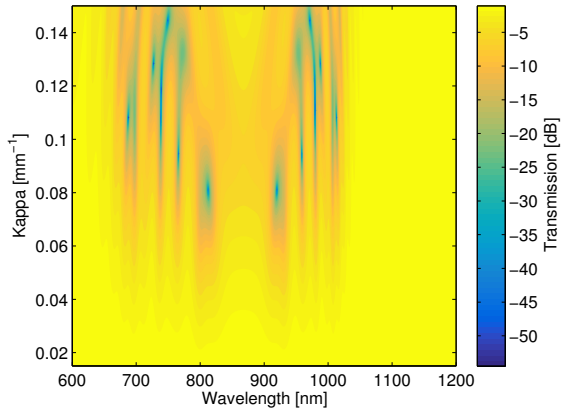

Fig. 4. Transmission data for the conversion of LP_{01} to LP_{11} in a TrueWave® fiber operated in a fewmoded regime. The applied mode converter is a nonlinearly chirped LPG where the chirp is optimized for conversion around 800 nm.

In Fig. 2(a), the full measurement of the beat length is plotted. The multiple curves are a result of the higher order diffraction and their sidebands. The higher order diffraction curves are marked with a red a red line corresponding to the fit in Fig. 2(b) scaled to the diffraction order. The remaining points are sidebands. Sidebands have previously been observed using higher order diffraction [18]. The first order diffraction is not achievable as previously explained. The phase matching measurement corresponding to second order diffraction is plotted in Fig. 2(b), the order of the diffraction is identified from the full phase matching measurement in Fig. 2(a). The phase matching measurement is fitted to a fourth order polynomial. In Fig. 3 the transmission, that is the remaining power in the fundamental mode after the LPG, is plotted as function of the wavelength and conversion efficiency for an unchirped LPG with a $\Lambda = 525$ μm which corresponds to conversion at 800 nm employing second order diffraction. -20 dB transmission is achieved with a 1.8 nm bandwidth without overcoupling, that corresponds to the lowest conversion efficiency κ

that allows for -20 dB transmission. The transmission of a nonlinearly chirped LPG optimized for broadband conversion around 800 nm is plotted in Fig. 4 as a function of the wavelength and the conversion efficiency. With a -20 dB transmission across a 8.6 nm bandwidth, a 4.8-fold increase of the bandwidth is achieved. As for the unchirped LPG, the transmission is found using coupled mode theory as described in (2) with the condition of (4). Note that the conversion to LP_{11} is achieved for higher values of the coupling coefficient, κ, corresponding to a larger force upon the rubber pad, hence there is a trade off between conversion bandwidth and possible permanent mechanical deformation of the fiber due to the larger load.

For closer examination, the transmission of the microbend LPGs in the chirped and unchirped configuration is plotted in Fig. 5 applying the conversion coefficient κ yielding the largest dip in transmission without overcoupling. In this figure, it is evident that the chirped LPG has a significantly broader bandwidth, if we consider the 3 dB bandwidth there is an 23-fold increment. However with conversion efficiencies of 0.026 mm^{-1} and 0.081 mm^{-1} for the unchirped and chirped configuration, respectively, the risk of permanent deformation of the fiber is much larger for the chirped LPG.

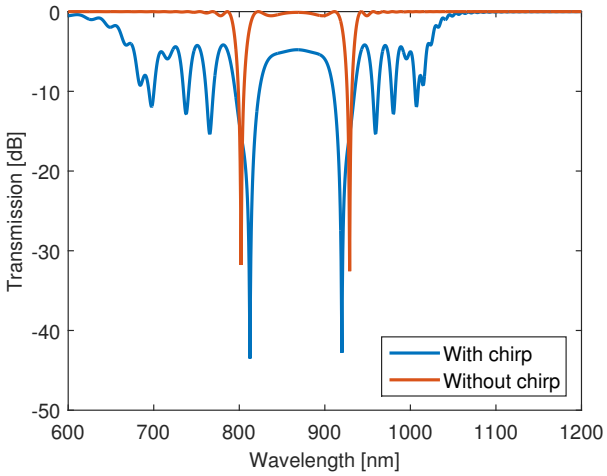

Fig. 5. Numerically determined transmission plot of the chirped and the unchiped LPG. For the chirped LPG, a conversion efficiency of 0.08115 mm^{-1} is applied and for the unchirped LPG, a conversion efficiency of 0.0258 mm^{-1}.

For the experimental investigations, the shape of the V-groove must be designed according desired nonlinear chirp. Thus the parametric curve describing the chirp, $\mathbf{r}(u)$ is written as

$$\oint_L = \int_0^z |\mathbf{r}'(u)| \mathrm{d}u = \Lambda(z) \tag{5}$$

Thus the line integral along the V-groove is equal to the pitch as function of z. This is however not easily solved. Instead, we approximate with a piecewise linear function, the pieces correspond to each step as the rubberpad is pressed on to the alumina block creating the microbends. To carve a smooth curve in the rubberpad, the piecewise linear function is approximated with a third order polynomia.

In this section, a physical realization of the setup in Fig. 1 is considered. We consider the results of an experimental realization of the nonlinearly chirped LPG. The chirp is tailored to the phase matching curve as for the numerical calculation in Fig. 4. The transmission is measured by

launching a broadband source in to the fundamental mode of the FUT as illustrated in Fig. 1 and after the chirped microbend LPG the FUT is spliced to a single mode fiber (@ 800 nm). This is a standard method for characterizing the conversion of LPG to the higher order mode [19]. Secondly, the transmission plot shows very little multipath interference indicating excitation of a single mode by the LPG, which verifies the assumption of no other losses in the transmission measurement. The transmission is measured as function of the translation of the stage controlling the position of the rubber pad. Note, that the force on the rubber pad increase with a descreasing value of the translation. In principle, the translation of the rubber pad is linearly proportional to the force on the rubber pad and thereby the conversion efficiency, κ, but due to mechanical restraints of the setup and the mechanical properties of the rubber pad, the relation between translation and force is not complete linear.

Initially, we measure a reference given by a nonchirped microbend LPG tailored for conversion at 800 nm corresponding to pitch of 525nm. The transmission mapping as function of the translation of the rubber pad is plotted in Fig. 6.

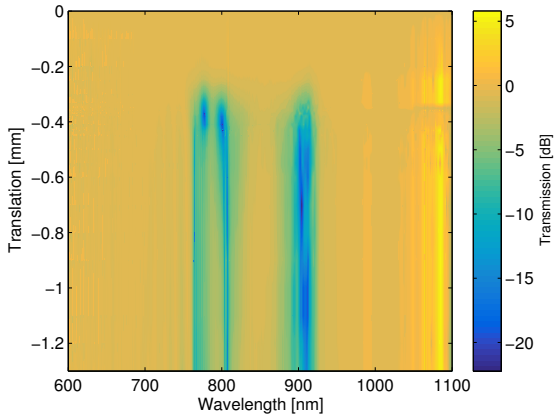

Fig. 6. Experimental transmission data for the conversion of LP_{01} to LP_{11} in a TrueWave® fiber operated in a fewmoded regime. The conversion efficiency is given by the translation of the rubber pad given by the translation of the stage controlling the position of the rubber band. The applied mode converter is an unchirped LPG with a pitch of 525 μm which corresponds to conversion at 800 nm.

Transmission as function of the wavelength and the translation of the stage, i.e. the conversion efficiency, κ, for the nonlinearly chirped LPG applying second order diffraction tailored for conversion at 800 nm using the measured phase matching curves plotted in Fig. 2 is plotted in Fig. 7. In both the transmission wavelength spectra of the chirped and the unchirped LPG, there are some features around 1050 nm independently of the translation, which is a result of unstable excitation source and not the microbend LPGs.

In the experimental transmission spectra of the nonlinearly chirped LPG, we observe many of the same features as we see in the numerical results. Unfortunately, we are not able to map some of the high conversion efficiency effects. That is a result of the use of second order diffraction in the LPG demanding higher conversion efficiencies than first order diffraction and the mechanical constraint of a microbend LPG limiting the conversion to HOMs to what is possible without permanently damaging or potentially breaking the fiber. The linearity between the plotted load and the conversion efficiency is also limited by the relaxation of the microbend LPG as described by G.-Nielsen *et al.* [15]. However, as we employ a rubber pad the relaxation is reduced.

In Fig. 8, the best possible conversion for the chirped and the unchirped LPG in the TrueWave

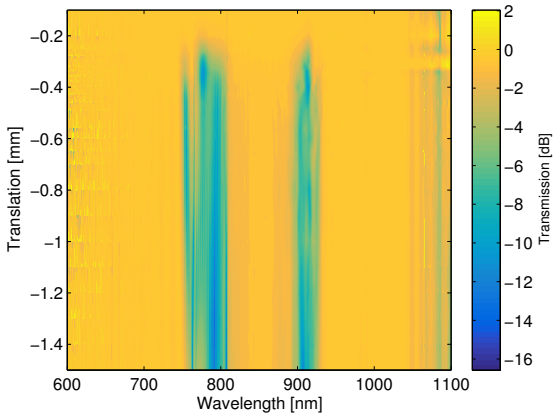

Fig. 7. Experimental transmission data for the conversion from LP_{01} to LP_{11} in a TrueWave® fiber operated in a fewmoded regime. The conversion efficiency is given by the translation of the rubber pad given in the translation of the stage controlling the position of the rubber band. The applied mode converter is a nonlinearly chirped LPG where the chirp is optimized for conversion around 800 nm.

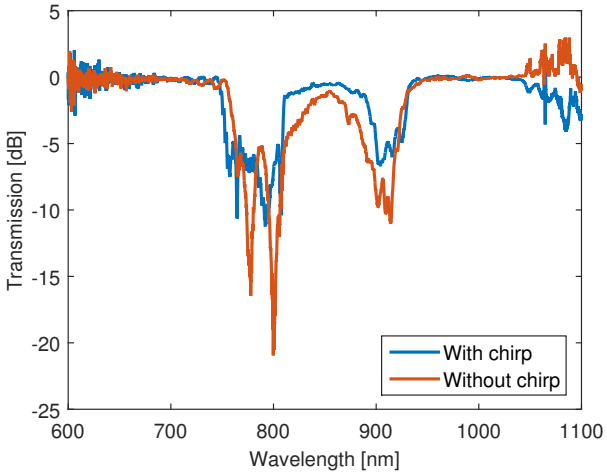

Fig. 8. Measured transmission plot of the chirped and the unchiped LPG in the TW fiber. For the chirped LPG, a translation of -0.41 mm is used and for the unchirped LPG, a load of -1 mm is used.

fiber is plotted. In both the numerical and experimental studies, the chirped LPG requires a higher coupling efficiency, κ, - given by the translation of the rubber pad - for optimum coupling. There are several features to notice in this plot: The first is that the transmission plot for the unchirped LPG does not only show one dip as the simulations. We expect that this is a result of the second order diffraction used. The second is the squareness of the transmission spectrum for the chirped LPG, a feature which has been achieved without overcoupling and unwanted spectral oscillatory behavior [14]. This feature is very attractive for GVD compensation using chirped LPGs [11, 12]. There is no significant broadening in the chirped LPG if we consider both dips in the transmission spectrum close to 800 nm for the unchirped LPG. However, we recall that the chirp was designed

only for the dip at 800 nm. Using this fact, the conversion bandwidth is enhanced 2.7-fold at 5 dB conversion. Due to mechanical constraints of this system, it is unfortunately not possible to achieve higher conversion efficiencies for this system, which would most likely have resulted in larger conversion. There is increased need for the high conversion efficiencies in this system due to the use of higher order diffraction.

In summary, we have demonstrated a new and versatile platform for chirped LPGs coupling from a symmetrical to an anti-symmetrical mode and vice versa. The transmission characteristics of this scheme has been modelled using coupled mode theory and a 4.8-fold increase of the bandwidth is achieved for conversion from LP_{01} to LP_{11} in a TrueWave® fiber operated in a fewmoded regime.

APPENDIX B

APPENDIX B

Here follows the manuscript for the paper "Determining the Group Velocity Dispersion by Field Analysis for the LP_{0X}, LP_{1X}, and LP_{2X} Mode Groups Independently of the Fiber Length" submitted for JOSA B.

Letter Journal of the Optical Society of America B 1

Determining the Group Velocity Dispersion by Field Analysis for the LP_{0X}, LP_{1X}, and LP_{2X} Mode Groups Independently of the Fiber Length

STINE MØLLER ISRAELSEN[1], MARIO A. USUGA CASTANEDA[1], AND KARSTEN ROTTWITT[1,*]

[1] DTU Fotonik, Ørsteds Plads byg. 343, 2800 Kgs. Lyngby, Denmark
[*] Corresponding author: karo@fotonik.dtu.dk

Compiled August 18, 2016

By knowing the electric field distribution of a guided mode in an optical fiber, we are able to evaluate the group velocity dispersion in a weakly guiding step index fiber for a pure mode in the LP_{0X}, LP_{1X}, and LP_{2X} mode groups independently of the fiber length. We demonstrate the method numerically for all three mode groups.

OCIS codes: (060.2310) Fiber Optics, (060.2400) Fiber properties, (060.2270) Fiber characterization.

http://dx.doi.org/10.1364/ao.XX.XXXXXX

Determining the group velocity dispersion (GVD) in optical fibers has been an important discipline for instance for the design of optical resonators and amplifiers [1, 2] and for designing setups for parametric processes including research on four wave mixing enabled by higher order modes (HOMs) [3]. There are a number of standard techniques for measuring the GVD which include time-of-flight measurements, phase shift measurements and interferometric techniques [1]. However, both time-of-flight and phase-shift measurements require relatively long fiber lengths [1]. Stable propagation of HOMs in long lengths of fiber is difficult due to mode mixing and determination of the GVD using the standard methods is thus not straight forward. A few demonstrations of GVD measurements of very stably propagating HOMs using long fiber lengths have been demonstrated - however, only in few moded fibers [4, 5]. Newer interferometric techniques include S^2 and C^2, though primarily developed for determining the modal content, these methods also yield the GVD of all modes in the decomposition [6–8]. These methods require fiber lengths in the order of meters and both have relatively complicated setups as is customary for interferometric techniques. A simpler interferometric technique for measuring the GVD of a HOM was presented by Menashe *et al.*; in this technique the fundamental mode and a selected HOM are exicted simultaneously and the modal beating is used to extract the GVD [9]. However, this method requires knowledge of the GVD of the fundamental mode.

In this paper, we determine the GVD of weakly guiding step index fiber by determining the intensity profile of a pure mode in the near field as function of the wavelength. This method is an extension of the mode field diameter method [10, 11]. The mode-field-diameter method considers only a single mode fiber and assumes that the field can be described by a Gaussian [10, 11]. In this work no such assumption is made in stead the complete intensity profile is used which allows us to consider a variety of modes.

As the determination of the GVD relies only on the intensity profile, our method thus works independently of the fiber length. The only thing needed is the intensity distribution of a purely guided mode. As a consequence, it is possible to use this method on very short fiber lengths as opposed to the other methods mentioned. We thus present the first very simple method for determining the GVD of a HOM without the need for propagation of the mode which may result in mode coupling. The method enables us to determine the GVD of HOMs in fibers where the HOM have poor propagation properties. Depending on the source used to excite the relevant mode, the method is potentially very broadband.

We exploit that the solution to the wave equation governing the field of a weakly guiding step index fiber in the core (and cladding) of the fiber is well known [12]. It is noted that despite the fact that our method of determining the GVD of HOMs is based on using a weakly guiding step index fiber, this is an approximation that provide significant insight and is often used for more complex fiber types [12, 13]. We assume that for a weakly guiding fiber, the modulus of the field is proportional to the square root of the intensity. For weakly guiding fibers the radial field distribution in the core is described by the Bessel function $J_x(\kappa r)$, with x describing the aximuthal mode order, where the parameter κ is given by:

$$\kappa^2 = k_0^2(n_c^2 - n_{eff}^2), \tag{1}$$

and k_0 is the wave number, n_c is the refractive index of the core, and n_{eff} is the effective refractive index of the mode. Initially, we assume that $n_c = n_{SiO_2}(\lambda) + \Delta n$, where n_{SiO_2} is the refractive index of silica and δn is the refractive index step between core and cladding. The wavelength dependence of the refractive index of silica, n_{SiO_2}, is given by Sellmeier's formula

[12]. The wavelength dependence of germanium, responsible for Δn, is negligible compared to that of silica [12]. That allows us to express n_{eff} as:

$$n_{eff}(\lambda) = \sqrt{(n_{SiO_2}(\lambda) + \Delta n)^2 - \kappa(\lambda)^2/k_0^2}. \quad (2)$$

The GVD parameter, D, is determined by

$$D = -\frac{\lambda}{c}\frac{\partial^2 n_{eff}}{\partial \lambda^2}. \quad (3)$$

If we find κ as outlined in the following sections, we may numerically determine the GVD. To a rough approximation the wavelength dependence of the square of the refractive index of the fiber core is equal to the wavelength dependence of silica: $n_c^2 \approx n_{SiO_2}^2$, and the expression for n_{eff} simplifies, as does the needed parameters for the fiber under test. In the following section, we outline the procedures to find κ for the LP_{0X}, LP_{1X}, and LP_{2X} modes.

For the LP_{0X} modes the normalized electric field strength is equal to $\Psi(r) = J_0(\kappa r)$. As there is no azimuthal dependence of the electric field, it is not considered for this mode group. The first step is to differentiate the radial dependence of the field: $\Psi'(r) = -\kappa J_1(\kappa r)$.

One approach to find κ could be to evaluate the maximum of the derivative which is κ, but the point of evaluation is for LP_{0X} very close to the core-cladding interface leading to uncertainty of the validity of the solution of the electric field strength. Secondly, this evaluation form would also be strongly dependent on the radial resolution of the field. To have a method valid for all modes in the mode group, we instead perform a Taylor approximation of $\Psi'(r)$ around $r = 0$.

$$\begin{aligned} T_{LP_{0X}}(r) &= -\kappa J_1(0) - \kappa^2 \left(J_0(0) - \left.\frac{J_1(\kappa r')}{r'}\right|_{r'\to 0} \right) r \\ &\to -\frac{1}{2}\kappa^2 r \quad \text{for} \quad r \to 0. \end{aligned} \quad (4)$$

The derivative of the radial field distribution is thus to be approximated with a straight line through origin to find κ.

For the LP_{1X} mode group, we cannot neglect the azimuthal dependence. However, considering the radial dependence for the angle yielding the maximum intensity allows us to omit the azimuthal dependence. The radial dependence of the LP_{1X} mode group may be described as: $\Psi(r) = J_1(\kappa r)$. Performing a Taylor expansion directly on the radial field distribution $r = 0$ to first order gives:

$$\begin{aligned} T_{LP_{1X}}(r) &= \kappa J_1(0) + \kappa \left(J_0(0) - \left.\frac{J_1(\kappa r')}{\kappa r'}\right|_{r'\to 0} \right) r \\ &\to \frac{1}{2}\kappa r \quad \text{for} \quad r \to 0. \end{aligned} \quad (5)$$

This procedure is valid for all modes in the LP_{1X} mode group. The radial field distribution is then approximated with a straight line through the origin that can used to find κ.

As with the LP_{1X} mode group, the azimuthal dependence of the LP_{2X} mode group cannot be neglected. We use the same approach and consider the radial field dependence for the angle yielding the maximum intensity. For the LP_{2X} mode group, it is necessary to differentiate the radial field distribution. The radial field distribution may be described by: $\Psi(r) = J_2(\kappa r)$. The derivative with respect to the radius of the radial field distribution is then $\Psi'(r) = \kappa \left(J_1(\kappa r) + \frac{2J_2(\kappa r)}{\kappa r} \right)$. As for the LP_{0X} mode group, we perform a Taylor approximation on the derivative of the radial field distribution around $r = 0$.

$$\begin{aligned} T_{LP_{2X}}(r) =& \kappa \left(J_1(0) + \left.\frac{2J_2(\kappa r)}{\kappa r}\right|_{r\to 0} \right) \\ &+ \kappa \left[\kappa \left(J_0(0) - \left.\frac{J_1(\kappa r)}{\kappa r}\right|_{r\to 0} \right) + \left.\frac{2J_2(\kappa r)}{\kappa r^2}\right|_{r\to 0} \right. \\ &\left. - \left.\frac{2\left(J_1(\kappa r) - \frac{2J_2(\kappa r)}{\kappa r}\right)}{r}\right|_{r\to 0} \right] r \\ \to& \frac{1}{4}\kappa^2 r \quad \text{for} \quad r \to 0. \end{aligned} \quad (6)$$

The derivative of the radial field distribution is then approximated with a straight line through origin to find κ.

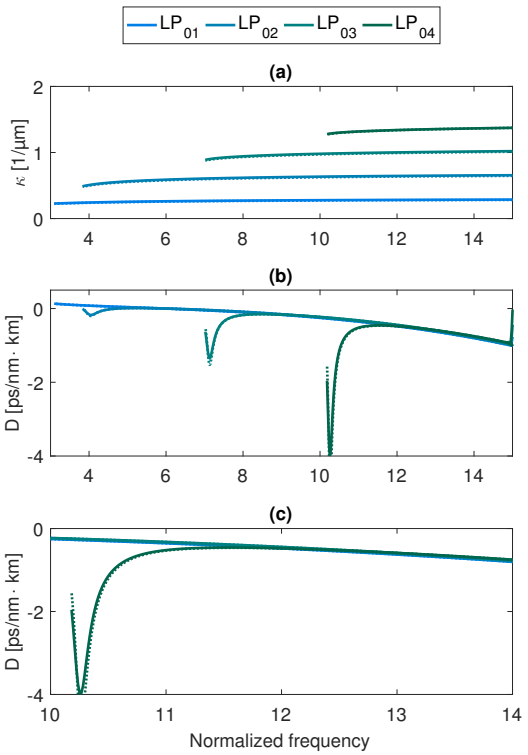

Fig. 1. (a) κ found using the Taylor approximation method on the differentiated radial mode field profile plotted for all guided modes in the LP_{0X} mode group. (b) The GVD found using κ is found. We only plot above cutoff. (c) A zoom in of the GVD plot. For all plots the solid lines correspond to the Taylor approximation method and the dotted lines to the data from the scalar mode solver.

In principle, this form could be expanded to include HOM groups but at the expense of having to expand to higher orders in the Taylor approximation. We limit the investigations to the mode groups where the considered Taylor expansions are

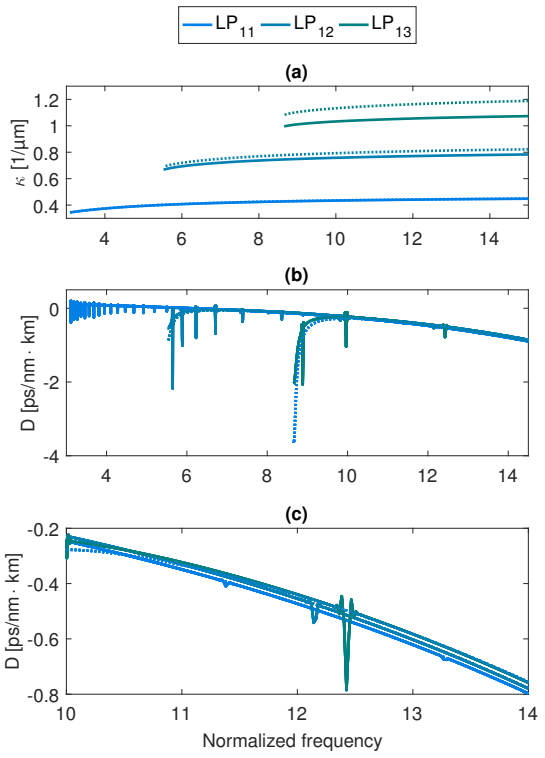

Fig. 2. (a) κ found using the Taylor approximation method on the radial mode field profile plotted for all guided modes in the LP_{1X} mode group. (b) The GVD found using κ is found. We only plot above cutoff. (c) A zoom in of the GVD plot. For all plots the solid lines correspond to the Taylor approximation method and the dotted lines to the data from the scalar mode solver.

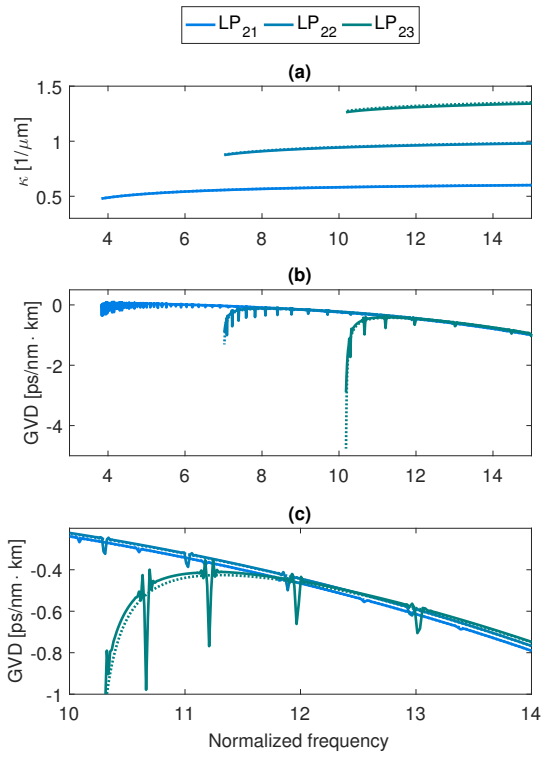

Fig. 3. (a) κ found using the Taylor approximation method on the differentiated radial mode field profile plotted for all guided modes in the LP_{2X} mode group. (b) The GVD found using κ is found. We only plot above cutoff. (c) A zoom in of the GVD plot. For all plots the solid lines correspond to the Taylor approximation method and the dotted lines to the data from the scalar mode solver.

straight lines through origin.

In this section, we consider a numerical example to demonstrate how the method works. The considered case is a multimode step index fiber with a numerical aperture of 0.149 and a core radius of 8 μm. The modes in the fiber are found with a scalar mode solver. The fiber supports all three considered mode groups.

Initially, we consider the LP_{0X} mode group. In Fig. 1a, κ is plotted for all guided LP_{0X} modes in the guided regions as function of the normalized frequency: $V = ka\sqrt{n_c^2 - n_{cl}^2}$. The simulated κ from the scalar mode solver is also plotted as a dotted line. We observe excellent agreement between the simulated values of κ and the κ-values found by the Taylor approximation method. The deviation in κ is less than 1 % for all modes considered.

In Fig. 1b, the GVD found using the Tailor approximation method of the LP_{0X} modes is plotted above cutoff along with the result for the GVD found with the scalar mode solver. Despite the approximation of the squared refractive index of the core, we are able to determine the GVD very accurately. In the zoom in, Fig. 1c, we see that the method is sufficiently accurate for also determining the modal spacing in the GVD and the spacing in the zero dispersion wavelength (ZDW) - both very important parameters in GVD tailoring using HOMs [2, 3].

In Fig. 2a, κ for the LP_{1X} mode group retrieved from the Taylor approximation method is plotted along with κ provided by the scalar mode solver. We observe good accordance between the two data sets, the deviation is less than 10 % for all considered modes. However, the agreement decreases with mode order. That is a result of the resolution of the radial dependence of the electric field strength.

In Fig. 2(b) and 2(c), the GVD of the LP_{1X} mode group based on the data for κ is plotted along with the GVD found with the scalar mode solver. As for the LP_{0X} mode group, we are able to determine the GVD very accurately, this includes important figures such as the intermodal spacing and the spacing in the ZDW. The peaks in the plot that do not follow the curve of the GVD evaluated by the scalar mode solver are artifacts of the numerical differentiation performed on the effective refractive index.

Lastly, we consider the LP_{2X} mode group. The values for κ retrieved with the Taylor approximation method which are in

good accordance with the simulated κ-values are plotted in Fig. 3a, with a deviation less than 1 % between the κ-values determined by the Taylor approximation method and those evaluated by the scalar mode solver. These values of κ are used to find the GVD. In the calculation of the GVD, we observe some artifacts caused by the numerical differentiation of the effective refractive index. We, however, observe good consistency between the two data sets. Consequently, we suggest that this method may be used in the design process for setups making use of the GVD tailorability of HOMs [2–5].

For all considered mode groups, we conclude that the method provides an easy way to find GVD based solely on the radial field profile. The method works well when the considered wavelength is not in the vicinity of cutoff wavelength for the respective mode.

A limitation of the method, given that it is to be implemented experimentally, is the ability to excite the HOMs purely. However recently, it has been demonstrated that HOMs may be excited with very good mode discrimination using spatial light modulators [14].

In conclusion; we have demonstrated the first, to our knowledge, method to determine the GVD of HOMs independently of the fiber length in a weakly guiding step index fiber by analysis of the radial electric field profile. The κ-value used in the evaluation of the GVD is determined with a accuracy of maximum 10 % across all considered mode groups. We speculate that the higher deviation for the LP_{1X} mode group compared to that of the LP_{0X} and LP_{2X} mode groups is a result of the direct analysis on the electric field and not on the derivative of the electric field which is used for LP_{0X} and LP_{2X} mode groups. The method may be applied to three mode groups LP_{0X}, LP_{1X}, and LP_{2X} modes which covers most modes commonly used in step index fibers.

REFERENCES

1. L. G. Cohen, "Comparison of single-mode fiber dispersion measurement techniques," Lightwave Technology, Journal of **3**, 958–966 (1985).
2. A. Verhoef, L. Zhu, S. M. Israelsen, L. Grüner-Nielsen, A. Unterhuber, W. Kautek, K. Rottwitt, A. Baltuška, and A. Fernández, "Sub-100 fs pulses from an all-polarization maintaining yb-fiber oscillator with an anomalous dispersion higher-order-mode fiber," Optics express **23**, 26139–26145 (2015).
3. P. Steinvurzel, J. Demas, B. Tai, Y. Chen, L. Yan, and S. Ramachandran, "Broadband parametric wavelength conversion at 1 μm with large mode area fibers," Opt. Lett. **39**, 743–746 (2014).
4. L. Grüner-Nielsen, S. Ramachandran, K. Jespersen, S. Ghalmi, M. Garmund, and B. Pálsdóttir, "Optimization of higher order mode fibers for dispersion management of femtosecond fiber lasers," Lasers and Applications in Science and Engineering pp. 68730Q–68730Q (2008).
5. S. H. M. Larsen, M. E. V. Pedersen, L. Grüner-Nielsen, M. Yan, E. Monberg, P. Wisk, and K. Rottwitt, "Polarization-maintaining higher-order mode fiber module with anomalous dispersion at 1 μm," Optics letters **37**, 4170–4172 (2012).
6. J. Nicholson, A. Yablon, S. Ramachandran, and S. Ghalmi, "Spatially and spectrally resolved imaging of modal content in large-mode-area fibers," Optics express **16**, 7233–7243 (2008).
7. D. Gray, M. Petrovich, S. R. Sandoghchi, N. Wheeler, N. Baddela, G. Jasion, T. Bradley, D. Richardson, and F. Poletti, "Real-time modal analysis via wavelength-swept spatial and spectral (s< sup> 2</sup>) imaging," (2016).
8. D. Schimpf, R. Barankov, and S. Ramachandran, "Cross-correlated (c 2) imaging of fiber and waveguide modes," Optics express **19**, 13008–13019 (2011).
9. D. Menashe, M. Tur, and Y. Danziger, "Interferometric technique for measuring dispersion of high order modes in optical fibres," Electronics Letters **37**, 1 (2001).
10. P. Sansonetti, "Modal dispersion in single-mode fibres: simple approximation issued from mode spot size spectral behaviour," Electronics Letters **15**, 647–648 (1982).
11. J. Pocholle, J. Raffy, J. Auge, and M. Papuchon, "Determination of modal dispersion in monomode fibres from wavelength dependence of the mode spot size," Electronics letters **19**, 1093–1094 (1983).
12. M. J. Adams, *An introduction to optical waveguides* (UMI Books on Demand, 1981).
13. F. Brechet, J. Marcou, D. Pagnoux, and P. Roy, "Complete analysis of the characteristics of propagation into photonic crystal fibers, by the finite element method," Optical Fiber Technology **6**, 181–191 (2000).
14. J. Demas, L. Rishøj, and S. Ramachandran, "Free-space beam shaping for precise control and conversion of modes in optical fiber," Opt. Express **23**, 28531–28545 (2015).

APPENDIX C

List of Abbreviations

- HOM: Higher order mode
- LPG: Long period grating
- GVD: Group velocity dispersion
- SLM: Spatial light modulator
- TAP: Turn-around-point
- MIMO: Multiple input multiple output
- PM: Polarization maintaining
- SMF: Single mode fiber
- ZDW: Zero dispersion wavelength
- FUT: Fiber under test
- MPI: Multi path interference
- FFT: Fast fourier transformation
- OSA: Optical spectrum analyzer

BIBLIOGRAPHY

[1] M. J. Adams.
An introduction to optical waveguides.
UMI Books on Demand, 1981.

[2] K. Okamoto.
Fundamentals of optical waveguides.
Academic press, 2010.

[3] T. A. Birks, J. C. Knight, and P. St. J. Russell.
Endlessly single-mode photonic crystal fiber.
Optics letters, 22(13):961–963, 1997.

[4] K. Furusawa, A. Malinowski, J. H. V. Price, T. M. Monro, J. K. Sahu, J. Nilsson, and D. J. Richardson.
Cladding pumped ytterbium-doped fiber laser with holey inner and outer cladding.
Optics Express, 9(13):714–720, 2001.

[5] N. Bozinovic, Y. Yue, Y. Ren, M. Tur, P. Kristensen, H. Huang, A. E. Willner, and S. Ramachandran.
Terabit-scale orbital angular momentum mode division multiplexing in fibers.
Science, 340(6140):1545–1548, 2013.

[6] S. Ramachandran, P. Kristensen, and M. F. Yan.
Generation and propagation of radially polarized beams in optical fibers.
Optics letters, 34(16):2525–2527, 2009.

[7] N. Bozinovic, S. Golowich, P. Kristensen, and S. Ramachandran.
Control of orbital angular momentum of light with optical fibers.
Opt. Lett., 37(13):2451–2453, Jul 2012.

[8] J. Durnin.
Exact solutions for nondiffracting beams. i. the scalar theory.
JOSA A, 4(4):651–654, 1987.

[9] P. Steinvurzel, K. Tantiwanichapan, M. Goto, and S. Ramachandran.
Fiber-based bessel beams with controllable diffraction-resistant distance.
Optics letters, 36(23):4671–4673, 2011.

[10] S. Ramachandran, J. M. Fini, M. Mermelstein, J. W. Nicholson, S. Ghalmi, and M. F. Yan.
Ultra-large effective-area, higher-order mode fibers: a new strategy for high-power lasers.
Laser & Photonics Reviews, 2(6):429–448, 2008.

[11] C. D. Poole, J. M. Wiesenfeld, D. J Digiovanni, and A. M. Vengsarkar.
Optical fiber-based dispersion compensation using higher order modes near cutoff.
Lightwave Technology, Journal of, 12(10):1746–1758, 1994.

[12] J. C. Knight, J. Arriaga, T. A. Birks, A. Ortigosa-Blanch, W. J. Wadsworth, and P. St. J. Russell.
Anomalous dispersion in photonic crystal fiber.
IEEE photonics technology letters, 12(7):807–809, 2000.

[13] S. Ramachandran, S. Ghalmi, Z. Wang, and M. Yan.
Band-selection filters with concatenated long-period gratings in few-mode fibers.
Opt. Lett., 27(19):1678–1680, Oct 2002.

[14] J. Limpert, N. Deguil-Robin, I. Manek-Hönninger, F. Salin, F. Röser, A. Liem, T. Schreiber, S. Nolte, H. Zellmer, A. Tünnermann, J. Broeng, A. Petersson, and C. Jakobsen.
High-power rod-type photonic crystal fiber laser.
Optics Express, 13(4):1055–1058, 2005.

[15] J. M. Fini and S. Ramachandran.
Natural bend-distortion immunity of higher-order-mode large-mode-area fibers.
Optics letters, 32(7):748–750, 2007.

[16] A. M. Vengsarkar, P. J. Lemaire, J. B. Judkins, V. Bhatia, T. Erdogan, and J. E. Sipe.
Long-period fiber gratings as band-rejection filters.
Lightwave Technology, Journal of, 14(1):58–65, 1996.

[17] T. Erdogan.
Fiber grating spectra.
Journal of lightwave technology, 15(8):1277–1294, 1997.

[18] T. Erdogan.
Cladding-mode resonances in short-and long-period fiber grating filters.
JOSA A, 14(8):1760–1773, 1997.

[19] R. Kashyap.

Fiber bragg gratings.
Academic press, 1999.

[20] X. Shu, L. Zhang, and I. Bennion.
Fabrication and characterisation of ultra-long-period fibre gratings.
Optics communications, 203(3):277–281, 2002.

[21] J.-C. Guo, Y.-S. Yu, X.-L. Zhang, C. Chen, R. Yang, C. Wang, R.-Z. Yang, Q.-D. Chen, and H.-B. Sun.
Compact long-period fiber gratings with resonance at second-order diffraction.
IEEE Photonics Technology Letters, 24(16):1393–1395, 2012.

[22] S. M. Israelsen and K. Rottwitt.
Divergence angle as a quality parameter for fiber modes.
In *CLEO: QELS_Fundamental Science*, pages JW2A–19. Optical Society of America, 2014.

[23] B. Tai, Z. Wang, Y. Liu, J. Xu, B. Liu, H. Wei, and W. Tong.
High order resonances between core mode and cladding supermodes in long period fiber gratings inscribed in photonic bandgap fibers.
Opt. Express, 18(15):15361–15370, Jul 2010.

[24] Y. Wang, W. Jin, J. Ju, H. Xuan, H. L. Ho, L. Xiao, and D. Wang.
Long period gratings in air-core photonic bandgap fibers.
Opt. Express, 16(4):2784–2790, Feb 2008.

[25] F. Hindle, E. Fertein, C. Przygodzki, F. Durr, L. Paccou, R. Bocquet, P. Niay, H. G. Limberger, and M. Douay.
Inscription of long-period gratings in pure silica and germano-silicate fiber cores by femtosecond laser irradiation.
IEEE Photonics Technology Letters, 16(8):1861–1863, 2004.

[26] T. Allsop, K. Kalli, K. Zhou, Y. Lai, G. Smith, M. Dubov, D. J. Webb, and I. Bennion.
Long period gratings written into a photonic crystal fibre by a femtosecond laser as directional bend sensors.
Optics Communications, 281(20):5092–5096, 2008.

[27] Y. Kondo, K. Nouchi, T. Mitsuyu, M. Watanabe, P. G. Kazansky, and K. Hirao.
Fabrication of long-period fiber gratings by focused irradiation of infrared femtosecond laser pulses.
Optics letters, 24(10):646–648, 1999.

[28] C. D. Poole, H. M. Presby, and J. P. Meester.
Two-mode fibre spatial-mode converter using periodic core deformation.
Electronics letters, 30(17):1437–1438, 1994.

[29] C. D. Poole, C. D. Townsend, and K. T. Nelson.
Helical-grating two-mode fiber spatial-mode coupler.
Journal of lightwave technology, 9(5):598–604, 1991.

[30] P. Z. Dashti, F. Alhassen, and H. P. Lee.
Observation of orbital angular momentum transfer between acoustic and optical vortices in optical fiber.
Physical review letters, 96(4):043604, 2006.

[31] L. Grüner-Nielsen and J. W. Nicholson.
Stable mode converter for conversion between lp01 and lp11 using a thermally induced long period grating.
Proceedings of IEEE Summer Topical Meeting, pages 214–215, 2012.

[32] J. Dong and K. S. Chiang.
Temperature-insensitive mode converters with co 2-laser written long-period fiber gratings.
IEEE Photonics Technology Letters, 27(9):1006–1009, 2015.

[33] A. J. Verhoef, .L Zhu, S. M. Israelsen, L. Grüner-Nielsen, A. Unterhuber, W. Kautek, K. Rottwitt, A. Baltuška, and A. Fernández.
Sub-100 fs pulses from an all-polarization maintaining yb-fiber oscillator with an anomalous dispersion higher-order-mode fiber.
Optics express, 23(20):26139–26145, 2015.

[34] L Zhu, A. J. Verhoef, K. G. Jespersen, V. L. Kalashnikov, L. Grüner-Nielsen, D. Lorenc, A. Baltuška, and A. Fernández.
Generation of high fidelity 62-fs, 7-nj pulses at 1035 nm from a net normal-dispersion yb-fiber laser with anomalous dispersion higher-order-mode fiber.
Optics express, 21(14):16255–16262, 2013.

[35] S. E. Golowich and S. Ramachandran.
Impact of fiber design on polarization dependence in microbend gratings.
Opt. Express, 13(18):6870–6877, Sep 2005.

[36] T. Allsop, F. Floreani, K. P. Jedrzejewski, P. V. S. Marques, R. Romero, D. J. Webb, and I. Bennion.
Spectral characteristics of tapered lpg device as a sensing element for refractive index and temperature.

Journal of lightwave technology, 24(2):870, 2006.

[37] D. Östling and H. E. Engan.
Broadband spatial mode conversion by chirped fiber bending.
Optics letters, 21(3):192–194, 1996.

[38] V. Grubsky and J. Feinberg.
Long-period fiber gratings with variable coupling for real-time sensing applications.
Opt. Lett., 25(4):203–205, Feb 2000.

[39] S. H. M. Larsen, M. E. V. Pedersen, L. Grüner-Nielsen, M. F. Yan, E. M. Monberg, P. W. Wisk, and K. Rottwitt.
Polarization-maintaining higher-order mode fiber module with anomalous dispersion at 1 μm.
Optics letters, 37(20):4170–4172, 2012.

[40] J. W. Nicholson, J. M. Fini, A. DeSantolo, P. S. Westbrook, R. S. Windeler, T. Kremp, C. Headley, and D. J. DiGiovanni.
A higher-order mode fiber amplifier with an axicon for output mode conversion.
In *SPIE LASE*, pages 93441V–93441V. International Society for Optics and Photonics, 2015.

[41] T. Grosjean, S. S. Saleh, M. A. Suarez, I. A. Ibrahim, V. Piquerey, D. Charraut, and P. Sandoz.
Fiber microaxicons fabricated by a polishing technique for the generation of bessel-like beams.
Applied optics, 46(33):8061–8067, 2007.

[42] N. Lindlein, G. Leuchs, and S. Ramachandran.
Achieving gaussian outputs from large-mode-area higher-order-mode fibers.
Applied optics, 46(22):5147–5157, 2007.

[43] P. Gregg, M. Mirhosseini, A. Rubano, L. Marrucci, E. Karimi, R. W. Boyd, and S. Ramachandran.
Q-plates as higher order polarization controllers for orbital angular momentum modes of fiber.
Optics letters, 40(8):1729–1732, 2015.

[44] J. Carpenter, B. C. Thomsen, and T. D. Wilkinson.
Degenerate mode-group division multiplexing.
Journal of Lightwave Technology, 30(24):3946–3952, 2012.

[45] A. K. Sridharan, P. H. Pax, J. E. Heebner, D. R. Drachenberg, J. P. Armstrong, and J. W. Dawson.
Mode-converters for rectangular-core fiber amplifiers to achieve diffraction-limited power scaling.
Optics express, 20(27):28792–28800, 2012.

[46] J. Demas, L. Rishøj, and S. Ramachandran.
Free-space beam shaping for precise control and conversion of modes in optical fiber.
Opt. Express, 23(22):28531–28545, Nov 2015.

[47] H. Dobb, K. Kalli, and D. J. Webb.
Temperature insensitive long-period grating sensors in photonic crystal fiber.
In *Photonics North*, pages 66–79. International Society for Optics and Photonics, 2004.

[48] G. Kakarantzas, T. A. Birks, and P. St. J. Russell.
Structural long-period gratings in photonic crystal fibers.
Optics Letters, 27(12):1013–1015, 2002.

[49] K. Lai, S. G. Leon-Saval, A. Witkowska, W. J. Wadsworth, and T. A. Birks.
Wavelength-independent all-fiber mode converters.
Opt. Lett., 32(4):328–330, Feb 2007.

[50] A. Witkowska, S. G. Leon-Saval, A. Pham, and T. A. Birks.
All-fiber lp_{11} mode convertors.
Opt. Lett., 33(4):306–308, Feb 2008.

[51] S. G. Leon-Saval, T. A. Birks, J. Bland-Hawthorn, and M. Englund.
Multimode fiber devices with single-mode performance.
Opt. Lett., 30(19):2545–2547, Oct 2005.

[52] D. Noordegraaf, P. M. W. Skovgaard, M. D. Nielsen, and J. Bland-Hawthorn.
Efficient multi-mode to single-mode coupling in a photonic lantern.
Opt. Express, 17(3):1988–1994, Feb 2009.

[53] S. G. Leon-Saval, N. K. Fontaine, J. R. Salazar-Gil, B. Ercan, R. Ryf, and J. Bland-Hawthorn.
Mode-selective photonic lanterns for space-division multiplexing.
Opt. Express, 22(1):1036–1044, Jan 2014.

[54] D. J. Richardson, J. M. Fini, and L. E. Nelson.
Space-division multiplexing in optical fibres.
Nature Photonics, 7(5):354–362, 2013.

[55] H. Hu, F. Da Ros, F. Ye, M. Pu, K. Ingerslev, E. Porto da Silva, Md. Nooruzzaman, Y. Amma, Y. Sasaki, T. Mizuno, Y. Miyamoto, L. Ottaviano, E. Semenova, P. Guan, D. Zibar, M. Galili, K. Yvind, L. K. Oxenløwe, and T. Morioka.
Single-source algaas frequency comb transmitter for 661 tbit/s data transmission in a 30-core fiber.
In *Conference on Lasers and Electro-Optics*, page JTh4C.1. Optical Society of America, 2016.

[56] R. Ryf, S. Randel, A. H. Gnauck, C. Bolle, A. Sierra, Sami Mumtaz, Mi. Esmaeelpour, E. C. Burrows, R.-J. Essiambre, P. J. Winzer, D. W. Peckham, A. H. McCurdy, and R. Lingle.
Mode-division multiplexing over 96 km of few-mode fiber using coherent 6 6 mimo processing.
Journal of Lightwave technology, 30(4):521–531, 2012.

[57] S. W. James and R. P. Tatam.
Optical fibre long-period grating sensors: characteristics and application.
Measurement science and technology, 14(5):R49, 2003.

[58] C. C. Ye, S. W. James, and R. P. Tatam.
Simultaneous temperature and bend sensing with long-period fiber gratings.
Optics Letters, 25(14):1007–1009, 2000.

[59] E. Li, X. L. Wang, and C. Zhang.
Fiber-optic temperature sensor based on interference of selective higher-order modes.
2006.

[60] S. H. M. Larsen, L. S. Rishøj, and K. Rottwitt.
All-fiber raman probe using higher order modes.
In *Optical Sensors*, pages SM2D–6. Optical Society of America, 2013.

[61] L. Yan, P. Kristensen, and S. Ramachandran.
All-fiber sted microscopy illumination system.
In *Conference on Lasers and Electro-Optics*, page SM4P.3. Optical Society of America, 2016.

[62] J. van Howe, J. H. Lee, S. Zhou, F. Wise, C. Xu, S. Ramachandran, S. Ghalmi, and M. F. Yan.
Demonstration of soliton self-frequency shift below 1300nm in higher-order mode, solid silica-based fiber.
Opt. Lett., 32(4):340–342, Feb 2007.

[63] P. Steinvurzel, J. Demas, B. Tai, Y. Chen, L. Yan, and S. Ramachandran.

Broadband parametric wavelength conversion at 1 μm with large mode area fibers.
Optics letters, 39(4):743–746, 2014.

[64] J. Demas, P. Steinvurzel, B. Tai, L. Rishøj, Y. Chen, and S. Ramachandran.
Intermodal nonlinear mixing with bessel beams in optical fiber.
Optica, 2(1):14–17, Jan 2015.

[65] H. Yoda, P. Polynkin, and M. Mansuripur.
Beam quality factor of higher order modes in a step-index fiber.
Journal of lightwave technology, 24(3):1350, 2006.

[66] S. Wielandy.
Implications of higher-order mode content in large mode area fibers with good beam quality.
Optics Express, 15(23):15402–15409, 2007.

[67] J. R. Fienup.
Phase retrieval algorithms: a comparison.
Applied optics, 21(15):2758–2769, 1982.

[68] O. Shapira, A. F. Abouraddy, J. D. Joannopoulos, and Y. Fink.
Complete modal decomposition for optical waveguides.
Physical review letters, 94(14):143902, 2005.

[69] D. Flamm, C. Schulze, D. Naidoo, S. Schröter, A. Forbes, and M. Duparré.
All-digital holographic tool for mode excitation and analysis in optical fibers.
J. Lightwave Technol., 31(7):1023–1032, Apr 2013.

[70] J. W. Nicholson, A. D. Yablon, S. Ramachandran, and S. Ghalmi.
Spatially and spectrally resolved imaging of modal content in large-mode-area fibers.
Optics express, 16(10):7233–7243, 2008.

[71] L. Grüner-Nielsen, Y. Sun, J. W. Nicholson, D. Jakobsen, K. G. Jespersen, R. Lingle Jr, and B. Pálsdóttir.
Few mode transmission fiber with low dgd, low mode coupling, and low loss.
Journal of Lightwave Technology, 30(23):3693–3698, 2012.

[72] H.-J. Otto, F. Jansen, F. Stutzki, C. Jauregui, J. Limpert, and A. Tunnermann.
Improved modal reconstruction for spatially and spectrally resolved imaging.
Journal of lightwave technology, 31(8):1295–1299, 2013.

[73] D. Gray, M. Petrovich, S. R. Sandoghchi, N. Wheeler, N. Baddela, G. Jasion, T. Bradley, D. Richardson, and F. Poletti.

Real-time modal analysis via wavelength-swept spatial and spectral (s< sup> 2</sup>) imaging.
2016.

[74] D. N. Schimpf, R. A. Barankov, and S. Ramachandran.
Cross-correlated (c 2) imaging of fiber and waveguide modes.
Optics express, 19(14):13008–13019, 2011.

[75] J. Demas and S. Ramachandran.
Sub-second mode measurement of fibers using c 2 imaging.
Optics express, 22(19):23043–23056, 2014.

[76] S. Chávez-Cerda, M. A. Meneses-Nava, and J. Miguel Hickmann.
Interference of traveling nondiffracting beams.
Opt. Lett., 23(24):1871–1873, Dec 1998.

[77] Y. Chen, L. Yan, L. Rishøj, P. Steinvurzel, and S. Ramachandran.
Dynamically tunable optical bottles from an optical fiber.
Opt. Lett., 37(16):3327–3329, Aug 2012.

[78] S. M. Israelsen, L. S. Rishøj, and K. Rottwitt.
Break up of the azimuthal symmetry of higher order fiber modes.
Optics express, 22(10):11861–11868, 2014.

[79] S. M. Israelsen, L. S. Rishøj, and K. Rottwitt.
Selfhealing of asymmetric bessel-like modes.
In *Bragg Gratings, Photosensitivity, and Poling in Glass Waveguides*, pages JTu3A–7. Optical Society of America, 2014.

[80] M. Steel.
Reflection symmetry and mode transversality in microstructured fibers.
Optics express, 12(8):1497–1509, 2004.

[81] M. J. Steel, T. P. White, C. M. de Sterke, R. C. McPhedran, and L. C. Botten.
Symmetry and degeneracy in microstructured optical fibers.
Optics letters, 26(8):488–490, 2001.

[82] J. M. Fini.
Improved symmetry analysis of many-moded microstructure optical fibers.
JOSA B, 21(8):1431–1436, 2004.

[83] L. Rishøj, M. Jones, J. Demas, P. Gregg, G. Prabhakar, L. Yan, T. Hawkins, J. Ballato, and S. Ramachandran.

Polymer-clad silica fibers for tailoring modal area and dispersion.
Optics Letters, 41(15):3587–3590, 2016.

[84] J. W. Goodman.
Introduction to Fourier optics.
Roberts and Company Publishers, 2005.

[85] S. Golowich.
Asymptotic theory of strong spin–orbit coupling in optical fiber.
Optics letters, 39(1):92–95, 2014.

[86] K. Ingerslev, S. M. Israelsen, and K. Rottwitt.
S 2-imaging of bessel-like beams.
In *Australia and New Zealand Conference on Optics and Photonics (ANZCOP 2013)*, 2013.

[87] S. Ramachandran, Z. Wang, and M. Yan.
Bandwidth control of long-period grating-based mode converters in few-mode fibers.
Optics letters, 27(9):698–700, 2002.

[88] S. Ramachandran.
Dispersion-tailored few-mode fibers: a versatile platform for in-fiber photonic devices.
Lightwave Technology, Journal of, 23(11):3426–3443, 2005.

[89] S. M. Israelsen and K. Rottwitt.
Broadband higher order mode conversion using chirped microbend long period gratings.
Submitted to Optics Express, see full paper in Appendix A.

[90] D. B. Stegall and T. Erdogan.
Dispersion control with use of long-period fiber gratings.
J. Opt. Soc. Am. A, 17(2):304–312, Feb 2000.

[91] T. He, L. Rishøj, J. Demas, and S. Ramachandran.
Dispersion compensation using chirped long period gratings.
CLEO: Science and Innovations, pages STu3P–7, 2016.

[92] S. Ramachandran, J. Wagener, R. Espindola, and T. A. Strasser.
Effects of chirp in long period gratings.
Bragg Gratings, Photosensitivity, and Poling in Glass Waveguides, page BE1, 1999.

[93] S. Ramachandran, P. Kristensen, and M. F. Yan.
Generation and propagation of radially polarized beams in optical fibers.
Opt. Lett., 34(16):2525–2527, Aug 2009.

[94] M. Matsuhara, K. O. Hill, and A. Watanabe.
Optical-waveguide filters: Synthesis.
JOSA, 65(7):804–809, 1975.

[95] R. C. Youngquist, J. L. Brooks, and H. J. Shaw.
Two-mode fiber modal coupler.
Opt. Lett., 9(5):177–179, May 1984.

[96] X. Peng, K. Kim, M. Mielke, T. Booth, J. W. Nicholson, J. M. Fini, X. Liu, A. DeSantolo, P. S. Westbrook, R. S. Windeler, E. M. Monberg, F. V. DiMarcello, C. Headley, and D. J. DiGiovanni.
Higher-order mode fiber enables high energy chirped-pulse amplification.
Optics express, 21(26):32411–32416, 2013.

[97] P. Almoro, G. Pedrini, and W. Osten.
Complete wavefront reconstruction using sequential intensity measurements of a volume speckle field.
Applied optics, 45(34):8596–8605, 2006.

[98] P. F. Almoro, A. M. S. Maallo, and S. G. Hanson.
Fast-convergent algorithm for speckle-based phase retrieval and a design for dynamic wavefront sensing.
Applied optics, 48(8):1485–1493, 2009.

[99] J. R. Fienup and C. C. Wackerman.
Phase-retrieval stagnation problems and solutions.
JOSA A, 3(11):1897–1907, 1986.

[100] https://www.thorlabs.com/thorcat/6800/780hp-specsheet.pdf.

[101] L. G. Cohen.
Comparison of single-mode fiber dispersion measurement techniques.
Lightwave Technology, Journal of, 3(5):958–966, 1985.

[102] L. Grüner-Nielsen, S. Ramachandran, K. Jespersen, S. Ghalmi, M. Garmund, and B. Pálsdóttir.
Optimization of higher order mode fibers for dispersion management of femtosecond fiber lasers.
In *Lasers and Applications in Science and Engineering*, pages 68730Q–68730Q. International Society for Optics and Photonics, 2008.

[103] D. Menashe, M. Tur, and Y. Danziger.
Interferometric technique for measuring dispersion of high order modes in optical fibres.

Electronics Letters, 37(24):1, 2001.

[104] S. M. Israelsen, M. A. U. Castaneda, and K. Rottwitt.
Determining the group velocity dispersion by field analysis for the lp_{0X}-, lp_{1X}-, and lp_{2X}-mode groups independently of the fiber length.
Submitted to JOSA B, see full paper in Appendix B.

[105] P. Sansonetti.
Modal dispersion in single-mode fibres: simple approximation issued from mode spot size spectral behaviour.
Electronics Letters, 15(18):647–648, 1982.

[106] J. P. Pocholle, J. Raffy, J. Auge, and M. Papuchon.
Determination of modal dispersion in monomode fibres from wavelength dependence of the mode spot size.
Electronics letters, 19(25-26):1093–1094, 1983.

[107] F. Brechet, J. Marcou, D. Pagnoux, and P. Roy.
Complete analysis of the characteristics of propagation into photonic crystal fibers, by the finite element method.
Optical Fiber Technology, 6(2):181–191, 2000.